Rolling Search for a Cascade GRB Signal

by

Brennan John Hughey

A dissertation submitted in partial fulfillment of the

requirements for the degree of

Doctor of Philosophy

(Physics)

at the

University of Wisconsin – Madison

2007

Rolling Search for a Cascade GRB Signal

Brennan John Hughey

Under the supervision of Professor Albrecht Karle

At the University of Wisconsin — Madison

High energy neutrino astronomy has the potential to address a number of topics in astronomy and particle physics, including the origins of the highest energy cosmic rays. The AMANDA detector was, until recently being surpassed by its own successor IceCube, the world's largest neutrino telescope. We present details of an untriggered 'rolling' search for high energy neutrinos from gamma-ray bursts and other transients in the years 2001-2003 using the AMANDA detector. This is the first analysis of its type to be conducted by AMANDA and serves as a useful complement to conventional gamma-ray burst neutrino searches, which utilize gamma-ray observations by various satellites. We place limits on the astrophysical flux of neutrinos based on several models, including the Waxman-Bahcall GRB flux.

Albrecht Karle (Adviser)

To Mom and Dad.

Acknowledgements

Many thanks to:

Albrecht Karle and Kael Hanson, for serving as mentors.

Gary Hill and Francis Halzen, for helpful suggestions concerning the specifics of the analysis.

Ignacio Taboada, Mike Stamatikos, Marek Kowalski, Julia Becker, Spencer Klein and other IceCubists for useful discussions.

The Madison IceCube/AMANDA group, especially my fellow grad students.

Henrikke Wissing for filtering the 2002 and 2003 stream used in this analysis.

And my parents, for all their love and support.

Contents

Chapter 1

Introduction

High energy neutrino astrophysics is a field which is still in its infancy, but which promises to reveal a great deal about the universe in which we live. The Antarctic Muon and Neutrino Detector Array (AMANDA) is by far the largest complete neutrino telescope constructed so far, although it will be joined in the next several years by similar detectors in the Mediterranean and in particular by its own successor, IceCube. It therefore provides both the best opportunity to look for high energy neutrinos and a means of testing different analysis methods which can later be applied to the larger IceCube array.

This thesis presents a rolling search for a transient neutrino source using cascades in the AMANDA-II detector. The analysis discussed here optimizes the search for a gamma-ray burst neutrino signal, but this method is also valid for other transients. Since the search does not require coincident photon emission like other GRB searches, it offers the possibility of discovering something completely unexpected. This method for detecting previously unidentified transients will not supplant the triggered GRB search, point source and diffuse analysis methods that have been used by many researchers over the course of the past several years in AMANDA. However, one ad-

vantage of high energy neutrino detectors is the versatility of methods used to examine the incoming data set, and the Rolling Search method adds a new tool to this toolkit.

This document is organized as follows: the next three chapters focus on summarizing the relevant background information in the areas of neutrino astrophysics (Chapter 2), high energy neutrino detection with AMANDA (Chapter 3), and the physics of Gamma Ray Bursts (Chapter 4). Chapter 5 gives a generic overview of the rolling search method. The next several chapters provide the specific details of the analysis, including filtering and reconstruction techniques (Chapter 6), data reduction (Chapter 7), and the statistical techniques employed (Chapter 8). Chapter 9 provides more details about analysis procedure, including a discussion of systematic errors. Chapter 10 presents the results of the analysis and discusses possibilities for future extensions.

Chapter 2

Neutrino Astrophysics

2.1 Neutrino Properties

Neutrinos were postulated by Wolfgang Pauli in the 1930s in order to explain why neutrons appeared to have more total energy than the protons and electrons into which they decayed. Pauli famously commented about the neutrino "I have done a terrible thing. I have invented a particle that cannot be detected [1]." He had a pretty strong case for this assertion. The neutrino is almost massless and therefore virtually unaffected by the gravitational force. It is also a lepton, meaning it is unaffected by the strong nuclear force, and chargeless, making it immune to electromagnetic effects.

Like many other claims that a scientific discovery was impossible, however, this one proved to be false. Neutrinos are subject to the weak nuclear force, and, while the majority of neutrinos can pass through the entire Earth without being even slightly affected, one will occasionally interact with a particle of matter through a weak interaction. The products of this decay are detectable. In the 1950's Reines and Cowan used liquid scintillators to observe neutrinos which were created in a nuclear reactor

[2], giving rise to the field of experimental neutrino physics.

2.2 Reasons For Neutrino Astronomy

There are several reasons to study astrophysical neutrinos. The most general reason to study neutrinos is that they are a different way of viewing the universe. Throughout the history of astronomy, whenever a new method of viewing the universe has been developed, usually studying a new range of the electromagnetic spectrum, new science has been discovered that was completely unanticipated. This is demonstrated anecdotally in the following table:

Surprising Discoveries in Astronomy

Wavelength	User	Year	Intended Use	Actual Use
Optical	Galileo	1608	navigation	moons of Jupiter
Radio	Jansky	1932	Noise	Radio Galaxies
Microwave	Penzias,Wilson	1965	Radio Galaxies	CMB
X-ray	Giaconni et al.	1967	sun, moon	neutron stars
γ-ray	military	1960's	nuclear explosions	GRBs

There are, however, more concrete and specific reasons for neutrino astronomy. Ironically, the same reasons that make neutrinos so difficult to detect also make them useful as an astrophysical signal. Since neutrinos interact only through the weak force, and then only rarely, they can pass through intervening matter which is opaque to both photons and cosmic rays. This means that they may be the only signal to come directly from otherwise invisible objects, such as the central engines of Active Galactic Nuclei. A related advantage is that neutrinos point directly back to their source. By contrast, photons can be absorbed and re-emitted by intervening matter as they travel to us. Cosmic rays can be deflected by the galaxy's magnetic field, an effect which cannot be adjusted for mathematically because the strength of the galaxy's magnetic

field is not well known. Therefore, the gamma rays and cosmic rays which do make it to Earth have lost their directional information.

Specific scientific questions which searches for high energy neutrinos can address include the nature of dark matter and the existence of the GZK cutoff. Perhaps the most significant motivating question in neutrino astronomy is the mystery of high energy cosmic rays, which we discuss in the next section.

2.3 Cosmic Rays

Cosmic rays are positively charged nuclei coming from space. Roughly 90% of cosmic rays are protons, with the remaining 10% being composed of heavier elements, although composition varies as a function of energy. Because neutrinos are produced primarily in hadronic processes, very energetic neutrinos generally require similarly energetic protons to create them. Astrophysical objects that emit neutrinos of very high energies therefore should also produce high energy protons, meaning that they are candidates to be the source of the heretofore unexplained high energy cosmic rays. In contrast, photons can't be used as a probe for cosmic ray production, since they can also be created in electromagnetic processes in the absence of accelerated protons.

The cosmic ray energy spectrum follows a power law index of 2.7 over many orders of magnitude up to a break, referred to as the knee. The spectral index then shifts to roughly 3.2 until a second break, called the ankle (see Figure 2.1). The exact slope of the spectrum at this energy is unclear due to low statistics.

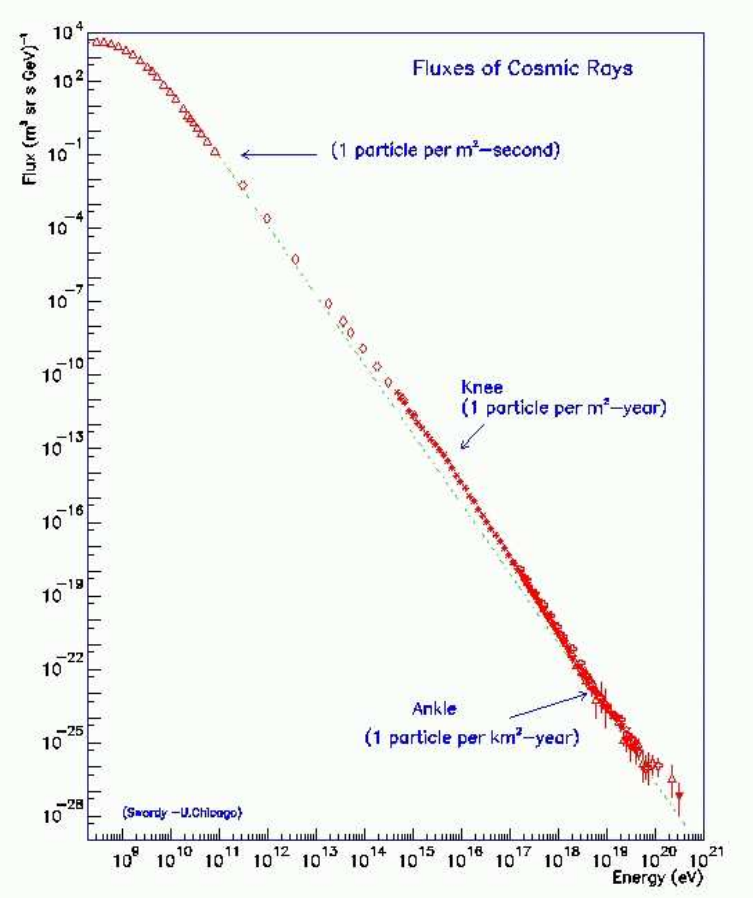

Figure 2.1: The cosmic ray spectrum, borrowed from [3].

2.3.1 Fermi Acceleration

The process by which cosmic rays are thought to reach high energies is called Fermi Acceleration. Up to the knee, the cosmic ray spectrum is generally attributed to Fermi acceleration in supernovae. Although their origin is unclear, it is often postulated that a similar acceleration process in gamma-ray bursts is at least partially responsible for cosmic rays above the knee [4] [5].

Second order Fermi acceleration was postulated by Enrico Fermi in 1949. Charged

particles encounter magnetic field configurations in a turbulent setting. They reflect off these "magnetic mirrors" with a gain in momentum $2m\gamma V_m$ in the case of a head-on collision or an equal loss of momentum in the case of an overtaking collision. Here, m is the mass of the charged particle, γ is the Lorentz factor and V_m is the velocity of the moving field configuration. The gain in a single head-on collision equals the loss in an overtaking collision on average. However, the random collisions result in a net acceleration of the particle because the the total number of head-on collisions is greater than the number of overtaking collisions. This is analogous to the fact that a southbound car on an expressway will generally pass by many more northbound cars than southbound ones.

The net gain in acceleration through second order Fermi acceleration is, however, insufficient to explain how cosmic rays are accelerated to the energies at which they are observed. First order Fermi acceleration, explained 30 years later, is a much more efficient accelerator. First order Fermi acceleration requires turbulent shocks, such as those found in the relativistic jets of AGN and GRBs. Shocks, like any longitudinal wave, compress the medium they are in. The magnetic field configurations which the particles reflect off therefore travel at a reduced velocity inside the shock compared to out of it, by a factor equal to the compression ratio of the shock. Thus, for particles being reflected back and forth across the shock front, momentum losses for overtaking collisions in the shocked medium are now lower in magnitude than the gains from head-on collisions outside the shocked region. The net gain in acceleration across the shock is therefore much greater than would be found in shock-free 2nd order Fermi acceleration.

There are significant differences between relativistic shock acceleration (such as that found in GRBs) and the nonrelativistic version. In a relativistic shock process the only particles that can outrun the shock are those traveling in almost the same direction as the shock itself, which results in a very non-uniform distribution of particles in the area of the relativistic shock [6], unlike the non-relativistic case. Additionally, in relativistic shock acceleration, the first time a particle crosses a shock it receives a large boost in velocity but the kinematics are such that subsequent crossings are much less efficient [7].

2.4 Astrophysical Neutrinos

In general, neutrinos are produced in astrophysical sources through proton-photon interactions of the form:

$$p + \gamma \rightarrow \Delta^+ \rightarrow \pi^+(+n) \rightarrow \mu^+ + \nu_\mu \rightarrow e^+ + \nu_e + \bar{\nu}_\mu + \nu_\mu. \tag{2.1}$$

Proton-proton scattering can also result in neutrinos through production of both π^+ and π^-. The primary difference in the two reaction mechanisms is that $p+\gamma$ reactions always lead to positively charged particles (π^+), while pp interactions can yield π^+ or π^-, which alters the predicted ratio of neutrinos to antineutrinos. In some cases, similar processes can occur with the more massive kaons instead of pions. There are many possible sources of astrophysical neutrinos; a brief overview is presented here.

2.4.1 Atmospheric Neutrinos

Atmospheric neutrinos come from interactions of cosmic rays with molecules in the upper atmosphere. They therefore follow the same power law energy spectrum as cosmic rays at low energies, but transition to a slope an order of magnitude steeper as

the pions and kaons from which they are created start to undergo significant energy losses before decaying [8]. In the case of neutrino telescopes such as AMANDA, they are a lower energy background for extraterrestrial neutrino sources. However, they also serve as a calibration tool and can be used as a sample to study many aspects of neutrino physics. AMANDA observes $\sim 10^3$ atmospheric neutrinos per year.

2.4.2 Supernovae

The detection of neutrinos from the relatively nearby Supernova 1987A by Super-Kamiokande-II in Japan [9], Baksan in the Caucasus and the IMB experiment in the U.S. [10] is to date the only confirmed detection of neutrinos from outside the solar system. The supernovae neutrino spectrum peaks in the MeV range. For high energy detectors such as AMANDA, neutrinos in this energy range are unresolvable individually due to sparse detector spacing, but a large number of MeV neutrinos would lead to a measurable increase in the overall event rate of the detector. Sensitivity to supernova neutrinos is generally limited to sources within our own galaxy [11].

2.4.3 Points Sources and Transients

There are many types of astrophysical objects which may be relatively steady-state emitters of neutrinos. Specific candidates for point sources include microquasars in our own galaxy and active galactic nuclei (AGN), both of which may produce high energy cosmic rays and neutrinos in their relativistic jets. Gamma ray bursts, the most promising transient source for extragalactic neutrinos, are discussed in detail in the next chapter.

2.4.4 WIMPs

Weakly Interacting Massive Particles (WIMPs) are a leading dark matter candidate. WIMPs may accumulate in astronomical objects, such as the sun or even the Earth, as a result of neutral current weak force elastic scattering. WIMPs may then annihilate with anti-WIMPs, producing a variety of decay products including neutrinos. Although the exact parameters of WIMPs are not well known, a WIMP neutrino signal would be identifiable by its direction, as it would come from the Earth's center or the sun [22].

2.4.5 Hidden Sources

The most obvious neutrino sources are those which emit observable photons. As previously mentioned, however, every time the universe has been viewed through a different lens, completely unexpected discoveries have been made. It is very possible that there may exist high energy neutrino sources without visible photon signatures which we currently have no information about. In the absence of proton and photon and proton emission, such astrophysical objects would not necessarily be constrained by the Waxman-Bahcall bound [12], a limit on neutrino flux constraining emission from optically thin sources. For example, for sources at high redshift $\geq$TeV energy photons may be absorbed before reaching Earth or there may be closer sources in which photons become absorbed but which allow neutrinos to escape.

2.5 Neutrino Oscillation

Neutrinos come in three flavors. These are the electron neutrino (ν_e), muon neutrino (ν_μ), and tau neutrino (ν_τ), corresponding to the more massive electron, μ,

and τ leptons. Each of these flavors has a corresponding anti-particle.

Ray Davis's experiment at Homestake mine was the first to detect solar neutrinos, in the late 1960's. They observed a flux of solar ν_μ by using a chlorine tank as the detector medium [13]. However, they saw only 1/3 of the expected number. This "solar neutrino problem" was eventually solved with data from the SuperKamiokande and SNO experiments. They determined that neutrinos are able to oscillate from one flavor to another over a sufficiently large distance, allowing the ν_μ to convert into flavors which could not be detected by the Homestake experiment. This discovery was revolutionary not only because neutrino oscillations solved the solar neutrino problem, but because in doing so they demonstrated that neutrinos have mass[1]. Each flavor eigenstate is a mixture of mass eigenstates, with the mixing described by the matrix:

$$\begin{bmatrix} m_1' \\ m_2' \\ m_3' \end{bmatrix} = \begin{bmatrix} c_{12}c_{13} & s_{12}c_{13} & s_{13} \\ -s_{12}c_{23} - c_{12}s_{23}s_{13} & c_{12}c_{23} - s_{12}s_{23}s_{13} & s_{23}c_{13} \\ s_{12}s_{23} - c_{12}c_{23}s_{13} & -c_{12}s_{23} - s_{12}c_{23}s_{13} & c_{23}c_{13} \end{bmatrix} \begin{bmatrix} m_1 \\ m_2 \\ m_3 \end{bmatrix} \tag{2.2}$$

where m is the neutrino mass, c_{ij} is $\cos(\theta_{ij})$ and s_{ij} is $\sin(\theta_{ij})$. Further complicating the issue is the possibility of a non-fourth, "sterile" neutrino, a noninteracting lepton that is predicted by some particle physics models, but has not been proven to exist. For most astrophysical phenomena, the predicted ratio of the three flavors $\nu_e : \nu_\mu : \nu_\tau$ is 1:2:$(3X10^{-5})$ [14]. The ratio of 1 ν_e for every 2 ν_μ is simply a result of the products in the pγ reaction described in equation 2.1. The ν_τ production comes from charmed mesons, an entirely different process which is suppressed relative to pion and kaon decay due to low cross-sections and a higher energy threshold [15]. Over astrophysical

[1] According to relativity, no time passes for a particle traveling at the speed of light. A massless neutrino would travel at exactly c, and therefore couldn't oscillate because it wouldn't have had any time to do so.

distances, neutrino oscillations should convert the ratio of ν_e:ν_μ:ν_τ at Earth to 1:1:1 (lumping together neutrinos and anti-neutrinos of each flavor) [14]. This assumes a ratio of Earth to source distance (in parsecs) to neutrino energy (in GeV) such that:

$$\frac{L(pc)}{E(GeV)} \geq 10^{-10}. \tag{2.3}$$

For an ultra-high-energy 10^9 GeV neutrino, this means a minimum distance of 10^{-1} parsecs, only about a third of a light year and only a fraction of the distance to the nearest star. For lower energy neutrinos, this minimum distance is even less.

However, Kashti and Waxman [15] point out that at high energies, π are more likely than μ to decay before losing a significant amount of their energy, meaning that the μ^+ particles in equation 2.1 don't decay into neutrinos, altering the 1:2 low energy flavor ratio of ν_e:ν_μ to 0:1 at high energies. This alters the expected flavor ratio at Earth to 1:1.8:1.8 for very energetic events. The transition between the low and high energy flavor ratios occurs over a couple orders of magnitude in $\log_{10}(E)$. The energy at which this transition starts depends on the specific properties of the neutrino source, but is typically $\sim$1 PeV for gamma-ray bursts.

Even in the case where the flavor ratio is 1:1:1, the neutrino to antineutrino ratio is not necessarily 1:1. For the pγ interaction described in equation 2.1, the ratio of ν to $\bar{\nu}$ at source is 1:0 for electron neutrinos and 1:1 for ν_μ. After neutrino oscillations, one expects a flavor ratio of 0.8:0.6:0.6 for neutrinos and 0.2:0.4:0.4 for antineutrinos. For pp interactions, however, all neutrino to antineutrino ratios are 1:1 at source, leading to equal numbers of neutrinos and antineutrinos for all flavors. Although cross sections are somewhat different for neutrinos and antineutrinos, it is unlikely that

AMANDA or IceCube could distinguish between neutrino and antineutrino interactions in most cases. However, there is a large enhancement in the cross section for charged current e$\bar{\nu}_e$ interactions at around 6.3 PeV (the Glashow resonance) which creates a distinct difference between the ν_e and $\bar{\nu}_e$ spectra. Given a sufficiently large sample of astrophysical ν_e, the prominence of the Glashow resonance could thus be used to distinguish between pγ and pp neutrino production mechanisms.

Chapter 3

AMANDA

3.1 High Energy Neutrino Detection

As previously mentioned, the vast majority of neutrinos pass through the Earth without interacting at all, and thus cannot be detected. However, one will occasionally interact with a nucleon through the weak force with either a charged current or neutral current interaction, represented schematically by the following Feynman diagrams:

Figure 3.1: Charged Current (left) and Neutral Current (right) neutrino interactions

Here, l is one of the three lepton flavors, N is a nucleon and H is a hadronic shower. The W boson is the exchange particle for charged current interactions, while Z_0 is the exchange particle for neutral current interactions.

When neutrinos interact with a particle in the detector medium, their decay

products are observable by Cherenkov radiation. When the speed of a particle exceeds the speed of light in a given medium[1], Cherenkov photons are created by atoms in the surrounding medium as they quickly restore themselves to their ground state after being disturbed by the electromagnetic field of the passing particle [16]. This radiation is emitted in a cone with angle:

$$\cos(\theta) = \frac{1}{\beta n(\lambda)}. \tag{3.1}$$

This angle is approximately 41° in ice or water. One obtains a similar conical shape any time the source of a spherically propagating wave is moving faster than the velocity of the wave itself, as can be seen by the applying Huygen's principle. Analogies are thus often drawn between Cherenkov radiation for light and the wake of a boat in water. Cherenkov light is emitted over a large range of wavelengths, but it follows a λ^{-2} emission spectrum which puts the majority of its flux in the blue wavelength range, and thus it appears blue.

Naturally, the use of Cherenkov light as a method of detection requires a detector to be built in a transparent medium. Antarctic ice, such as that used in the AMANDA and IceCube experiments, is very useful as a medium for the detector because it is remarkably transparent and uniform for a natural medium, allowing a minimum of scattering and absorption of Cherenkov photons. The depth and size of the Antarctic icecap also allows for much larger instrumented volumes than would be feasible if placing detectors in an artificially constructed medium, such as the mines used by

[1]It can do this because the speed of light in matter is c/n (where n is the index of refraction of the medium) which is less than the "cosmic speed limit" c. Einstein is okay with particles traveling faster than light in ice or water, just not in vacuum.

Super-Kamiokande [9] and other lower energy neutrino experiments. This larger size is necessary because the expected event rates of astrophysical neutrinos are much smaller at higher energies and because higher energy neutrinos create events which emit light over longer distances, requiring a larger detector to adequately reconstruct the event.

Most other high energy neutrino experiments either abandoned (Dumand [17]), currently operating (Baikal [18]) or under construction (ANTARES [19]) use water rather than ice as a Cherenkov medium. Both media have advantages. Ice has a much longer absorption length than water, but also has a shorter scattering length [20]. This means that, other variables being equal, an ice Cherenkov telescope would have worse angular resolution than a water Cherenkov telescope because the photons have changed directions more by the time they reach the photomultiplier tube. On the other hand, the energy resolution should be better in ice because a lower percentage of detectable photons wind up being lost in the detector medium. Locations such as Hawaii and the Mediterranean are more accessible than the South Pole, which has a deployment season limited to a couple of months per year. However, using ice as a medium minimizes complications in reconstruction which can occur in water-based detectors. These complications include currents, radioactivity in the detector medium and bioluminescent marine life. The first of these causes the position of the detectors to vary significantly as a function of time, while the last two significantly increase background noise.

3.2 the Detector

The Antarctic Muon and Neutrino Detector Array (AMANDA) is a high-energy neutrino detector situated at the South Pole. It consists of 677 optical modules, each of which is composed of an 8 inch, 14 stage photomultiplier tube (Hamamatsu R-5912-2) and supporting hardware surrounded by a glass pressure sphere. These optical modules are buried in the ice on a total of 19 strings. Optical modules are spaced between 10 and 20 meters apart, depending on the string, and the entire array has a radius of approximately 200 meters.

The first 4 AMANDA strings were deployed in the austral summer of 1993-1994 at a depth of 800-1000 m below the ice. These are referred to as AMANDA-A. Unfortunately, the presence of bubbles in the ice at this depth means that scattering is too large to reconstruct the paths of muons, although the array was effective as a calorimeter [21]. In the austral summers of 1995-1996 and 1996-1997, 10 strings were deployed at a depth of 1500 to 2000m. These strings are collectively referred to as AMANDA-B10. Three more strings were deployed in 1997-1998 and and an additional 6 strings were deployed in 1999-2000. These strings included optical fiber readouts in addition to the standard twisted pair cables. The combination of AMANDA-B10 and these additional 9 strings is referred to as AMANDA-II. See Figure 3.2 for a schematic of AMANDA-A, B-10 and II.

The pulse output of each photomultiplier tube is approximately 1V per photoelectron, with an instantaneous dynamic range of 10-20 photoelectrons. After traveling upward through $\sim$2 km of cable, however, the typical amplitude is around 5-15 MeV. At the surface, this signal is enhanced by Swedish Amplifiers (SWAMPs). The

SWAMPs also serve to supply high voltage to the optical modules and decouple the signal from the high voltage (both are transmitted on the same cable). From the SWAMPs, the signal is fed at 25× gain into peak sensing analog to digital converters (ADCs). As a parallel process the signal is amplified by 100×, fed through a discriminator and time to digital converter (TDC), and finally through a digital multiplicity adder (DMAD). The DMAD is used to produce a multiplicity trigger, which requires at least 24 OMs to fire simultaneously to register an event. The hardware is set up so that the ADCs are sensitive to pulses within $\pm 2\mu$s of the trigger time while the TDC can record information for up to 8 pulses per optical module in a window of 32μs around the trigger time [22].

The successor to AMANDA is called IceCube. As of February 2007, IceCube consisted of 22 strings. The first string was deployed in January of 2005, 8 strings were deployed in the austral summer of 2005-2006, and 13 additional strings were deployed in the 2006-2007 season. IceCube will eventually be comprised of between 70 and 80 strings and have an instrumented volume of roughly 1 km^3, with roughly 17 meters between modules. IceCube will also work in coordination with IceTop, a 1 km^2 surface air shower array, which employs digital optical modules frozen within tanks of ice. Due to both the larger number of optical modules deployed and wider string spacing, IceCube will have an instrumented volume two orders of magnitude greater than AMANDA. In addition, IceCube employs larger photomultiplier tubes and more advanced technology, including digital optical modules which house data acquisition software which digitizes signals within the detectors themselves. This technology was prototyped on strings 18 and 19 of AMANDA. AMANDA itself was

officially integrated into IceCube in March 2005 and will continue to function as a lower energy subdetector of the IceCube array.

3.3 Detection of Different Neutrino Flavors

The most commonly studied neutrino signature in AMANDA analyses is the muon track (see Figure 3.3). If a muon neutrino decays via the charged current channel, it will produce a muon traveling in a direction within an angle of approximately 1 degree of the original neutrino. Muons lose energy due to Cherenkov radiation at a steady rate of about 0.2 GeV/cm. Additionally, higher energy muons suffer stochastic energy losses through bremsstrahlung and pair production, which appear as small bursts of light along the track.

The other neutrino signature which AMANDA can use is called a "cascade". Cascades occur when energy is imparted to multiple photons, leptons and/or hadrons, each of which produces more particles as it decays, resulting in a shower of particles. These decay products produce a roughly spherically-shaped mass of light in the detector (see Figure 3.3). There are two distinct types of cascade. An electromagnetic cascade is composed of leptons and photons, creating more particles through bremsstrahlung and pair production. In a hadronic cascade, hadrons are produced through strong force interactions. When hadronic cascades pair produce or create γ-rays, these particles will produce electromagnetic cascade subcomponents. Overall, hadronic cascades emit roughly 80% as much light as electromagnetic cascades.

Compared to cascade analyses, muon searches have higher overall neutrino effective areas because the long track-length of muons allows AMANDA to pick up tracks which originated far away from the detector, whereas cascade events must originate

at least partially within the detector radius. Muon analyses can also use spatial constraints to reduce background because their track-like shape gives them much better pointing resolution. Since only neutrinos can travel through the entire Earth, muon analyses are able to cut out the majority of the background by only taking upward-traveling events. The only remaining background is thus atmospheric neutrinos and downgoing events whose direction has been misreconstructed. Directional reconstructions can use tighter angular cuts to reduce background even further for muon analyses which search for neutrinos from specific sources.

However, the cascade channel also has advantages. While ν-induced μ tracks are only caused by charged current ν_μ interactions, cascades can be produced by interactions of all 3 neutrino flavors. Processes producing cascade signatures include $\nu_x N$ neutral current interactions of any neutrino flavor, $\nu_e N$ or $\nu_\tau N$ charged current interactions and $\bar{\nu}_e e^-$ at 6.3 PeV (the Glashow Resonance). Since cascades are topologically distinct from AMANDA's primary background of atmospheric muons, it is not necessary to use the Earth as a filter, so cascade analyses have full (4π sr) sky coverage, as opposed to 2π sr for muon analyses. This doubles the number of potential neutrino sources that are able to be analyzed.

ν_τ are a unique case. If the τ decays into an electron (18% branching ratio) it produces a typical cascade, indistinguishable from an electron neutrino signature. If it decays into mesons (about a 64% branching ratio), but its energy is below 100 TeV the situation is similar since the track that is produced is $<$5 m and generally indistinguishable from the cascade [23]. It is possible, however, in a very energetic τ cascade to recreate an energetic τ which travels some distance before producing

a second particle cascade. This is commonly referred to as a "double bang event" and would provide a unique means of clearly identifying a ν_τ event [24]. A related signature is the "lollipop", which is a partially contained double bang event in which a single cascade and a τ track (the stick of the lollipop) are visible in the detector [25]. Neither of these signatures are visible using AMANDA because the detector's volume is insufficient. It is hoped however that this phenomenon will be identifiable with IceCube (see Figure 3.4).

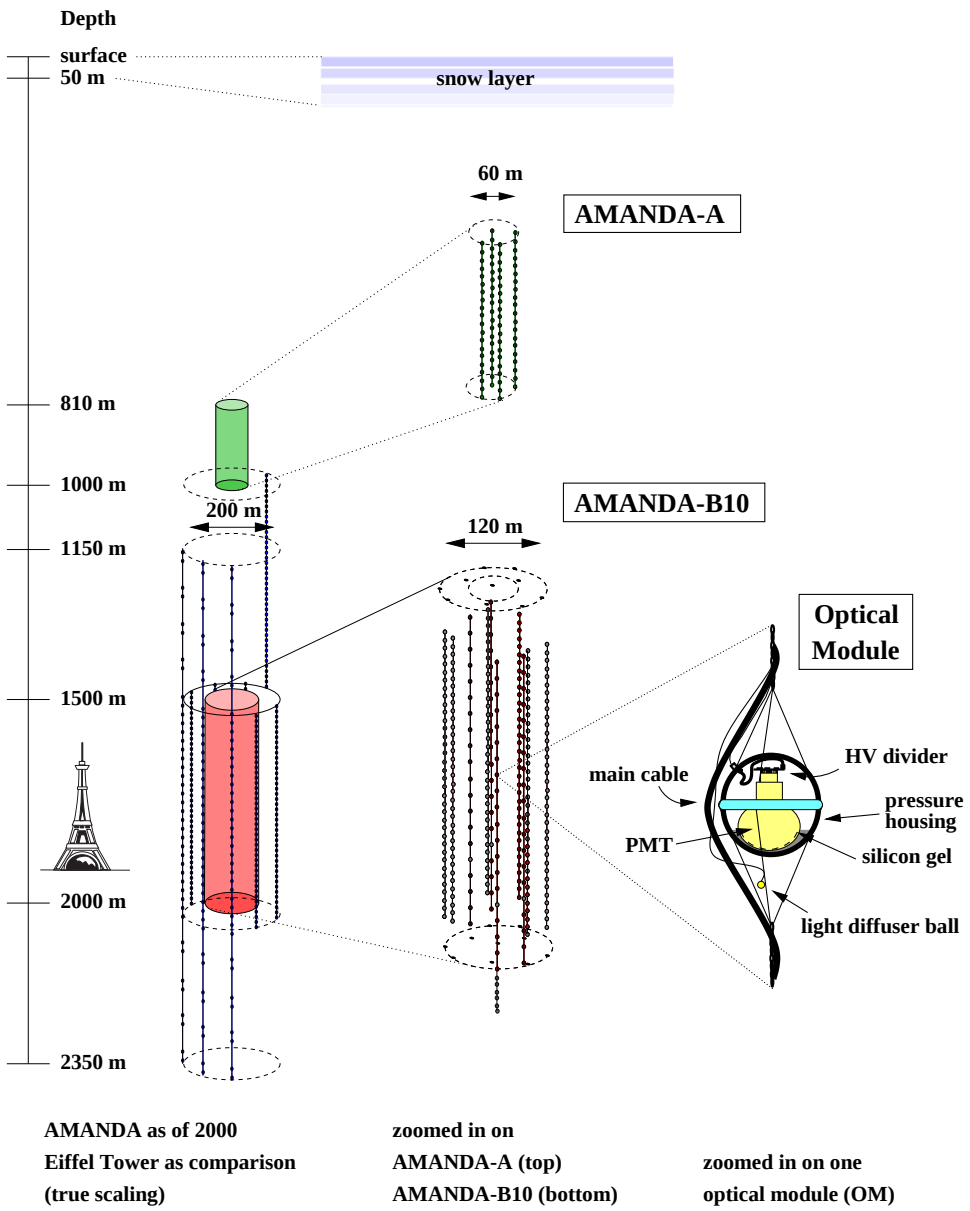

Figure 3.2: A schematic drawing of the AMANDA detector

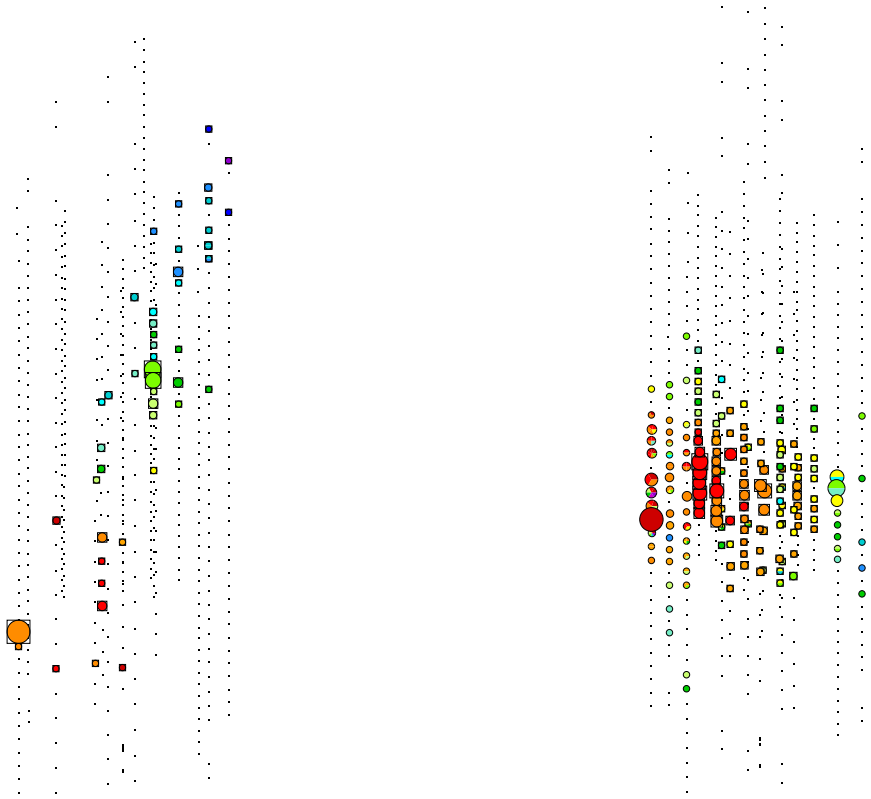

Figure 3.3: Muon (left) and cascade (right) signatures in the AMANDA detector.

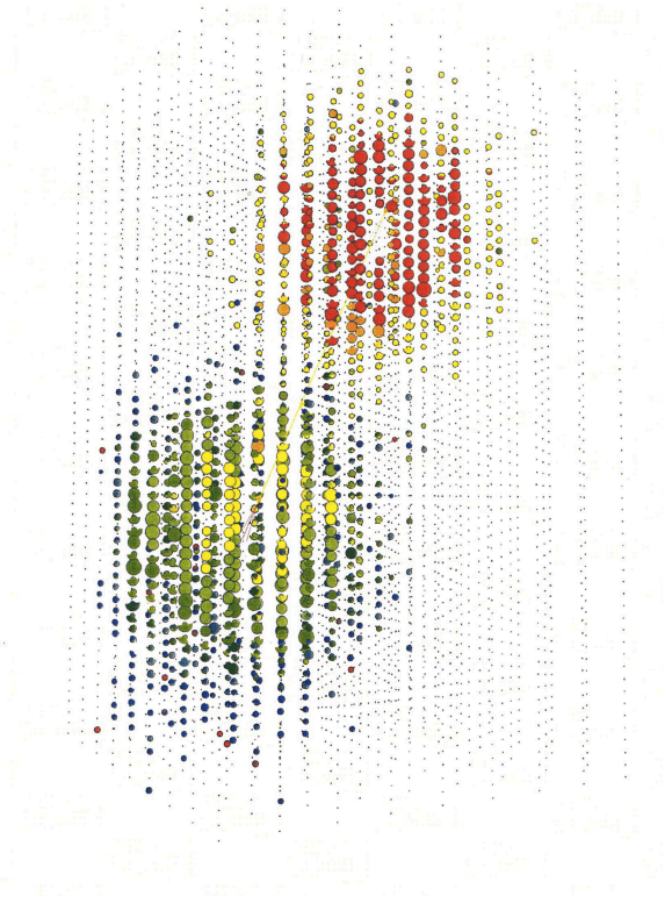

Figure 3.4: A tau double-bang event simulated in the IceCube detector

Chapter 4

Gamma Ray Bursts

4.1 A Brief History of GRB Observations

Gamma-ray bursts (GRBs) were discovered by the Vela satellite network in the late 1960s. Vela was a series of military satellites monitoring Soviet compliance with the nuclear test ban treaty using optical, x-ray and γ-ray detectors. When calibrating their detectors by turning them skyward, they were surprised to find γ-ray signals coming from space. After the information was declassified, 16 gamma-ray bursts detected by Vela satellites were reported in 1973 [26]. Not long after this, the IMP-6 satellite determined that the photon spectrum for GRBs peaked in the gamma-ray range, rather than simply being the tail end of a lower energy distribution [27].

GRBs remained very mysterious phenomena for the next couple of decades. Starting in 1991, the Burst and Transient Source Experiment (BATSE) aboard the Compton Gamma Ray Observatory collected data which greatly expanded what was known about GRBs. One of the most important discoveries was the isotropic distribution of bursts at all luminosities (see Figure 4.1). This distribution implied that GRBs were cosmological in origin, rather than originating in our own galaxy [28] as

previously thought. This was surprising because, based on experimental observations, GRBs originating at cosmological distance scales from Earth must be almost unbelievably energetic, in the range of 10^{52} to 10^{53} ergs. Additionally, BATSE was able to measure the duration of GRBs. The approximate burst duration as measured by BATSE is called T_{90}, defined as the time during which the central 90% of the gamma ray emission occurs. See Figure 4.2 for a plot of observed T_{90} times.

The Italian satellite Beppo Sax was the first to identify longer wavelength afterglows of GRBs, with photons in the x-ray, optical and radio wavelengths. Beppo Sax data allowed the Hubble Space Telescope to identify the host galaxies of some GRBs, providing further evidence supporting their cosmological origin [29]. Up to this point there was still some speculation that the observed isotropic burst distribution could have come about if GRBs originated in the Oort cloud of our own solar system [30].

NASA's Swift satellite began operation in November 2004. Because Swift's sky coverage is only about a third of BATSE's, it identifies fewer bursts. However, it is able to provide a great deal of information about each burst in multiple wavelengths. One of its chief aims is to determine the origin of GRBs, and when used in concert with ground-based observatories, is capable of directly measuring redshift values for $\sim$25% of bursts it identifies [31]. GRBs have been observed with redshifts as far away as z=6.3 [32] and as close as z=0.0085 [33]. Measured redshift values are consistent with models wherein the frequency of GRBs is roughly consistent with the star formation rate [34].

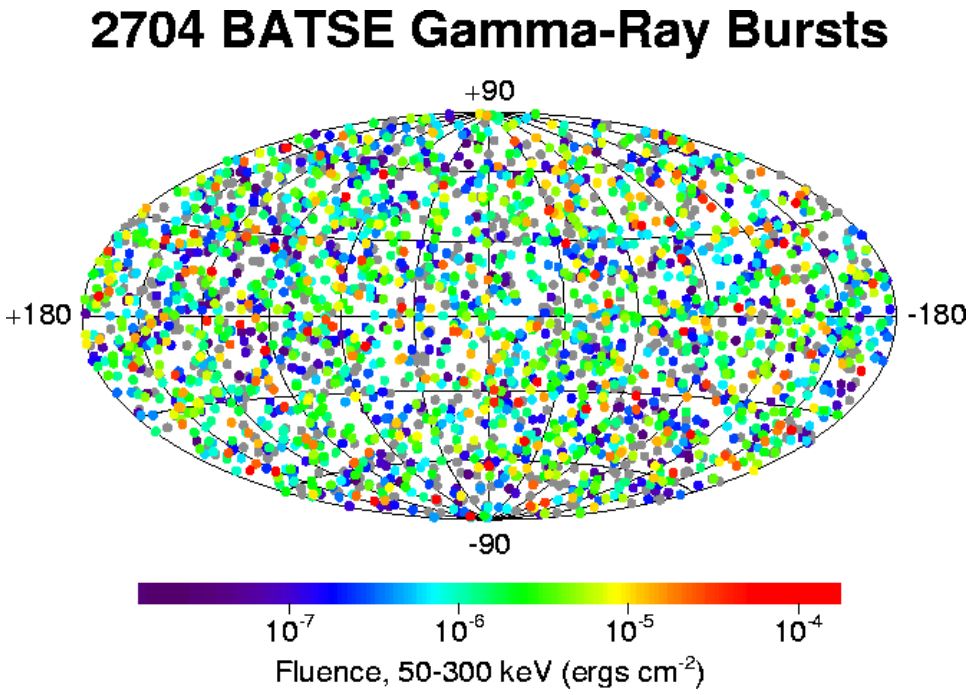

Figure 4.1: Isotropic spatial distribution of GRBs from the BATSE catalog, demonstrating cosmological origin of GRBs. GRBs originating in our own galaxy would clump along the galactic plane, at least in the case of the more distant fainter bursts (lighter dots in this picture).

4.2 Properties of GRBs

Much about GRBs is still not known with certainty, but a coherent picture is gradually coming together. In this section, we discuss several more aspects of gamma-ray bursts and their progenitors.

4.2.1 Compactness and Relativistic Acceleration

There are short time-scale fluctuations in GRB light curves of scale δt on the order of a few milliseconds, implying that they came from compact objects of size $< c\delta t$. This compact size indicates that the GRB should be optically thick, a claim which is at odds with the observed non-thermal photon spectra. This contradiction

is historically referred to as the "compactness problem". However, if the source has a large Lorentz boost factor Γ, the photon spectrum is blue-shifted to a lower energy and the size of the object becomes $c\delta t\Gamma^2$, allowing a mathematically consistent picture of GRBs [7]. Each shock front within the GRB jet travels at a different velocity, but the required bulk (average) Lorentz boost factors are typically around $\Gamma \approx 300$.

4.2.2 Central Engines and Bimodal Distribution

The inner workings of the mechanisms which cause GRBs cannot be observed directly, but numerous theoretical scenarios have been proposed to describe these central engines. Based on the observed T_{90} times, GRBs appear to follow a bimodal distribution, with "long" bursts lasting more than 2 seconds and "short" bursts lasting less than 2 seconds [35] (see Figure 4.2). It is currently thought that the two classes of GRBs may have different progenitors, with short duration bursts resulting from neutron star - neutron star or neutron star - black hole mergers [36][37] and longer bursts resulting from hypernovae (the collapse of massive stars) [38]. The latter is referred to as the collapsar model, and should be accompanied almost simultaneously by a supernova. Based on the growing catalog of observations, additional classes of bursts have been proposed. For example, there may be distinct populations of low-luminosity and high-luminosity bursts [39].

The supranova model is a competing scenario for long bursts. This also involves the collapse of a massive star into a black hole, but requires a two-step process. First, the star collapses into a neutron star, triggering a supernova. After roughly a week to a month, the unstable neutron star then collapses into a black hole. It is this second collapse which causes the gamma-ray burst [40]. Currently, however the observed as-

sociations between supernovae and GRBs (e.g. GRB060218 [41] and GRB030329 [42]) show very little delay between the two, meaning that the collapsar model is currently strongly favored over the supranova model based on the experimental evidence.

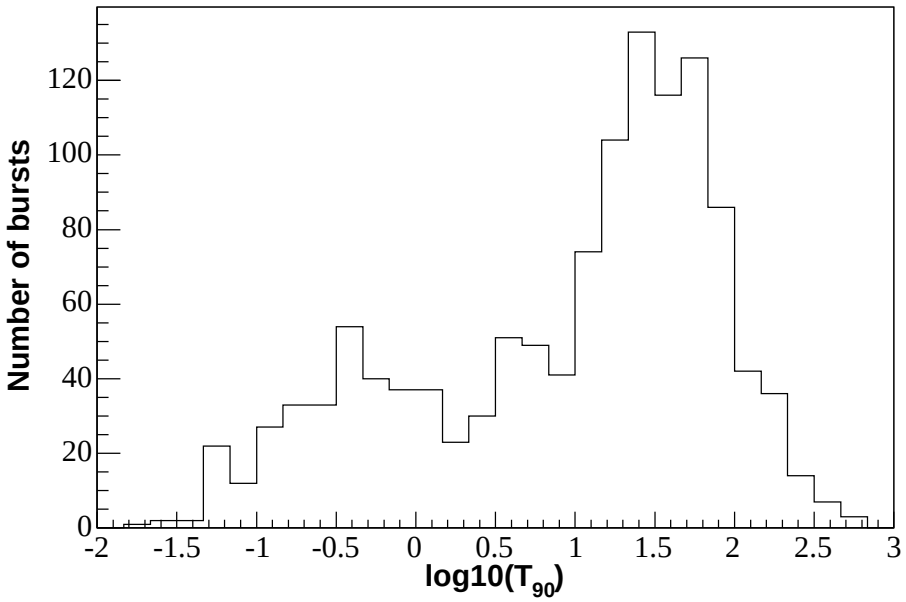

Figure 4.2: BATSE 4b catalog T_{90} times demonstrating bimodal distribution of GRBs.

4.2.3 Beaming

It is believed that GRBs are beamed. That is to say, the emission of GRBs occurs in two relatively narrow jets rather than isotropically. Physical evidence for beaming comes from the observations of GRB afterglows which gradually decay at first, then suddenly begin a more rapid dropoff [43][44][45]. This dropoff is explained by the Earth no longer being on-axis with the GRB jet. While beaming reduces the total energy requirement for each GRB from $\sim 10^{53}$ ergs to $\sim 10^{51}$ ergs, it increases the overall number of GRBs occurring by the same factor, since only GRBs beamed

towards us will be directly observable [29].

4.3 Neutrino (and Photon) Emission From GRBs

The most successful and generally accepted model accounting for the observed properties of GRBs is the fireball shock model [46], which applies regardless what the central GRB engine is. In this model, protons are Fermi accelerated by internal and external shocks resulting from a collimated relativistic fireball. Neutrino emission, along with photon emission, is predicted to occur at various stages of the GRB.

4.3.1 Prompt Emission

Prompt neutrino emission occurs in coincidence with the gamma-rays of the GRB, through pγ interactions (equation 2.1) within the relativistic jets of the GRB itself. Since shocks are caused by turbulence within the GRB jet, the difference in velocity between the two sides of the shock front is not great, even though the velocity in the observer's frame is quite large. Thus, shock acceleration at this stage is only mildly relativistic.

The prompt photon spectrum is generally fit by a Band function, which models the energy spectrum as a broken power law [47]:

$$N(\nu) = N_0 \begin{cases} (h\nu)^{\alpha} exp(-\frac{h\nu}{E_0}) & \text{for } h\nu < (\alpha-\beta)E_0 \\ ((\alpha-\beta)E_0)^{\alpha-\beta}(h\nu)^{\beta} exp(\beta-\alpha) & \text{for } h\nu > (\alpha-\beta)E_0 \end{cases} \tag{4.1}$$

where α and β are the two spectral indices, which vary from burst to burst. The predicted neutrino spectrum, however, contains two 'break energies' at which the spectrum changes slope. This spectrum is:

$$E^2\frac{\mathrm{d}\Phi}{\mathrm{d}E} = \frac{f_\pi}{8\epsilon_e}\frac{F_\gamma}{ln(10)}\begin{cases} (E/E_b)^{-\beta-1} & E < E_b \\ (E/E_b)^{-\alpha-1} & E_b < E < E_\pi \\ (E/E_b)^{-\alpha-1}(E/E_\pi)^{-2} & E > E_\pi. \end{cases} \quad (4.2)$$

The lower break energy, E_b, occurs because of the break in the photon spectrum, since the neutrino energy is directly impacted by the γ-rays which produce it. The higher energy break, E_π, results from synchrotron energy losses of the pions which produce the neutrinos [48] and therefore applies only to the neutrino spectrum. Break energies and spectral slopes will vary significantly from GRB to GRB due to varying distances, energies, Lorentz factors, et cetera, but "typical" values, as estimated in [48] and elsewhere are 10^5 and 10^7 GeV for the two break energies, with spectral slopes α=-1 and β=-2 (see Figure 4.5). Further details for modeling neutrino flux with this method, including specific parameters for two sample bursts, are provided in Appendix E.

Murase and Nagataki have produced more detailed models of neutrino emission, using three different sets of burst parameters [49]. While one of the sets (set C) uses assumed values which are too extreme to be representative of all bursts, set A produces a predicted neutrino flux similar to that predicted by Waxman-Bahcall, although arrived at by different calculations. Applying the MSN oscillation matrix to predicted spectra for ν_e and ν_μ[1] [50] at source, Ignacio Taboada has obtained predictions for all neutrino flavors, treating neutrinos and antineutrinos separately. The somewhat simplistic flavor ratio assumptions made when testing other spectra are therefore not needed in this case. These predictions are shown in Figure 4.3 . This neutrino flux uses

[1]As discussed previously, the pγ production mechanism is not expected to produce any ν_τ at source. Any production of tau neutrinos will be suppressed by several orders of magnitude relative to the other two flavors. Since, according to the best available mixing parameters, ν_μ and ν_τ are fully mixed at astrophysical distances, their predicted spectra at Earth are identical.

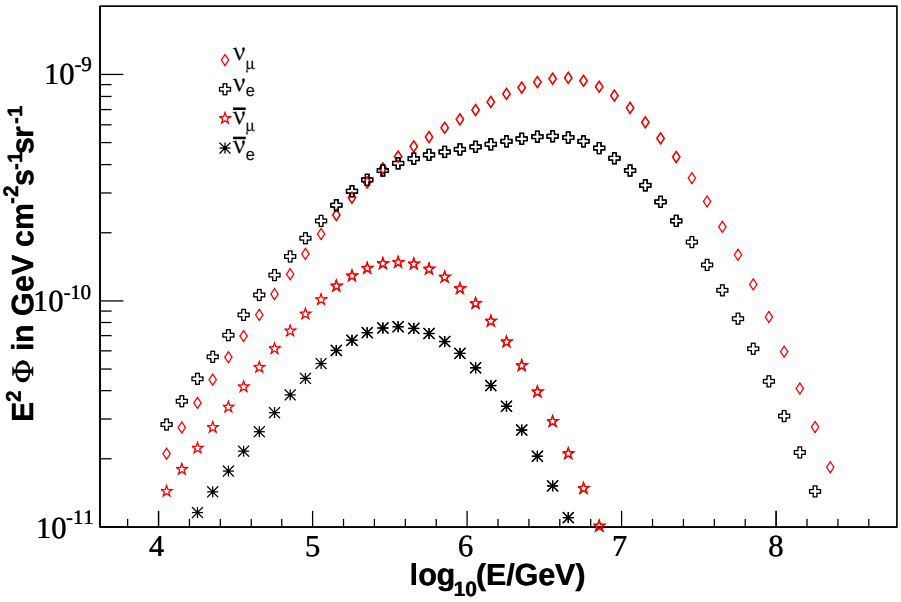

Figure 4.3: Neutrino flux at Earth for Murase and Nagataki Model A. ν_τ spectral predictions are identical to ν_μ.

a burst distribution based on satellite observations from BATSE and other detectors (with a total rate of ∼690 bursts per year). However, the predicted flux is not much different if the burst rate is tied to the star formation rate and integrated out to a redshift of z_{max}=7 (see Figure 4.4), so the selection effects are not too significant.

In the supranova model of emission [51] [40], one can also get substantial neutrino emission from jet interactions with photons in the pulsar wind bubble external to the jet. This would create a separate spectrum of neutrino emission in addition to the Waxman-Bahcall spectrum which would arrive simultaneously with the burst (see Figure 4.5).

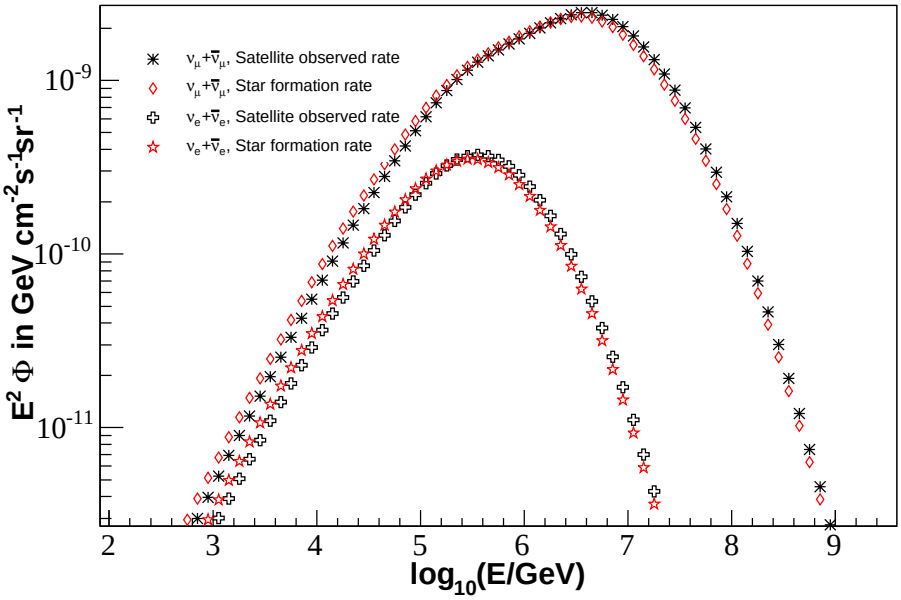

Figure 4.4: Neutrino flux predicted by Murase and Nagataki Model A [49] at source for ν_μ and ν_e. Two different redshift evolutions are assumed, one based on the burst observations of γ-ray satellites and the other based on the star formation rate integrated out to z=7. Since the bulk of the neutrino flux is predicted to come from relatively nearby bursts, the difference in the net neutrino flux between the two assumptions is minimal.

4.3.2 Afterglow Neutrino Emission

After the initial burst of gamma-rays, afterglow photon emission on longer time scales has been observed for many bursts in the x-ray, optical and radio bands, in many cases enabling direct measurements of redshift and identification of the host galaxy. Waxman and Bahcall have also theorized an ultra-high energy neutrino afterglow spectrum coming from "reverse shocks" which result from the interaction between protons in the GRB's relativistically expanding fireball and the photon field in the surrounding medium. In this case, the shocks are ultrarelativistic, since the two sides of the shock front (the jet and the surrounding medium) are moving at vastly different speeds. The predicted afterglow spectrum can be seen in Figure 4.5. Synchrotron emission changes the photon spectrum above a fixed energy, leading to the observed break in the predicted neutrino spectrum [52].

4.3.3 Thermal Neutrinos

Many low energy thermal neutrinos (MeV range) are also predicted by some models, such as the collapsar and neutron star merger models. These are not beamed like the neutrinos occurring within the relativistic GRB jet, but rather are emitted isotropically. Along with gravitational waves emitted at the same time, these carry with them a considerable fraction of the entire system's energy. However, these neutrinos are not detectable at cosmological distances and would be indistinguishable from neutrinos created in an accompanying supernova [7].

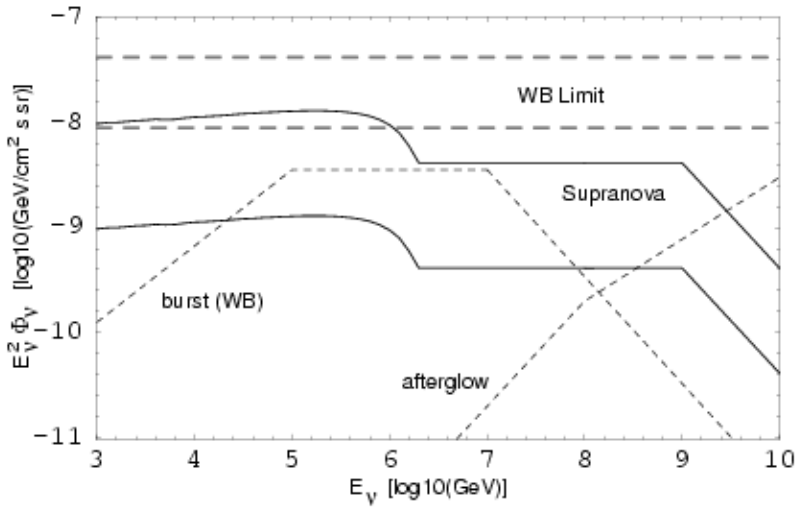

Figure 4.5: Prompt and afterglow neutrino emission spectra (dotted lines) from Waxman and Bahcall paper [48] Also shown is diffuse flux prediction for the supranova model (solid) assuming all (top) or 10% (bottom) of GRBs have accompanying pulsar winds. The flux is for ν_μ, but has not been adjusted for neutrino oscilations. This plot is borrowed from [53].

4.3.4 Precursor Neutrinos

In the case that a GRB results from the collapse of a massive star, there may be a precursor neutrino spectrum which is quite different from the spectrum expected from prompt emission. The process producing precursor neutrinos occurs internally within a GRB jet, just as in prompt emission, but occurs as the jet is still propagating within the stellar body itself. This alters the neutrino spectrum and, because the inside of the star is optically thick to γ emission, means that the neutrinos are not accompanied by a photon signal. The predicted spectra for precursor emission can be seen in Figure 4.6 for two models. In the H model, the helium core of a star is surrounded by a hydrogen cloud. In the He model, this hydrogen cloud is not present. Precursor emission is expected approximately 10-100 seconds before prompt emission

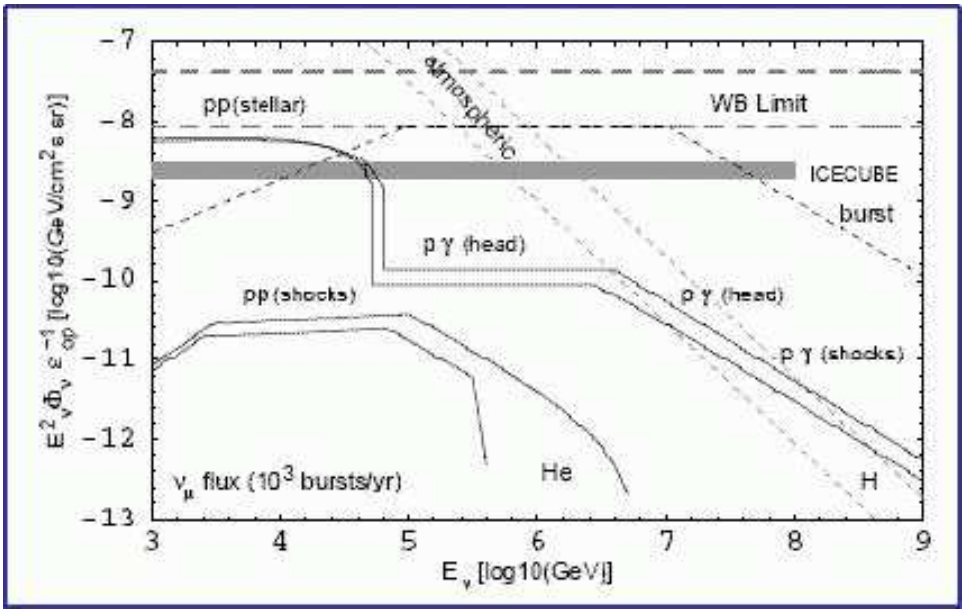

Figure 4.6: Precursor spectra predictions for stars with He and H layers (solid lines) with WB flux (dotted line), taken from [54]. Note that the flux in this plot is divided by $\epsilon_{\rm op}$, the fraction of jet energy dissipated in sub-stellar shocks.

[54].

4.4 Related Phenomena

4.4.1 X-Ray Flashers

X-Ray flashers occur on similar timescales to GRBs, but their photon spectra peak in the X-ray range. Optical afterglows have been observed from at least two X-ray flashers [7]. It is currently not clear whether these transients are just lower energy GRBs or if they are a distinct class of phenomenon. These are not promising neutrino sources under the collapsar model, since a small fraction of proton energy would be converted to pions, but the neutrino production under the supranova model

could be significant [55].

4.4.2 Choked Bursts

It is possible to generate the "precursor" spectrum described in the previous section without a subsequent GRB [54]. In the case of slowly-rotating or particularly large stars, the jet may produce neutrinos while still in the stellar body, but fail to get through the stellar envelope and therefore not produce a GRB. Since they have never been identified, the commonality of these "choked" bursts is unknown, but they may outnumber conventional GRBs by as much as a factor of 100 if their rate is tied to the rate of supernovae [56].

4.4.3 Mildly Relativistic Supernovae

It is possible that massive collapses which do not produce gamma-ray bursts may also produce neutrino spectra from jets with smaller Lorentz factors ($\Gamma \sim 3$ rather than $\Gamma \sim 100$). If one includes kaon as well as pion decays in neutrino production, this neutrino flux may be significant. The neutrino energies predicted, however, are at much lower energy than for a conventional burst, closer in energy range to an atmospheric neutrino spectrum, making their detection more difficult [57].

4.4.4 Soft Gamma Repeaters

SGRs are a distinct phenomenon from GRBs, thought to originate from the global magnetic rearrangement of the crust or interior of a magnetar (a type of highly magnetized neutron star). Like gamma ray bursts, soft gamma repeaters are transient gamma ray, and possibly neutrino, sources. SGRs, however, are known to have multiple flary periods, separated in many cases by several years, whereas a GRB is a

one-time-only event. They also have a softer photon energy spectrum than GRBs[2]. Four distinct SGRs have been observed so far. Neutrino predictions from SGR are not well determined, particularly since the baryon loading is not theoretically constrained as in GRBs. It is generally assumed however, that neutrinos would be produced in pγ interactions and would therefore have a simple power law energy spectrum, following the photon spectrum [58] [59] .

[2]Hence the name, soft gamma repeater.

Chapter 5

Overview of the Rolling Search Method

5.1 Summary of Technique

The concept of the rolling search is straightforward: starting with every surviving neutrino candidate event, we look in a predefined time window for additional surviving events. A clumping of events which is extremely unlikely to have occurred due to background fluctuations (modeling the background as a stochastic Poissonian process) is evidence of a neutrino signal from a transient source. Significance is evaluated accounting for trial factors incurred over the entire 3 year period, so careful data reduction is required (discussed in detail in Chapter 7). Since this analysis uses the cascade channel, no angular cuts are performed.

5.2 Comparison With Other GRB Analyses

Several AMANDA searches for GRBs have already been conducted, all of which have looked for neutrinos correlated with GRB γ-ray detections by satellites [29] [60] [61] [62] [63]. Compared to the rolling search, these have significant advantages in background rejection, since one must only worry about background during the time in

which the burst is occurring. This leads to a smaller number of events being required for significance. Additionally, if one has identified an individual burst, depending on what parameters were measured, it is possible to use spectral indices, redshift values and so forth to model each burst individually and get more accurate predictions about the neutrino rate of that GRB [64] [62] [55] (see also Appendix E). Since Swift directly measures redshift for a large percentage of bursts it identifies, this dataset will be particularly conducive to this individualized analysis. The majority of satellite-coincident analyses up to this point, however, have utilized the same averaged predictions that the rolling analysis uses.

On the other hand, satellite-coincident searches can't look for bursts which the satellites didn't see. Obviously, a rolling search is better equipped to identify γ-ray dark transients, but it also has the potential to see many GRBs missed by satellites. Since the loss of BATSE in early 2000, the rate of GRB detection by the IPN[3] network has been considerably smaller, approximately a rate of $\sim$1 burst per week rather than $\sim$1 per day in the case of BATSE. Swift has recently increased this rate, but its focus is on gaining a lot of information about each GRB it detects rather than detecting as many GRBs as possible. Swift's narrower field of view means it is still less prolific than BATSE, and BATSE itself only had $\sim 2\pi$ sky coverage at any given time[1]. At any rate, in the period over which this analysis was conducted, 2001-2003, which was between the eras of BATSE and Swift, the majority of GRBs went undetected. Additionally, if neutrino emission does not arrive simultaneously with prompt γ-ray emission, this

[1] In principle, even some bursts which were within BATSE's field of view but had photon signatures too weak to trigger the detector could still have been significant neutrino sources. However, currently favored theoretical models constrain the baryon loading factors within GRBs to a narrow enough range that neutrino and photon fluxes at Earth should be more-or-less directly proportional for conventional gamma-ray bursts.

may cause a triggered search to miss an observation, but will not adversely affect a rolling search.

Given worse per-burst sensitivity, but an increased number of possible targets compared to the satellite-coincident searches, it is best to view the rolling search as a useful complement to the analyses already conducted.

5.3 Selection of Time Windows

Since the distribution of GRBs is bi-modal, two time windows were selected: 1 second for the short burst class and 100 seconds for the long burst class. Because of the large amount of variation in the shapes of GRB light curves, it is not realistic to tune the cuts with great precision, but these choices are roughly optimized to make the best tradeoff between retained signal and background allowed in each window. Analyses utilizing rolling time windows performed by the Tibet Air Shower Array [65] and Milagro [66] utilize similar time windows. Although the 100 second time window truncates some longer GRBs, many of these longer GRBs still have a very large percentage of their photon flux within a 100 second time window. This is demonstrated, at least indirectly, by Figure 5.2. Figure 5.2 demonstrates that among the "long" burst population ($T_{90} > 2$ seconds) fluence and duration are only weakly correlated. Thus, we are not preferentially cutting away flux from the strongest bursts by using a time window which truncates some long GRBs. An approximate correction for the lost flux from very long bursts is applied when determining sensitivity.

Another possible method of selecting time windows would be to fit the two peaks of the bimodal distribution with gaussians and take the point of 1 sigma upward fluctuation. This doesn't change the decision much for the long burst set, but would

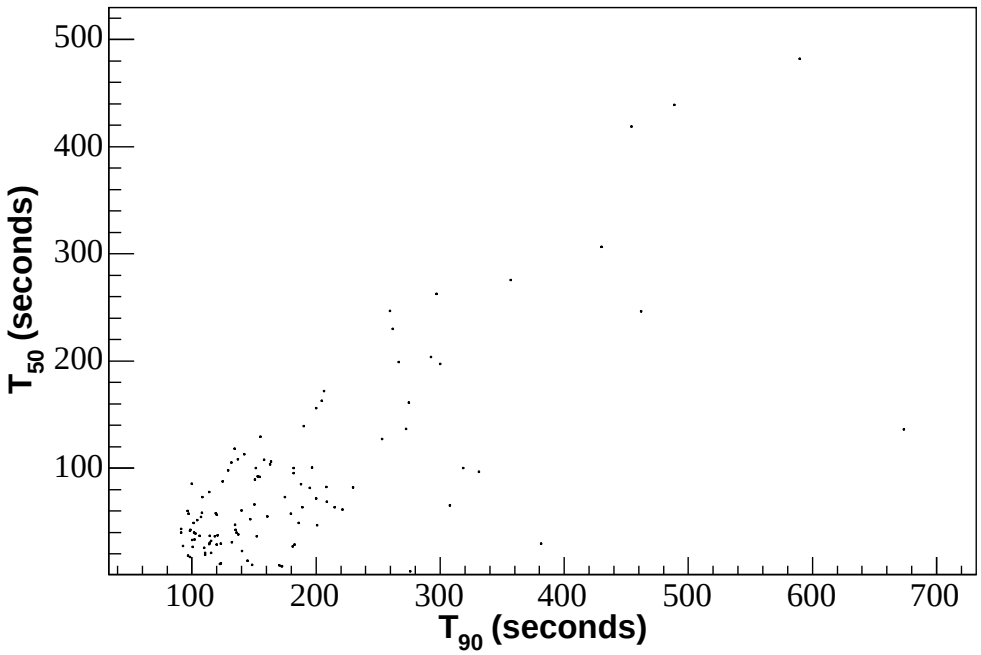

Figure 5.1: BATSE T_{90} times vs. T_{50} times for bursts with $T_{90} > 90$ seconds taken from the 4B catalog [35]. Many very long bursts still contain a substantial fraction of their flux within a much smaller time period.

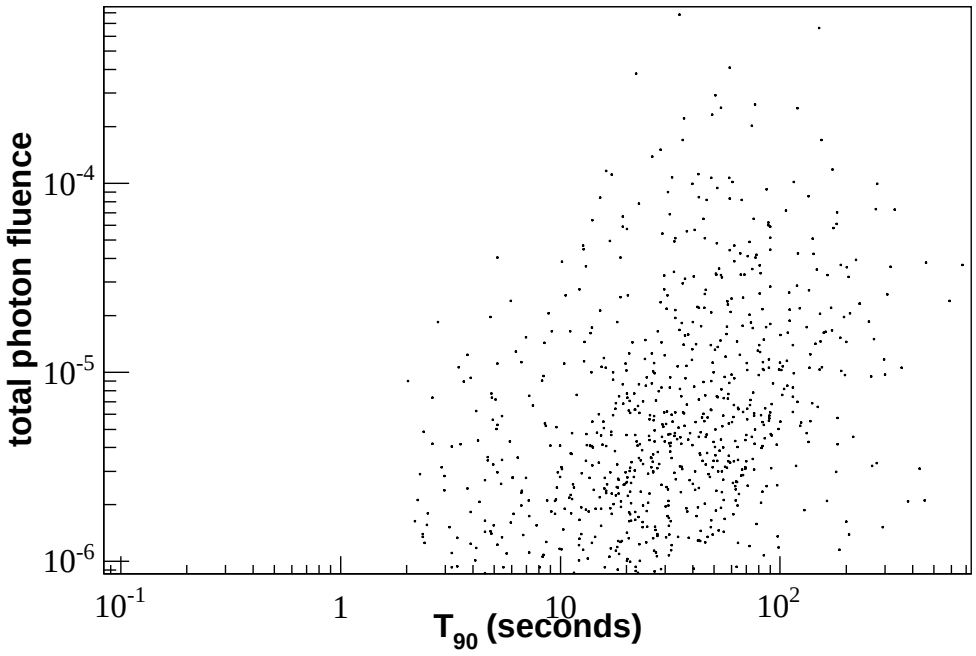

Figure 5.2: BATSE T_{90} times versus total photon fluence taken from the 4B catalog [35] for long (>2 second) bursts. The plot demonstrates that fluence is not a direct function of duration.

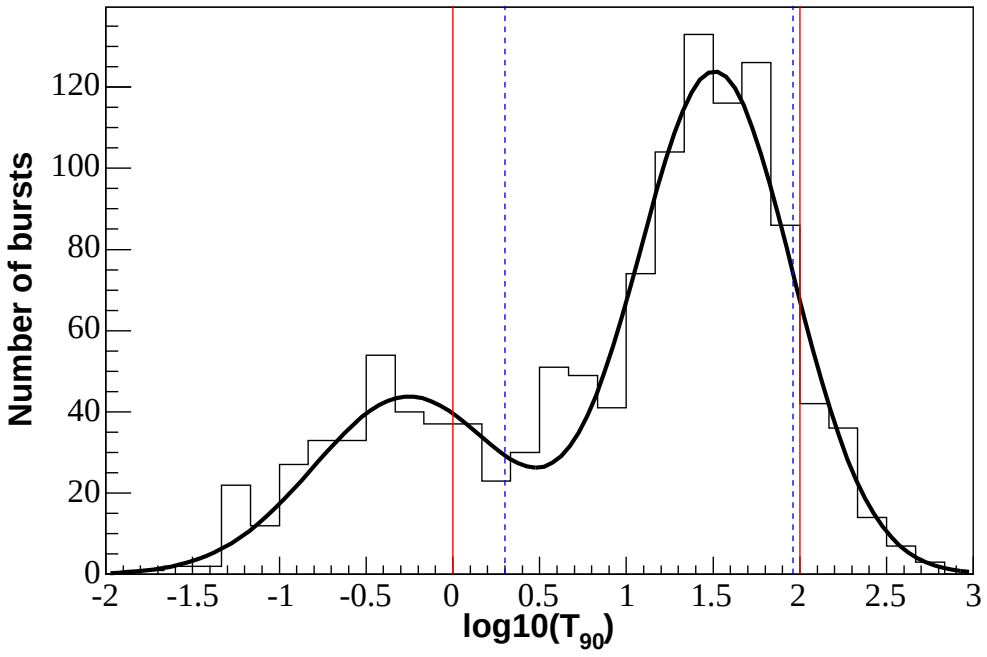

Figure 5.3: BATSE T_{90} times taken from the 4B catalog [35], clearly showing two burst classes. The black line is a double-gaussian fit to the data, solid vertical lines are the cuts actually taken, dotted lines are the 1 σ upward fluctuation points for the fit.

extend the choice from 1 second to $\sim$2 seconds for the shorter duration bursts (see Figure 5.3).

5.4 Picking the Right Rolling Search Method

Some consideration must be given to the exact method used to conduct a rolling search. Obviously, if one simply measures the number of events in consecutive, non-overlapping 100 second windows, one risks cutting a significant cluster of events into two smaller groupings. If the same technique is performed, but with overlapping windows (starting, say, every 10 seconds), one is less likely to miss a cluster of events,

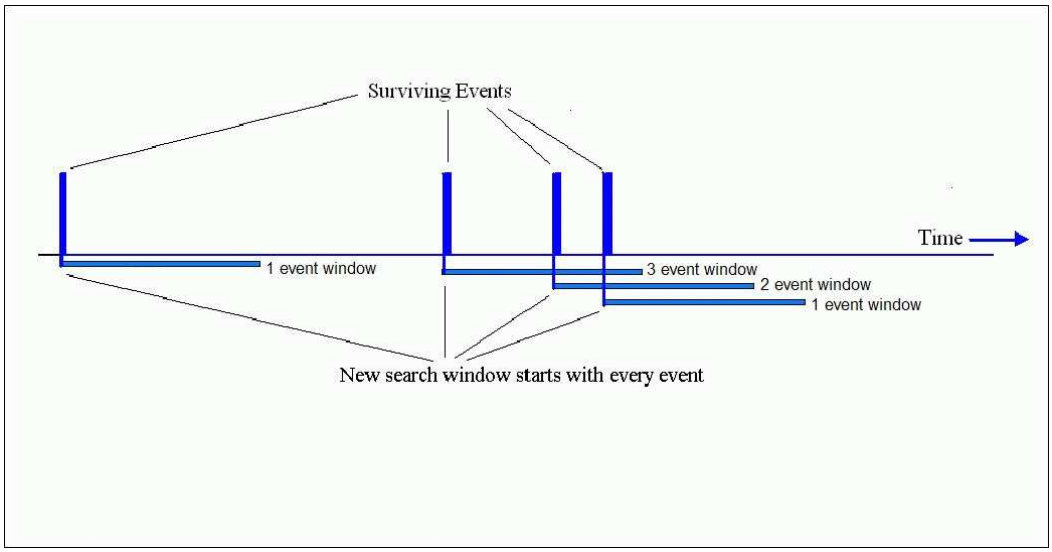

Figure 5.4: Schematic of the rolling search method.

but this is still a distinct possibility. Additionally, one introduces a complicated trials factor equation with each window coupled in a non-trivial way to 10 other windows. Thus, we have elected to start a time window at each surviving event, which guarantees that no significant cluster will be missed and allows simple calculations (since statistics are low enough that each window can be treated as an approximately independent trial). The sensitivities resulting from the overlapping windows method and the approach we have chosen are nearly identical, but for the above reasons starting a new window with each event is philosophically more appealing.

Chapter 6

Data Processing and Simulation

Now that some background and a general overview has been presented, the next few chapters present the technical details of turning some unfiltered sets of data into a completed rolling search analysis. This chapter covers the basics of data processing in AMANDA. Chapter 7 describes the cuts used to isolate the events we are looking for, and Chapter 8 discusses the statistical process of cut optimization.

6.1 File Selection

The same bad files which were omitted from the Zeuthen point source analysis file selection were omitted from this analysis. "Bad" in this context covers a range of problems, such as electronics failures, windstorms and unknown disturbances which prevent data from being usable. According to Zeuthen's standards, files are generally evaluated by requiring a high percentage of optical modules to have count rates within a few standard deviations of their average [67]. Additionally, the number of channels variable N_{channel}, which is defined as the number of optical modules with at least one hit[1], was checked to ensure a reasonable distribution in each run. Since the rolling

[1] A "hit" occurs each time an optical module is triggered by a photon.

search requires by its nature a stable and uninterrupted period of data, short runs under 4000 seconds were removed. Additionally, the austral summer seasons, during which time the South Pole station had a considerably higher population and work was being done on the AMANDA detector, were left out of the data sample. Runs 7219 and 7249 from the 2003 data sample were removed because bad files within these runs caused a very large number of gaps in the data. Run 3399, the final file in the 2001 sample, was omitted due to the unusual behavior in flare checking[2] variables.

6.2 Hit Cleaning and Filtering

The 2001 data set was filtered in Madison using the filtering and reconstruction package Siegmund [68]. The 2002 and 2003 data samples started with Henrike Wissing's filtering at Zeuthen, using the more recently developed Sieglinde [69] software. In spite of the differences in initial filtering, results between data sets are quite consistent.

Cleaning the runs so that they are ready to be used in analysis requires several steps. Dead or unreliable optical modules are removed from the analysis, using the standard AMANDA-II bad OM list for each year [67]. Hits outside a time window of -2 μs to +4.5 μs around each event are also eliminated. This is larger than the time-span of an event, but removes most PMT noise and reduces PMT afterpulsing, which typically occurs on a scale of $\sim$6 μs. Isolated hits (those without another hit within 500 ns and 70 m) and hits with small amplitude (ADC$<$0.3 in 2001 and ADC$<$0.1 in 2002 and 2003) are removed as well, which reduces cross-talk and noise hits.

Since cross-talk still remains after this basic cleaning, a dedicated filter to reduce

[2]Flare checking is explained in section 6.3.

electronic cross-talk was applied. The first part of the cross-talk filter consists of TOT cuts individually tailored to each optical module and recalbirated each year. Additionally, 2 dimensional ADC vs. TOT cuts are applied to each OM and a cross-talk map is used to remove cross-talk between the top and bottom of strings.

6.3 Flare Checking

The procedures described above do a good job of removing noise and cross-talk hits for valid events. However, due to occasional high winds, external electromagnetic emission and other factors, entire "non-physical" events can sometimes show up in AMANDA data which are an artifact of the detector and not caused by an actual particle detection. Non-physical events are colloquially referred to as "flares" in AMANDA and IceCube. In this analysis, it is very important to remove flary events. This is true not just because they are an unwanted source of additional background, but, more importantly, the distribution of flary events cannot be represented by the same Poissonian distribution as surviving events which result from actual particles. It is therefore conceivable that a clustering of non-particle events could register as a signal. Flare checking software, developed by Arvid Pohl, can be used to identify the likelihood of an event being of non-particle origin according to 9 different observable parameters, referred to as flare checking variables. Definitions of these nine variables are as follows:

Variable Name	Description
only_adc	number of hits with ADC values but no leading edges
missing_channel	number of channels with a missing leading or trailing edge
nchannel_dead	number of OMs marked as dead which have hits in them
short_M	hits which are too short among a particular class of OMs
short_H	hits which are too short in hybrid and coaxial OMs
long_noise	hits with long TOT that have leading edges in the noise region
long_missing	hits with long TOT in a subevent missing the leading edge in the first hit or trailing edge in the last hit
induc_B10	compares hits in the twisted pair strings 5-10 to the on-time hits in coaxial strings 1-4 to look for inductance related events
induc_1119	similar to induc B10, but for AMANDA-II strings 11-19

More detail is available in [70].

Flare checking values are normalized according to the base-10 logarithm of their probability, so that 1 event in 10 will have a value above 10, 1 event in 100 will have a value above 2, and so forth. A sample that has no cuts and is undisturbed by non-particle events thus normally yields an exponential distribution. This distribution can be upset by non-particle disturbances, which don't fit into this exponential pattern and can also be thrown off by cuts which naturally select higher values in certain variables. In order to correctly assign values, the flare checker must be run on a data sample at the minimum bias level, before any cuts are made. The flare checking cuts themselves, however, can then be applied at a later stage of the analysis. Some events, particularly in this high energy analysis, have values outside the range for

which the flare checking cuts are normalized. These events receive a value of -1 and are considered unclassifiable by the flare checking software. Adopting a conservative approach towards removal of events which may or may not be flary, these events are kept in the sample.

The first step in flare checking is to remove the events which are obviously outside of the expected exponential distribution of events, restoring the distributions to their proper shape. This is done visually, starting with the clearest cut and working consecutively from there. The cuts for 2002 and 2003 are induc_B10<16, induc_11<8 and missing_channel<14. The cuts used for 2001 are induc_B10<16, induc_11<8 and short_M<14. See Figures 6.1 to 6.3 for plots demonstrating these cuts.

After this step is completed, the top 1% of flare checking values are eliminated for those variables whose distributions are not changed by tightening cuts, since it is inferred that real signal will not be preferentially cut away. These were found to be long_noise, long_missing, nchannel_dead, induc_11 and missing_channel. The remaining variables demonstrate energy-dependent selection effects, meaning that as cuts tighten, more of the high value events are retained. This step is therefore not performed using these variables, since cutting 1% of surviving events may in fact be reducing signal retention by a much larger amount. This procedure follows the "extended" procedure recommended in Arvid Pohl's flare checking proposal [71]. Plots of the distributions at various cut levels are found in Figures 6.4 to 6.6.

The flare checking cuts were designed to identify non-particle events, and legitimate signal events will not on average have higher average values for the 9 flare checking variables relative to normal background events (aside from the energy corre-

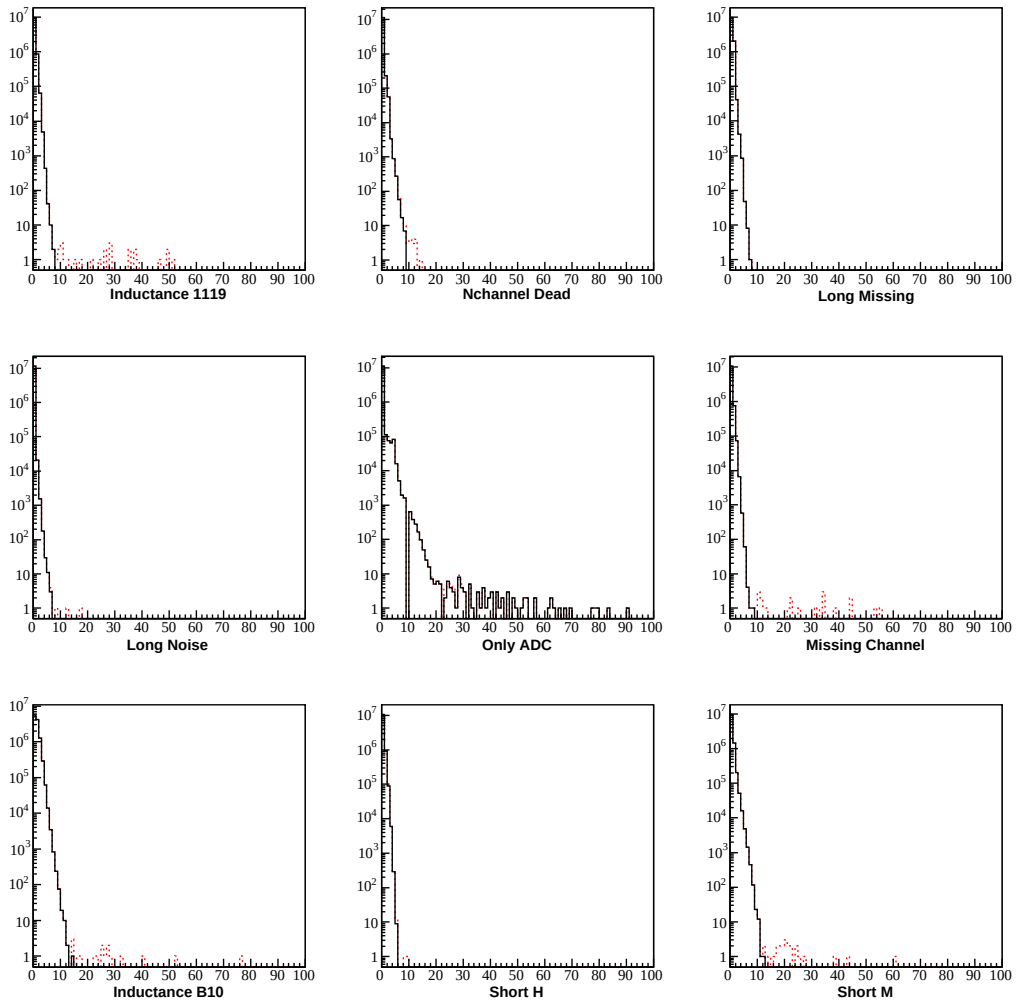

Figure 6.1: Flare checking variables for 2001. Solid lines show kept events, dotted lines show events removed by cuts.

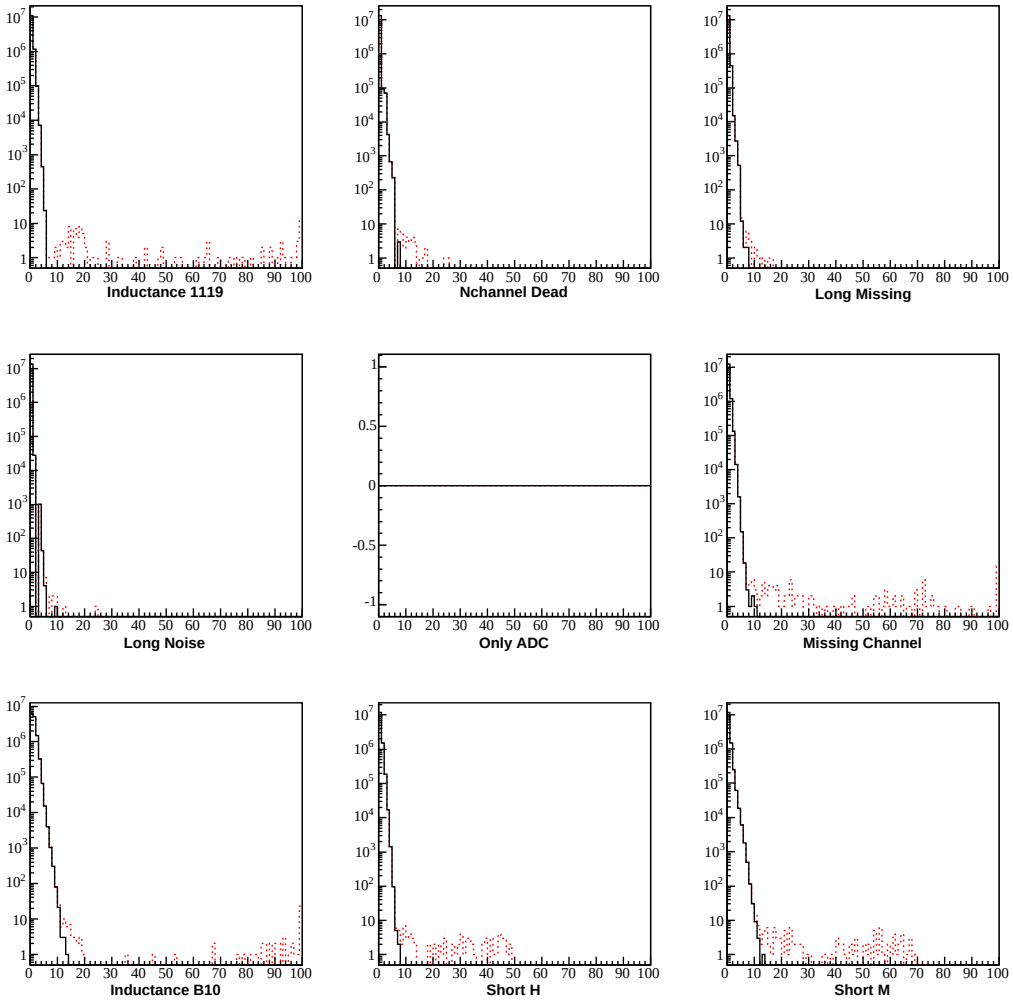

Figure 6.2: Flare checking variables for 2002. Solid lines show kept events, dotted lines show events removed by cuts.

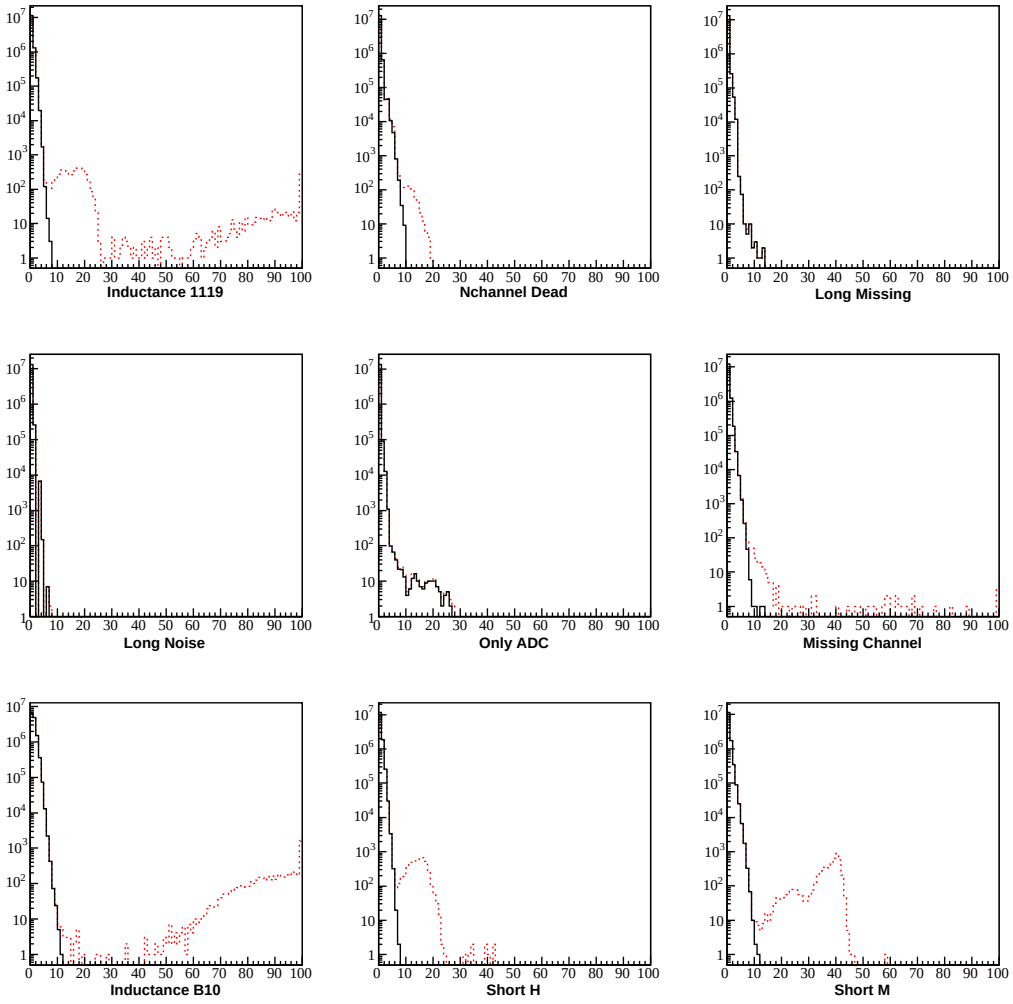

Figure 6.3: Flare checking variables for 2003. Solid lines show kept events, dotted lines show events removed by cuts.

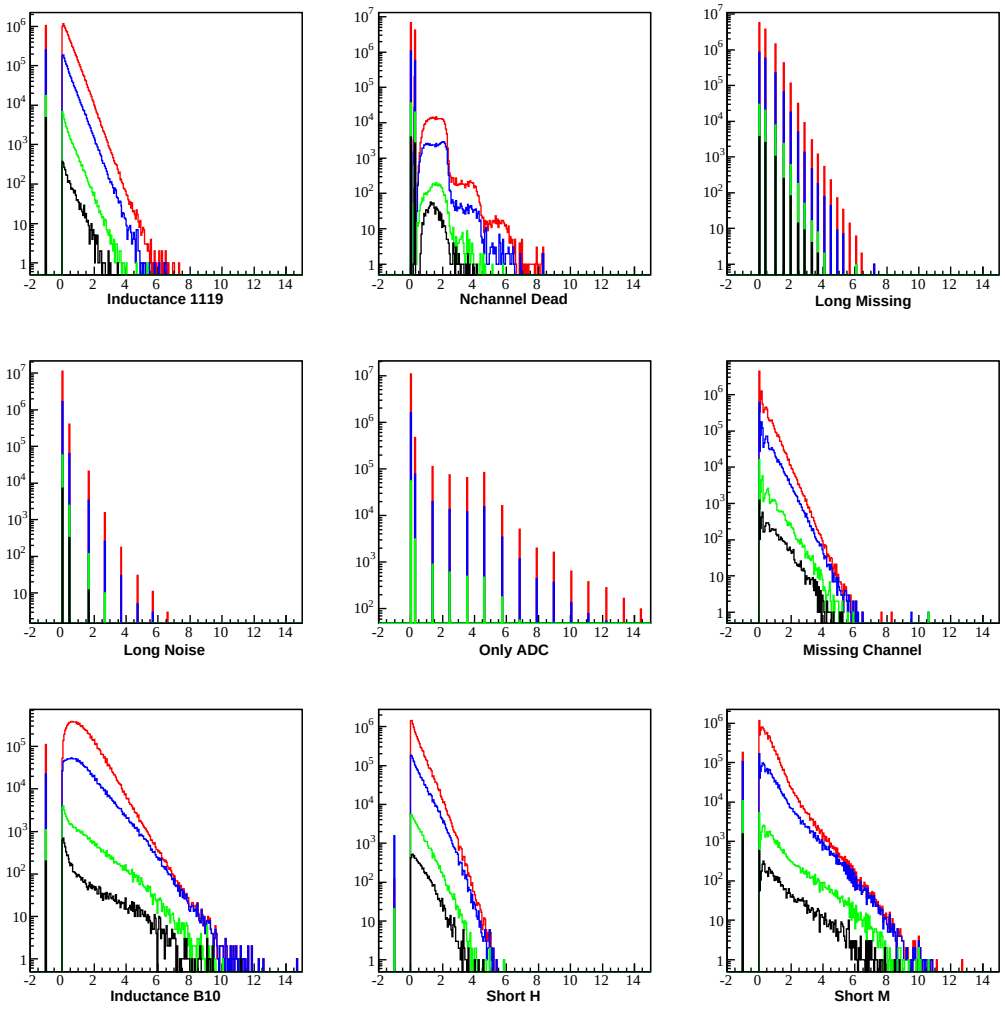

Figure 6.4: Flare checking variables for 2001 at various cut levels. In decreasing order these are: high energy filter, direct hits cut, loose support vector machine and tighter support vector machine. The first five variables, which show no noticeable selection effects, are used for extended flare checking cuts.

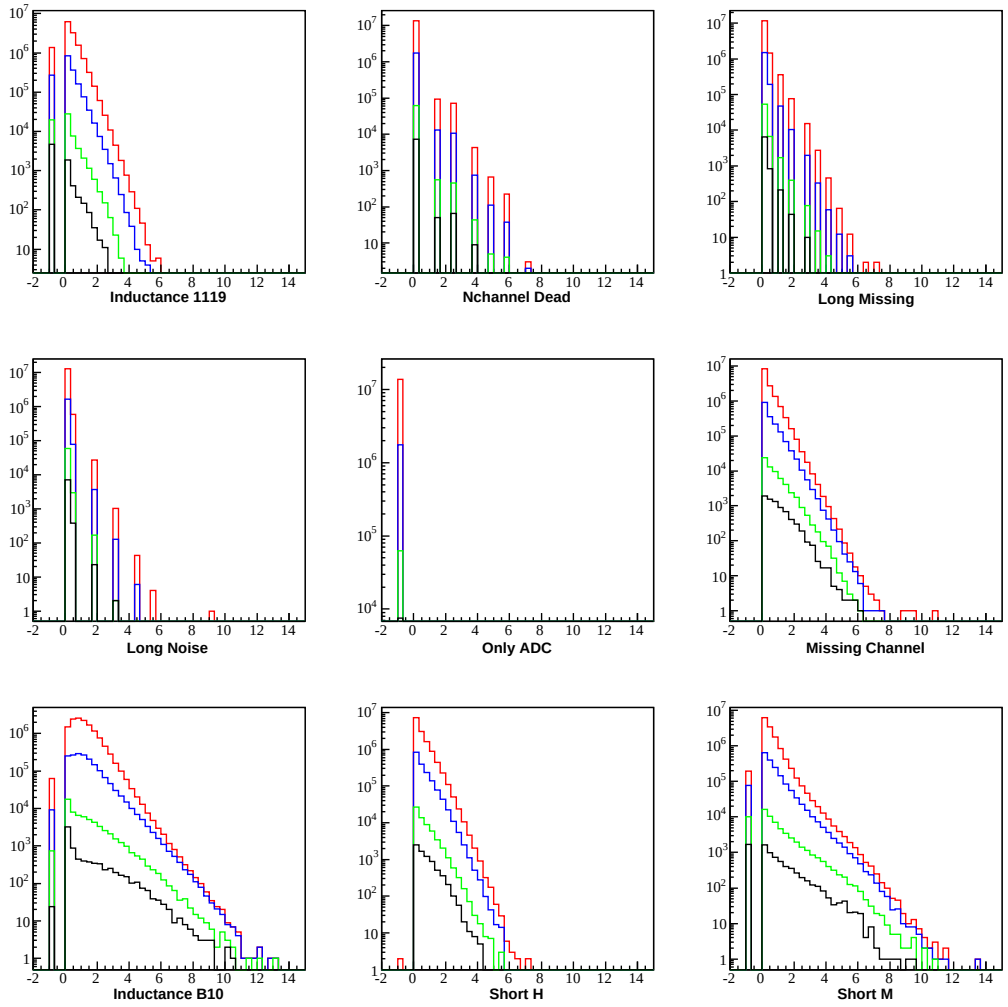

Figure 6.5: Flare checking variables for 2002 at various cut levels. In decreasing orders these are: high energy filter, direct hits cut, loose support vector machine and tighter support vector machine. The first four variables, which show no noticeable selection effects, are used for extended flare checking cuts. (Note that for unknown reasons, the variable only_adc has a uniform value of 0 in 2002 and is therefore not used for this year. I am unable to correct this as it was the case in the original data files I obtained.)

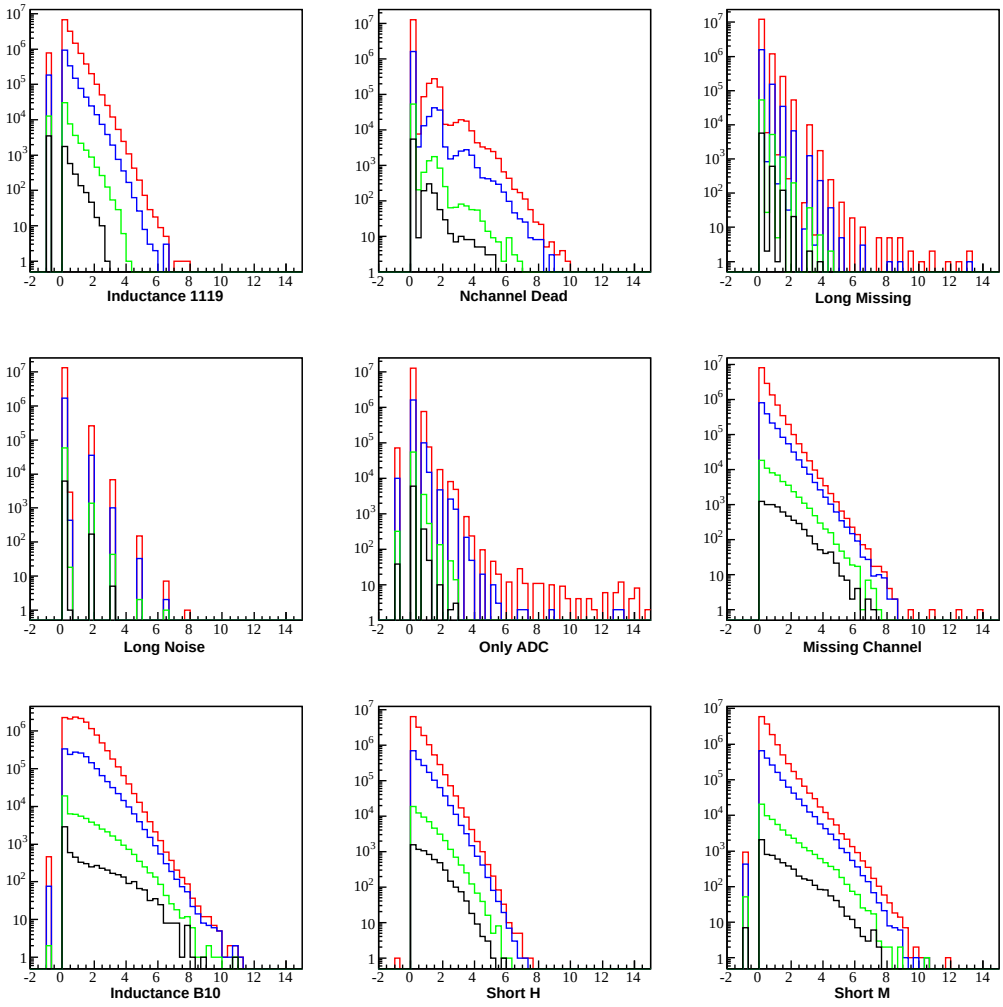

Figure 6.6: Flare checking variables for 2003 at various cut levels. In descending order these are: high energy filter, direct hits cut, loose support vector machine and tighter support vector machine. The first five variables, which show no noticeable selection effects, are used for extended flare checking cuts.

lation present in some variables). However, after unblinding the analysis was re-run without flare checking cuts as an *a posteriori* check. The results were not substantially different compared to the original unblinding results, ensuring that no observation was missed as a result of flare checking and also demonstrating that non-particle events did not create a large enough disruption in the distribution of events in this case to upset the distribution of coincidences predicted by Poissonian statistics.

6.4 Reconstructions

6.4.1 First Guess Fits

Although more accurate reconstruction methods exist, first guess fit methods are much quicker than more sophisticated methods of reconstruction and can be of significant use when used as an initial seed in more sophisticated algorithms (as is done in this analysis) or when used as an initial filter in data reduction.

The first guess cascade fit is also called the center of gravity fit. It assumes the cascade is spherical in shape and takes the weighted average of the ADCs of all hit optical modules to determine x, y and z vertex coordinates [22].

The first guess muon fit used in this analysis is call the direct walk fit [72] [73]. The direct walk method calculates pairs of hits consistent with a muon moving at the speed of light by comparing the distance between hit optical modules to the difference in times between the two events by the formula

$$\mathrm{D}/c - 30\mathrm{ns} < \Delta t < \mathrm{D}/c + 30\mathrm{ns} \text{ where } \mathrm{D} > 50\mathrm{m}. \tag{6.1}$$

The program then selects track candidates based on the number of correlated hits

as determined by this formula and their spread along the possible track. The actual track is selected by finding the largest cluster of quality track candidates, since the true track should produce many nearby candidate tracks while fake tracks should be isolated.

The line fit is another fast muon fit used in this analysis. It models the muon track as a line with velocity $\vec{v}$ and minimizes the function:

$$\sum_{\text{hits}} ADC(\vec{r}_{\text{hit}} - \vec{r}_0 - \vec{v} \cdot t_{\text{hit}})^2 \tag{6.2}$$

with respect to $\vec{v}$ and the track vertex $\vec{r}_0$.

6.4.2 Iterative Likelihood Reconstructions

The primary fits used in this analysis were Pandel track-like and point-like fits for muon and cascade events, respectively. The likelihood for a given hypothesis is defined as:

$$\mathcal{L} = \sum_{i=0}^{\text{hits}} p(t^i_{\text{res}}, d_i) \tag{6.3}$$

where $\text{p}(t^i_{\text{res}},d_i)$ is the probability of a photon arriving at a distance d from the center of the coordinate system at time t_{res}, measured with respect to the ideal Cherenkov cone. In the case of the cascade fit, the coordinate system is fixed at the center of the cascade, while for the muon fit the center of the coordinate system is attached to the muon, moving along the muon track at the speed of light [22]. Likelihood reconstructions attempt to find the most likely fit for an event, which for mathematical convenience actually involves minimizing the function $-\log(\mathcal{L})$ [2]. Mathematically, the function used in the Pandel reconstruction (originally developed for the Baikal detector) is [74]:

$$p(t^i_{\rm res}, d_i) = \frac{\tau^{\frac{d}{\lambda}} t^{\frac{d}{\lambda}-1} \exp -(t + c_{\rm ice}\frac{t}{X_0} + \frac{d}{X_0})}{\Gamma(\frac{d}{\lambda})} \tag{6.4}$$

with X_0 corresponding to the absorption length, λ the scattering length and τ the scattering time. This procedure is patched with a Gaussian function which accounts for PMT jitter. These fits are able to make multiple attempts at minimizing the log likelihood function. The first attempt starts with a first guess seeded by a previous fit and subsequent attempts minimize the function starting from a random first guess. This procedure helps avoid getting stuck in a local minimum rather than the true minimum in likelihood space. In this analysis, the iterative muon fit is seeded with the direct walk fit and the iterative cascade fit is seeded with the cascade first guess. Maximum likelihood reconstructions in AMANDA are described in more detail in [75].

6.4.3 Reproducibility issues

For events without clear tracks, particularly cascades and very high energy events, the Pandel muon reconstruction may produce wildly different results depending on what random seed is used, since there is no clear minimum for the likelihood maximization procedure to find. This is not really a failure of the fit method, since for these events there really is no "track-like" hypothesis that fits the data. However, since we don't know *a priori* which events are track like and which are best described by cascades, the cuts in this analysis use both hypotheses on all events, often comparing one against the other.

Given a reasonably large ensemble of events, the distributions of our observables are not affected by the random number seed chosen, since the event-by-event random fluctuations will cancel each other out. However, on an individual event-by-event

basis, whether or not an event survives all cuts and is kept as signal can in some cases depend on which random number seed is chosen. It is of course well known that some percentage of the real signal will be removed by our cuts in order to reduce the background to an acceptable level, so the only philosophical and logistical problem this presents is that scientific experiments depend, by basic principle, on reproducibility. For this reason, the reconstruction program *recoos* [76] was adapted to conduct the Pandel muon reconstruction using a known user-defined seed rather than one drawn from the process identification number, as is normally done. This ensured that if any reprocessing was necessary, the same events would be kept as signal.

6.5 Deadtime

In addition to the time when the detector is physically off (i.e. during maintenance), AMANDA also experiences deadtime between events. During this time, the detector cannot record new data because the electronics are being read out. The deadtime is typically on the order of a few milliseconds between each event, but longer for higher energy events (see Figure 6.7.) The deadtime percentage removes a fraction of the potential events from *each* burst, in contrast to the time the detector is actually off or not taking reliable data, which reduces the total *number* of bursts in our sample. Thus, this analysis distinguishes between *ontime*, the net period of time the detector is taking stable data, and *livetime*, the total time during which events actually register. Generally, $livetime = ontime \times (1 - deadtime)$. The livetimes for the datasets used in this analysis were 183.4 days for 2001, 193.8 days for 2002 and 185.2 days for 2003, for total livetime 562.4 days. Deadtime percentages were 21.3% for 2001, 15.0% for 2002 and 15.3% for 2003.

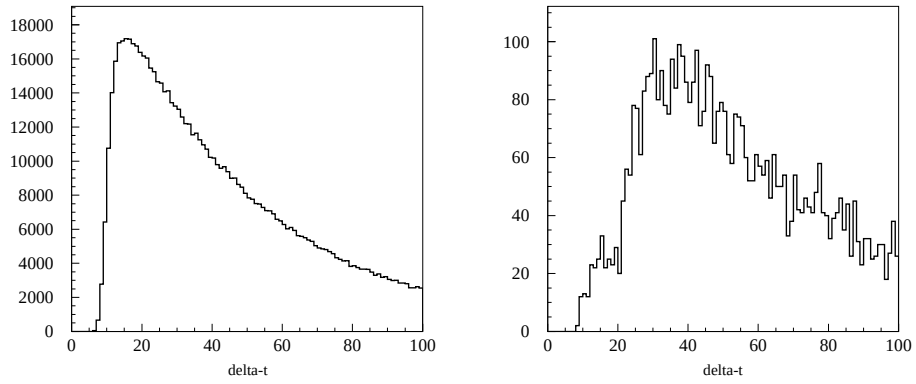

Figure 6.7: Δt between events at trigger level, in milliseconds. The plot on the left uses no cut. The distribution is Poissonian, except for the reset time of $\sim$10 milliseconds, the effects of which are clearly visible on the left side of the plot. The plot on the right shows only energetic events with high N_{channel}. These events show a considerably longer average reset time.

6.6 Monte Carlo Simulation

Cascade signal events were simulated with the ANIS software package [77]. 600 thousand events of each of the three neutrino flavors were generated. ANIS uses a default E^{-1} power law spectrum so that an equal number of events are generated in each decade of log(Energy). The spectrum was then re-weighted to match the shapes of the various neutrino flux predictions. Signal Monte Carlo was also generated using the Tea package [78], which was found to be in good agreement with ANIS, as should be the case since they use the same underlying physical assumptions. Tea was only used to test the Waxman-Bahcall model, since it was directly generated as a Waxman-Bahcall type broken power law spectrum.

Background Monte Carlo was generated using CORSIKA[3] [79]. The background

Monte Carlo was not used in determining cuts, rather actual data was used since any signal is well buried by background. However, the background simulation is still important since comparing it to real data allows us to verify that the software is modeling a given observable correctly, giving us more confidence in the accuracy of the signal Monte Carlo. Approximately 1 million events were generated in order to have an adequate sampling of high-energy events to compare to real data.

After being generated, all Monte Carlo was run through the program MMC (Muon Monte Carlo)[80], which simulates the propagation of track-like particles (primarily muons) in the ice. Since the signal for which we are looking is a cascade rather than a track, MMC makes a very small difference for the signal Monte Carlo, but is nevertheless used to simulate the signal more accurately. The Monte Carlo is then run through AMASIM [81], which simulates the response of the AMANDA detector using appropriate calibrations for each year.

[3]CORSIKA is the leading air shower simulation package, used for various experiments worldwide. Here, it used to generate the muon flux at the surface of the Earth (ice).

Chapter 7

Data Reduction

Using the procedures outlined in the previous chapter, we have obtained a high quality sample that is relatively free of distortion from noise hits, afterpulsing, cross-talk and so forth. However, at this point we have roughly 5 million remaining events per day, and locating even a fairly sizable signal in this large amount of background without further cuts would be hopeless. This chapter describes the steps by which we make cuts to remove as much of this background as possible while eliminating a minimal amount of our predicted high energy cascade signal.

7.1 High Energy Filter

Since we are looking for events that are at considerably higher energy than most of the downgoing muonic background, the first step in data reduction is applying a high energy filter. This employs two cuts. First, the total number of hits in all OMs in an event must be greater than 160. Second, at least 72% of the OMs used must have two or more hits in them. This filter cuts background to $\sim$1% of its previous level (from around 5 million to 50 thousand events per day) while retaining about

two-thirds of the signal events.

7.2 Cut on Number of Direct Hits

Step 2 involves cutting on the number of direct hits, $N_{\rm dir}$. The time of a hit is compared to the expected arrival time of a photon traveling directly from the appropriate point along the reconstructed muon track or cascade. If the fit hypothesis is correct, those photons that are delayed very little by scattering in ice will arrive close to the predicted time and are counted as a direct hit. Several time window choices are available for determining what constitutes a "direct" hit. The widest possible time window was used in this analysis, 15 nanoseconds before and 150 nanoseconds after the predicted time. This provided the clearest separation between signal and background.

There is too much disagreement between the simulated background and the real data in $N_{\rm dir}$ to fully trust the signal simulation. This problem is far from unique to this analysis. $N_{\rm dir}$, since it relates directly to photon scattering, is more affected than most variables by simplifications and inaccuracies in the modeling of the ice properties. Rather than include it in the final cut stage, which requires low systematic uncertainties in the actual shape of the signal spectrum, we instead use it as a loose cut to get the number of events down to a more reasonable level. In addition to saving processing time, applying this cut improves the overall separation between signal and background once all cuts have been applied.

$N_{\rm dir}^{\rm muon}$ (the number of direct hits for the muon fit) is a useful cut because one gets fewer direct hits with an incorrect hypothesis than a correct one, meaning cascades will generally be clumped at small values of $N_{\rm dir}^{\rm muon}$. A significant tail in the cascade

signal simulation is caused by particularly energetic events with a large number of total hits, since these events can have a considerable number of events which register as "direct" according to the track hypothesis simply by random chance. One can therefore eliminate this tail by dividing number of direct hits by total number of hits (see figure 7.1). This was the cut used in the original 2001 analysis.

A further improvement was made for the years 2002 and 2003. The signal spectrum is kept in a tighter peak if one takes $N_{\mathrm{dir}}^{\mathrm{muon}} - N_{\mathrm{dir}}^{\mathrm{cascade}}$ than if one just takes $N_{\mathrm{dir}}^{\mathrm{muon}}$ (see figure 7.1). While a cascade event may occasionally happen to wind up with a non-negligible number of direct hits based on an (incorrect) track fit, this incorrect fit will very rarely result in a significantly greater number of direct hits than would be obtained by a correct cascade hypothesis. It was decided not to make this adjustment for the 2001 dataset because it had previously been unblinded with the original cut, and incurring the additional trials penalty would not be justified.

7.3 Support Vector Machine Cut

The final step in data reduction is a cut using a six-variable support vector machine (SVM). Support vector machines are programs which find the optimal multi-dimensional cut to separate two different classes of data (referred to here as "signal" and "background") using input variables. They are related in concept to neural networks, and in some cases, the definitions of the two overlap. Previous uses of SVMs have included face detection in images, text categorization and charm quark detection [82]. The program used to train the support vector machine used in this analysis was SVM$^{\mathrm{light}}$ [83].

The support vector machine learns to classify data by being fed a series of back-

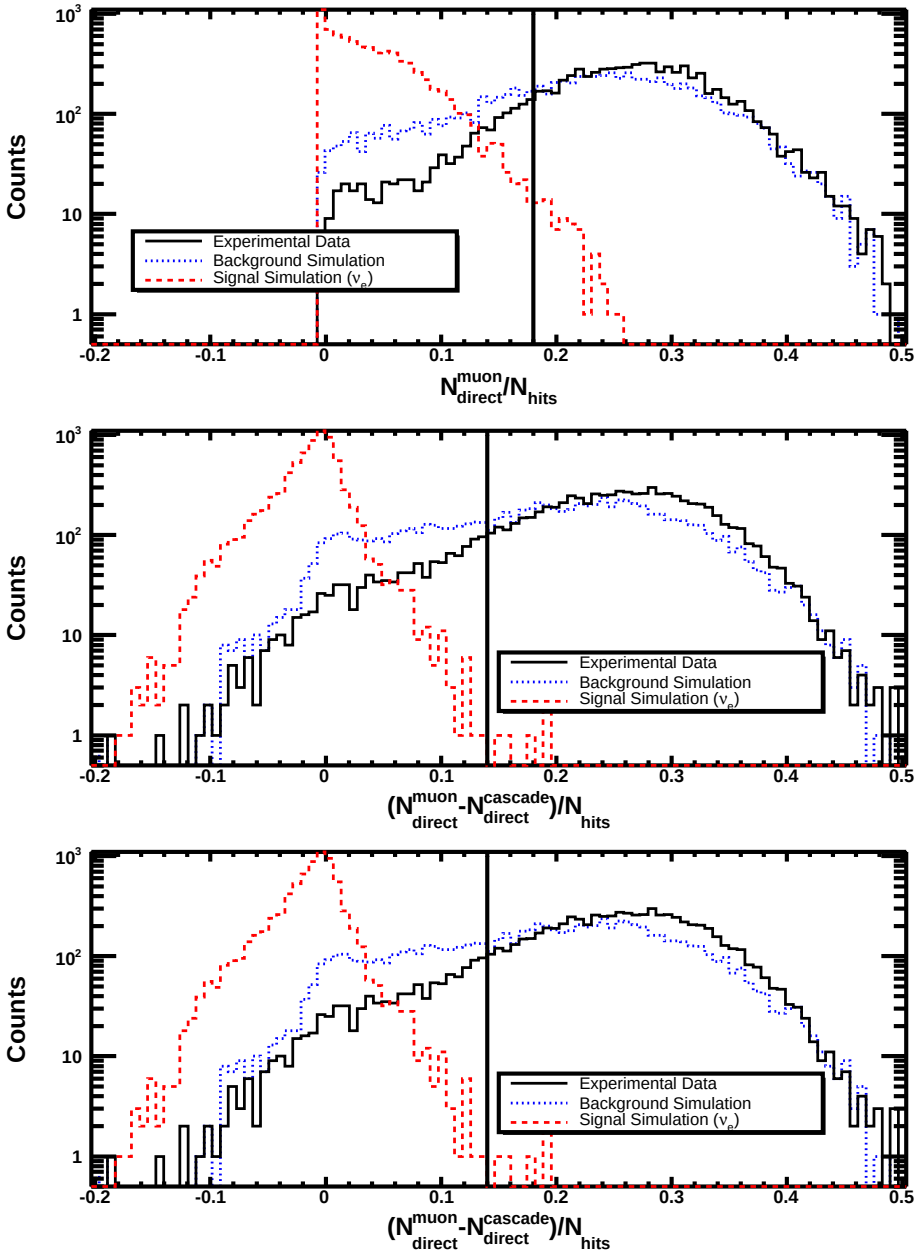

Figure 7.1: Number of direct hits cut for 2001, 2002, 2003.

ground and signal events. Signal events are taken from cascade Monte Carlo while background events are taken from the real data sample. It is assumed that any signal buried within the real data will be overshadowed by thousands of legitimate background events, therefore real data does a better job of characterizing the real background than monte carlo simulation.

Five runs ($\sim$1 day each) from each year are used as background events for training. These 5 training runs were left out of the final analysis, since AMANDA's blindness standards require that all selection criteria applied to an analysis be finalized before the experimental data is actually examined. Properly conducting a blind analysis allows the experimenter to avoid unconsciously choosing the cuts in such a way that the statistical significance of an observation is artificially increased or decreased. (See [84] for a brief discussion of blindness as applied to particle physics experiments.)

When training the SVM, each event is entered as a series of numerical values. The first value tells the program whether the sample event is signal or background. The following six values are the cut variables, re-scaled to have a value between 0 and 1. This rescaling is done to normalize the variables to each other, preventing one variable from becoming dominant simply because of the numerical scale it is plotted on. Once an SVM has been trained with several thousand background and signal events, it uses this information to classify additional data as either "signal" or "background".

When using a support vector machine, several choices must be made by the user, the first of which is the mathematical kernel. This kernel is the mathematical equation which is used to translate the multidimensional space of the variables into a higher dimensional space where the decision function can be expressed as a linear function of

the input variables [82]. For this analysis, a Gaussian radial basis function kernel with width 30 was empirically determined to be the best choice. Other choices of kernel include a simple polynomial of arbitrary degree p and a hyperbolic tangent function. Once the kernel is selected, the "cost factor", also known as the error penalty, can be varied. This is the "cost" of allowing a given event to be labeled as background, and is the variable by which the support vector machine cut can be tightened or loosened to allow more or less background (and signal) to be kept by the cut.

Optimization procedures for deciding which cost factor to take are discussed in the next chapter. A sample plot showing support vector machine output is shown in Figure 7.2 and the six variables used in the support vector machine are plotted in Figures 7.3 to 7.8. Comparisons of different neutrino flavor cascade reconstructions in the six variables are shown in Figure 7.9. These six cut variables are described as follows:

7.3.1 Cut 1: Fraction of hit modules with 8 or more hits

The first variable in the SVM is the fraction of hit optical modules which have 8 or more hits. (Eight hits per event is the most AMANDA hardware can record, so anything which would have more than 8 events is recorded as 8.) This is primarily an energy-related cut, as higher-energy events are more likely to produce a larger number of hits in the detector and tend to produce particles in bundles. However, a cascade will also produce on average a higher number of hits per module compared to a muon induced by a neutrino of comparable energy because of the multiple particles produced in the shower.

7.3.2 Cut 2: Number of hits divided by Number of channels

This cut operates on the same principle as the previous variable in that high energy events and cascades both tend to have larger numbers of events per hit channel. N_{channel} and N_{hits} are by themselves rough indicators of energy, but the combination has more power to separate cascades from muonic background than the variables individually. Support Vector Machine results are similar if one takes the two variables independently, meaning the SVM apparently finds this combination on its own as well.

7.3.3 Cut 3: Number of late hits: $N_{\text{late}}^{\text{cascade}}$ - $N_{\text{late}}^{\text{muon}}$

A late hit is defined as a hit occurring at least 150 ns after the nominal start of an event. The number of late hits works as a cut variable for the same reason as N_{dir}. It is useful in distinguishing between muons and cascades since more late hits will occur for an inappropriate hypothesis (e.g. a cascade fit when the particle is really a muon) than a correct one. Subtracting the number of late hits for the muon fit from the number of late hits for the cascade fit allows a direct comparison of the accuracy of the two fits. While this cut is correlated with the number of direct hits variable, it is a less powerful cut. However, there is considerably better agreement between the number of late hits variable in real data and simulation, allowing its inclusion in the support vector machine.

7.3.4 Cut 4: Length of direct hits: $L_{\text{dir}}^{\text{muon}}$

Length of direct hits is another topological variable. The track length is defined by projecting each of the direct hits (see direct hits discussion in section 6.2) onto the reconstructed muon track and measuring the physical distance between the first and

last events on the track. Properly fit track-like muon events will have significantly greater lengths than more spherically-shaped cascades.

7.3.5 Cut 5: Likelihood Ratio

The likelihood ratio variable used is actually defined as negative log likelihood for mathematical convenience:

$$-\ln(\frac{\mathcal{L}_{\text{cascade}}}{\mathcal{L}_{\text{muon}}}) \tag{7.1}$$

where $\mathcal{L}_{\text{muon}}$ is the likelihood of the event being a muon according to the muon fit and $\mathcal{L}_{\text{cascade}}$ is the probability of the event being a cascade according to the cascade reconstruction, as discussed in the previous chapter.

7.3.6 Cut 6: Velocity of the Line Fit

Velocity of the line fit [76] works as a topological cut because the line fit matches muon track events better than cascades. The velocity of a line fit applied to a more spherical cascade event will be slower because the events don't occur in a linear progression as the line fit assumes, but spread out in multiple directions.

7.4 Overall Signal Retention

As a summary of the data reduction process, simulated signal (weighted to a Waxman-Bahcall power law) and experimental background passing rates for the various stages of data reduction are shown in the table below (with the final cut stages optimized according to the procedure described in the next chapter).

	Exp Data	$\nu_e + \bar{\nu}_e$ signal
Initial	100%	100%
Filter	0.80%	62%
N_{dir} cuts	0.10%	62%
SVM short window search	0.0027%	58%
SVM long window search	0.00040%	43%

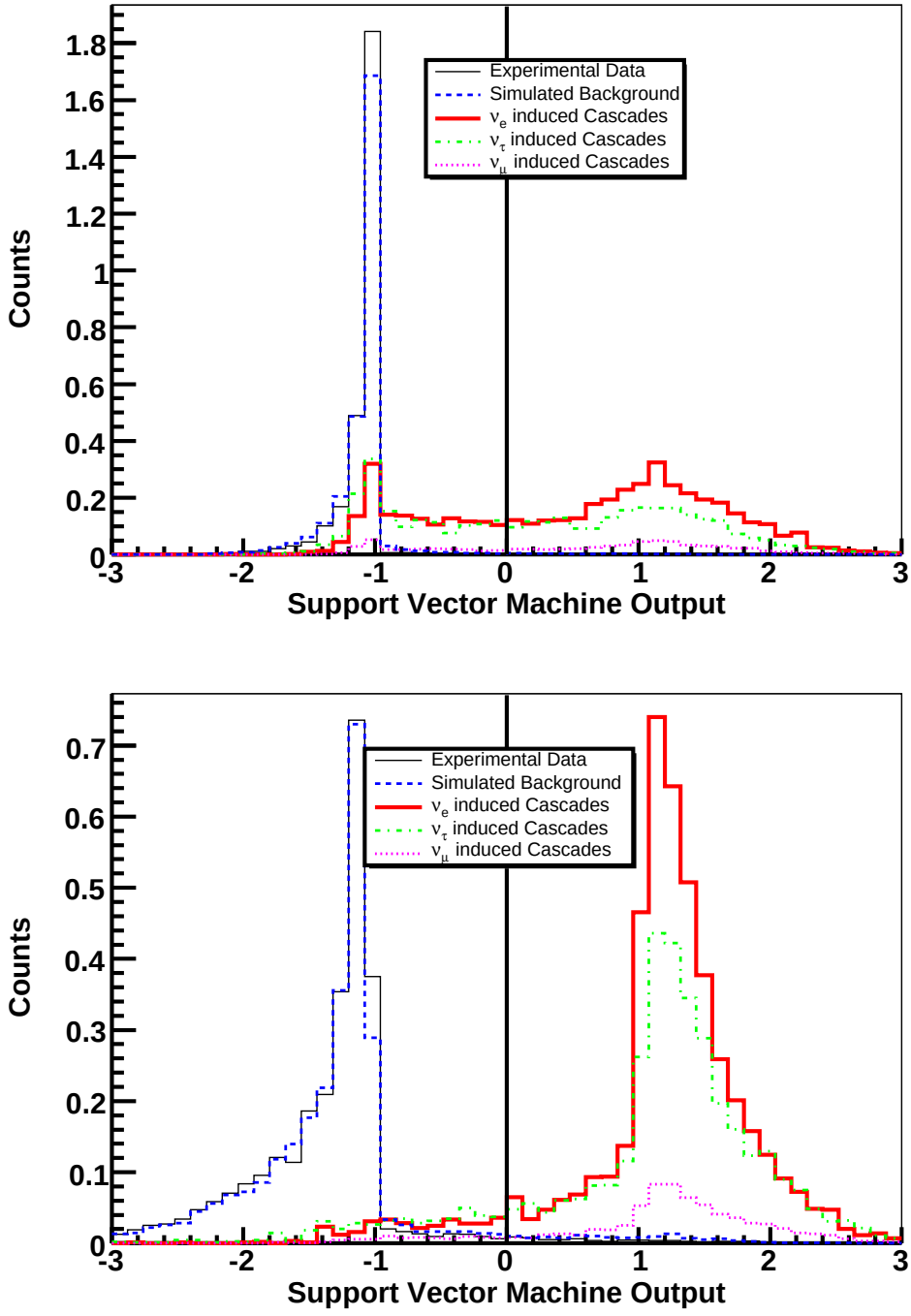

Figure 7.2: Support Vector Machine value output for long (top) and short (bottom) time window optimizations in 2002, featuring real data and ANIS simulation of each neutrino flavor. Zero is the boundary between "signal" and "background" classifications.

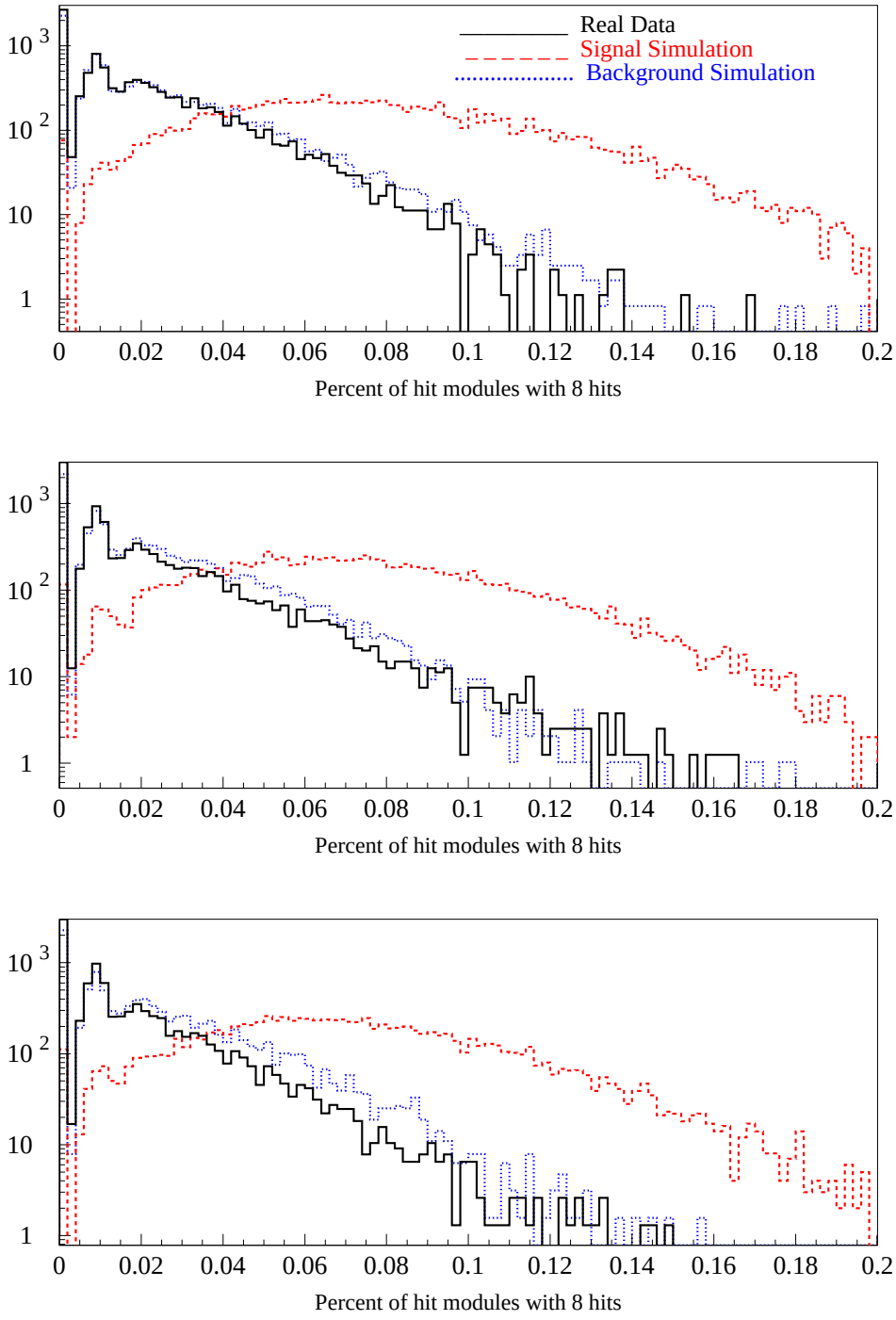

Figure 7.3: Frac 8 variables for 2001 (top), 2002 (middle), and 2003 (bottom).

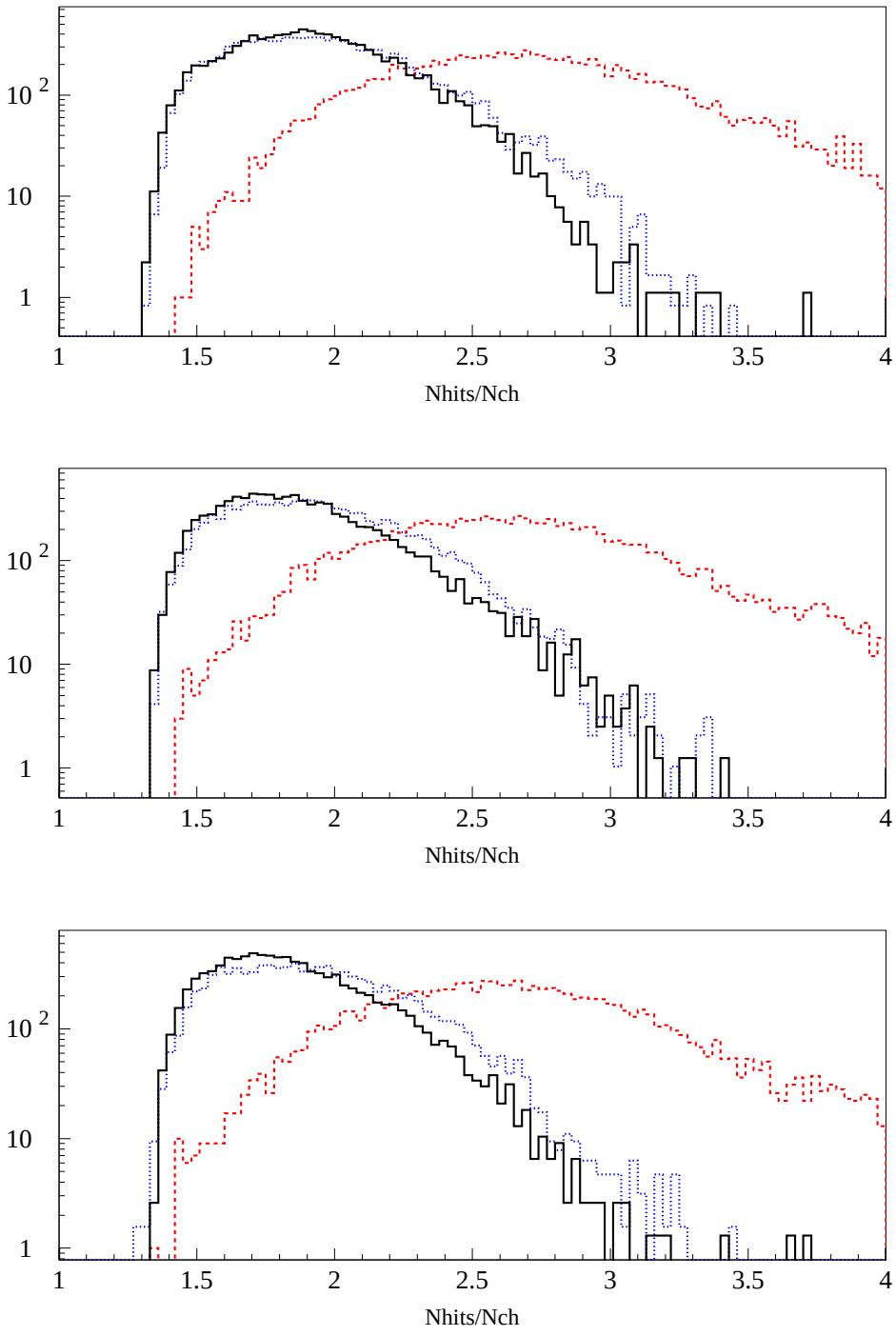

Figure 7.4: Number of Hits divided by Number of Channels for 2001 (top), 2002 (middle), and 2003 (bottom).

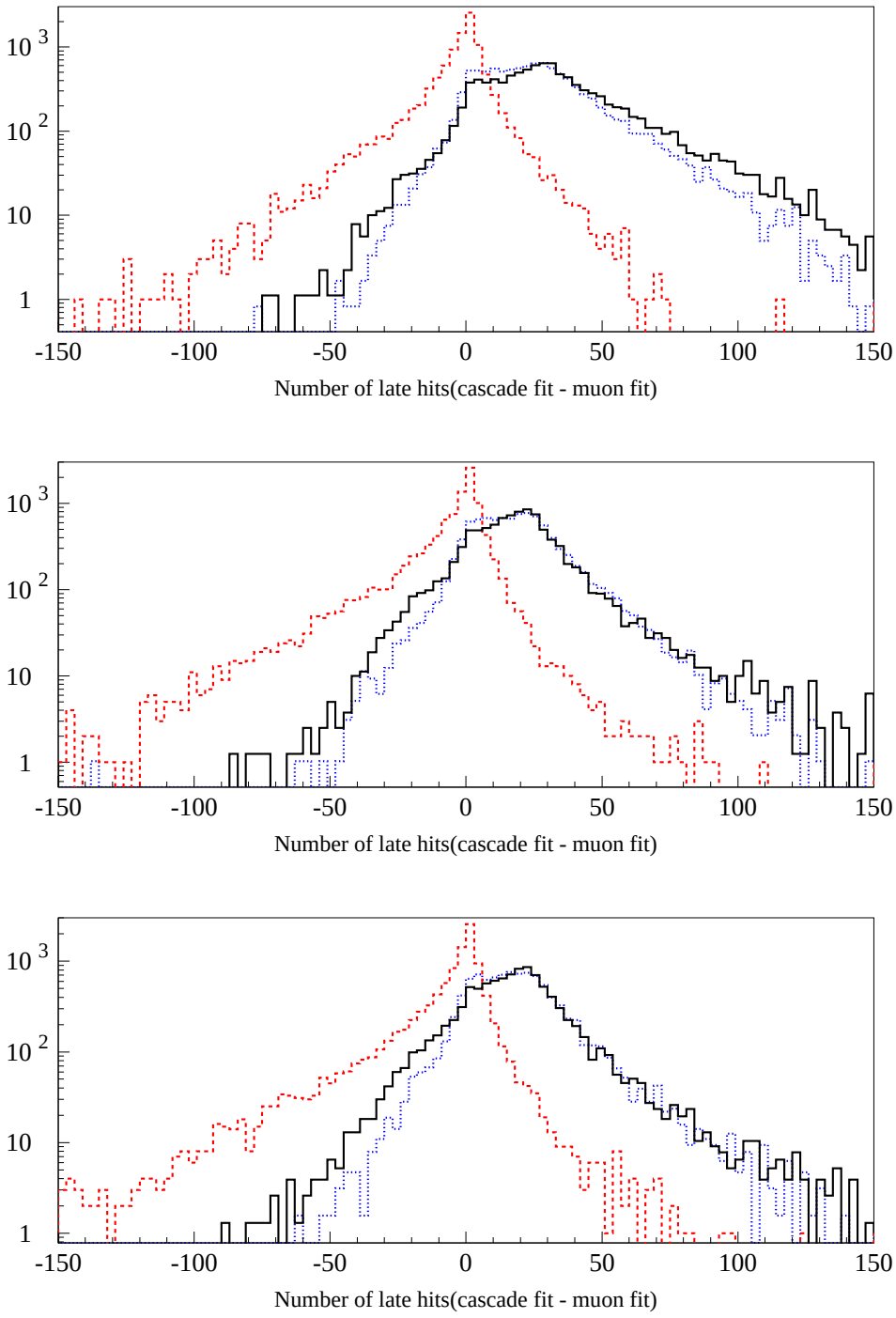

Figure 7.5: Number of Late Hits for 2001 (top), 2002 (middle), and 2003 (bottom).

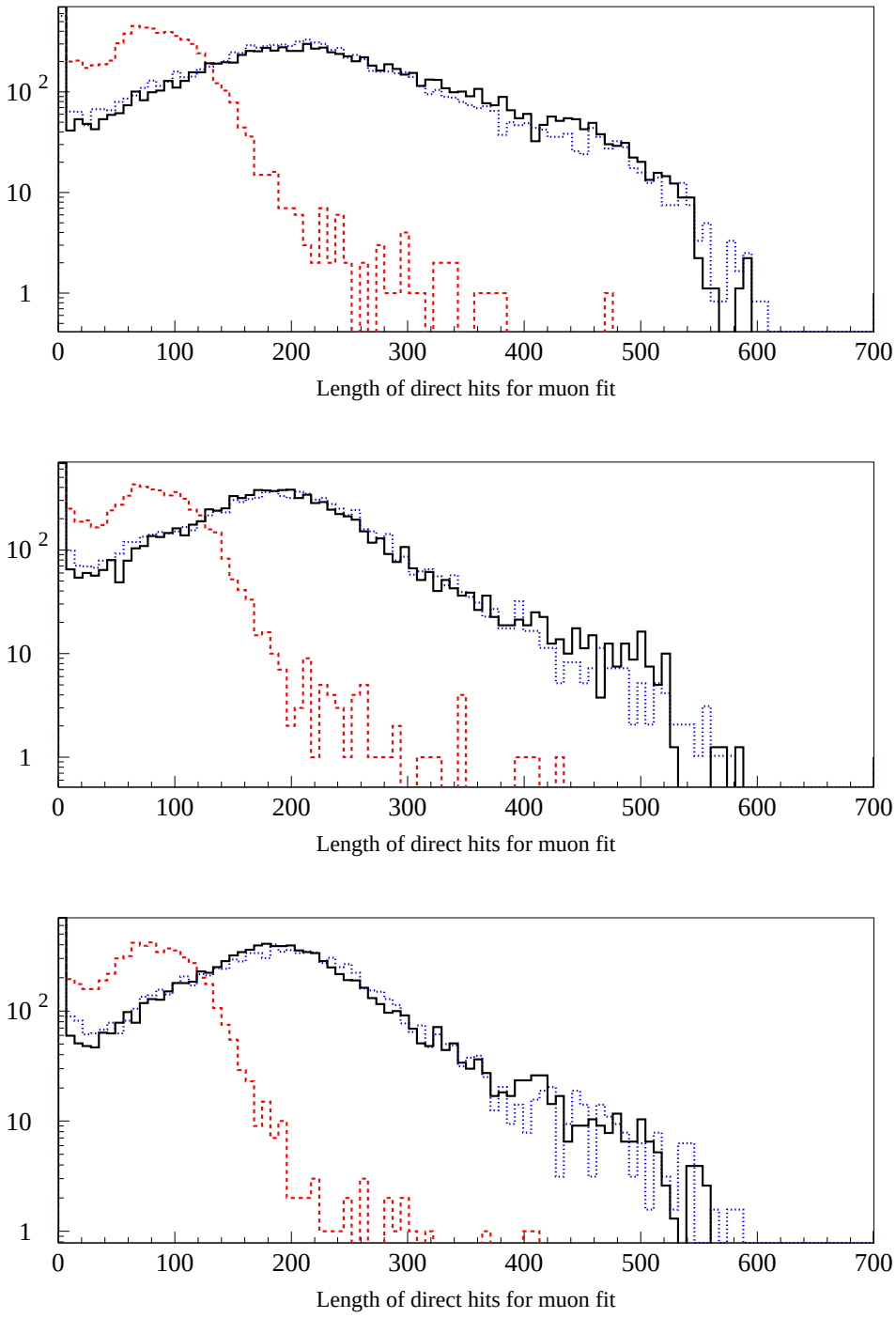

Figure 7.6: Length of Direct Hits for 2001 (top), 2002 (middle), and 2003 (bottom).

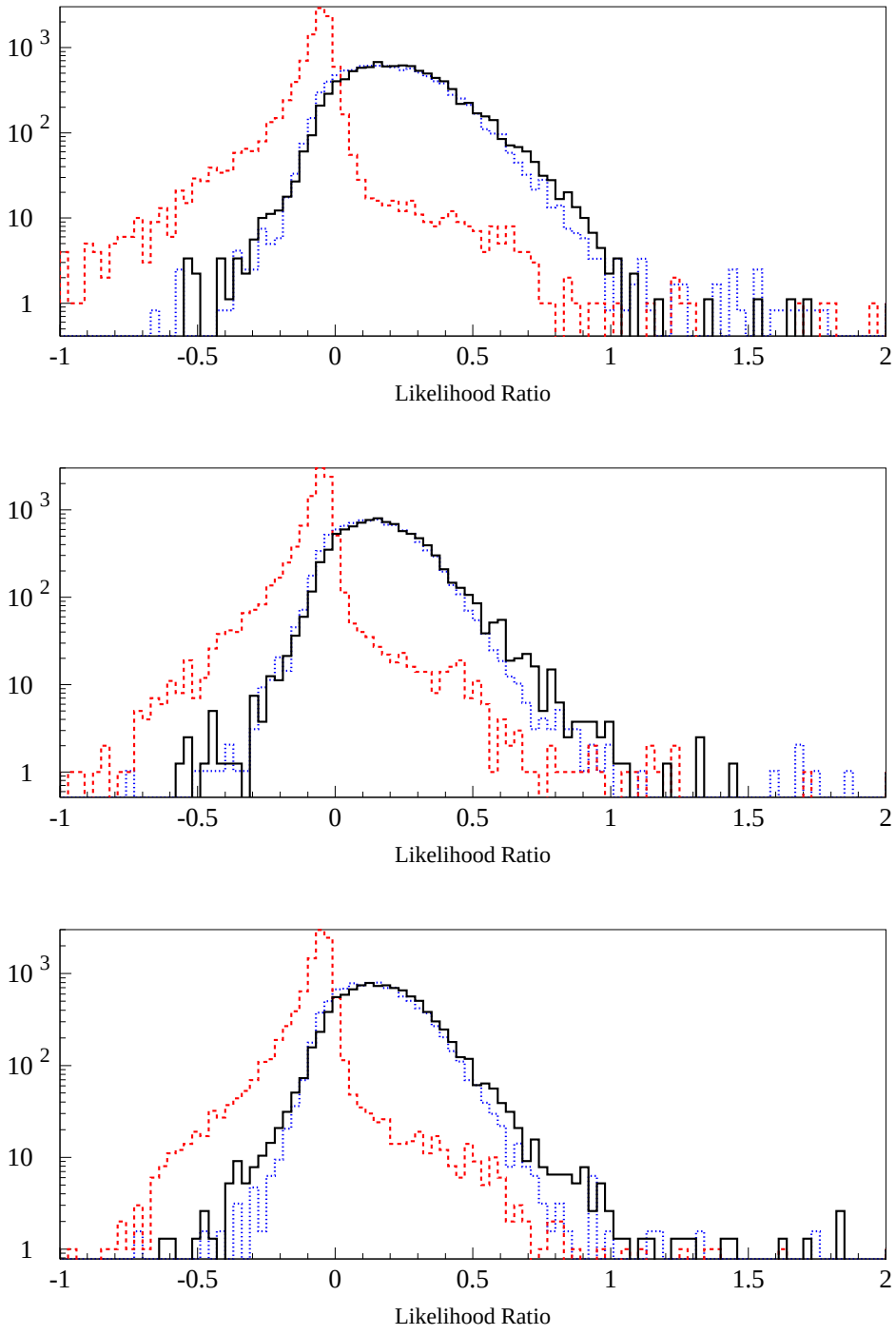

Figure 7.7: Likelihood Ratio Cascade fit to Muon fit for 2001 (top), 2002 (middle), and 2003 (bottom).

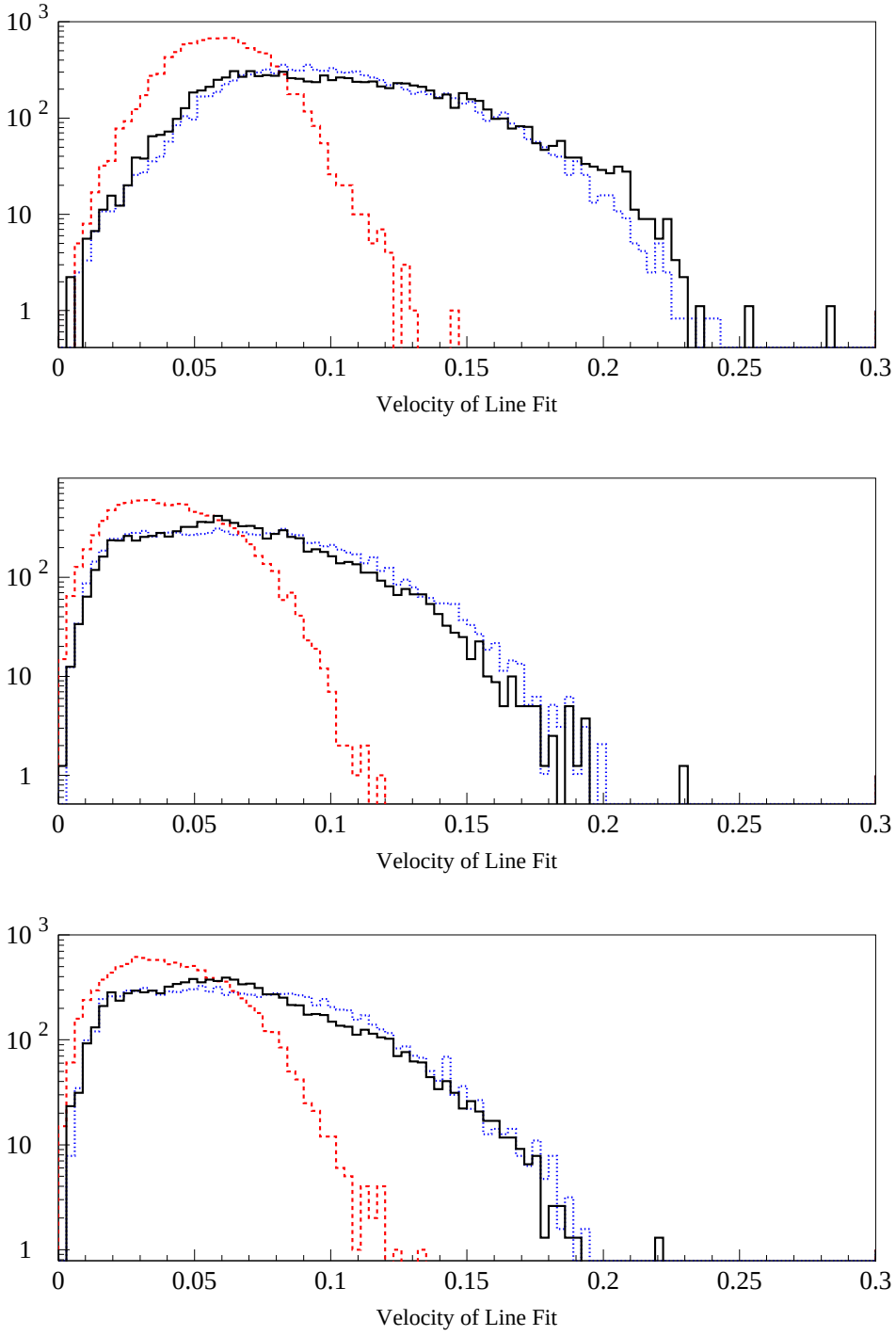

Figure 7.8: Velocity of the Line Fit for 2001 (top), 2002 (middle), and 2003 (bottom).

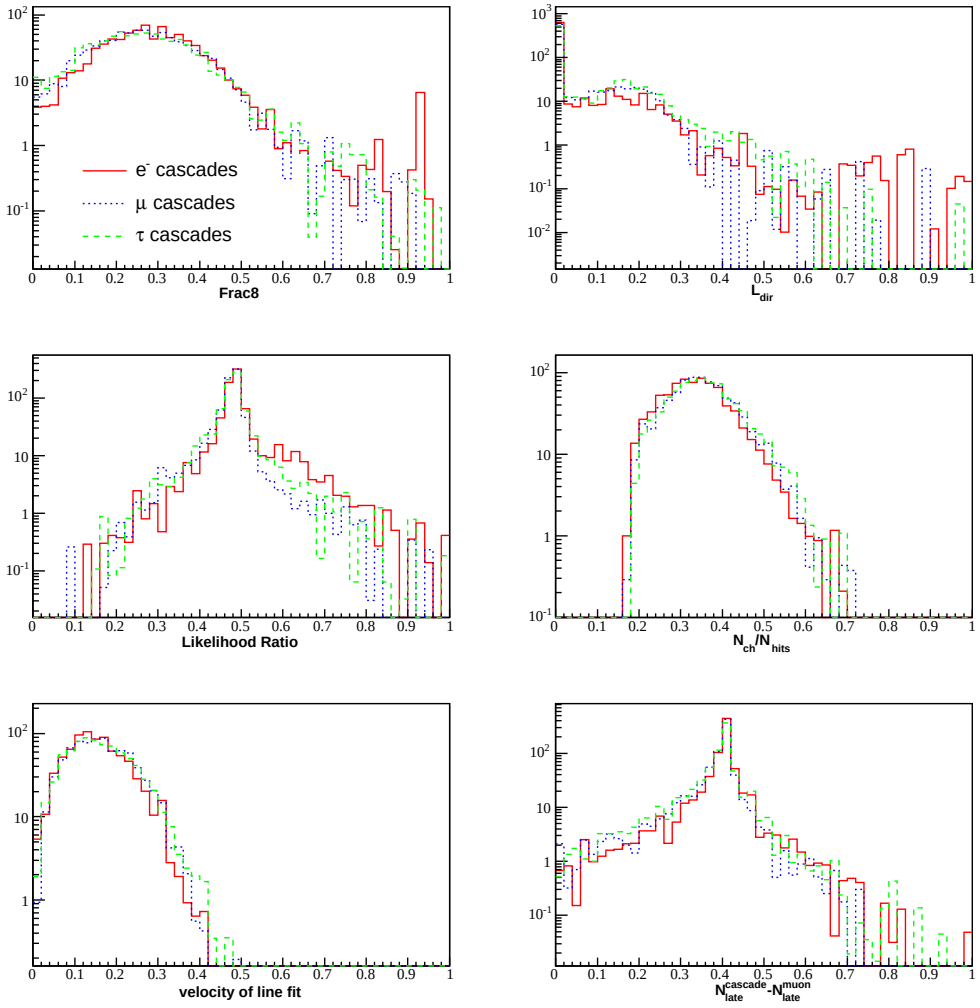

Figure 7.9: Cascade signal produced by the three flavors of neutrino for the six variables used in the Support Vector Machine cut. Total flux has been normalized to allow direct comparison. The distributions are quite similar, but non-negligible differences exist.

Chapter 8

Cut Optimization

There are two different, albeit related, methods of selecting the optimal cuts in AMANDA analyses. Section 8.1 describes how to perform a sensitivity optimization for this analysis. This method, which is designed to place the best possible neutrino flux limit in the absence of a signal, is the one used for most AMANDA analyses. Although this method was not the one selected for this analysis, it is still useful to examine the sensitivities at various cut strengths to make sure the selected cuts are not too far from the optimal sensitivity. Additionally, the procedure used to calculate upper limits, described in sections 8.1.2 and 8.1.3, is essentially the same when calculating sensitivity and when determining final limits. Section 8.2 describes the procedure ultimately used to select our final cuts, which optimizes the analysis for the best chance of making a significant discovery.

8.1 Sensitivity

8.1.1 The Model Rejection Potential Method

Sensitivity optimizations in AMANDA generally follow the Model Rejection Potential formalism [85]. This method is designed to be an unbiased means of optimizing the limit setting potential of an analysis assuming no signal will be observed. The minimum neutrino flux to which an analysis is sensitive at a 90% confidence level is found by the formula:

$$\Phi_{90} = \Phi \frac{\bar{\mu}_{90}}{N_s} \tag{8.1}$$

The same calculation can of course be done for any confidence level, but 90% is the value generally used in AMANDA analyses. Φ is a reference flux[1]. N_s is the number of signal events one expects in the detector given this reference flux. $\bar{\mu}_{90}$ is the average upper limit expected from the experimental background, obtained using a 90% confidence belt calculated under the Feldman Cousins [86] ordering system (as described in the next section). The ratio $\bar{\mu}_{90}/N_s$ is referred to as the model rejection factor (MRF), the scaling factor between the actual experimental sensitivity Φ_{90} and the reference flux Φ.

It has recently been proposed that the median upper limit should be used in place of the average upper limit. It is philosophically a more appealing choice since, unlike average upper limits, it is independent of the metric used [87]. It is even easier

[1]Sensitivities and upper limits relative to Waxman-Bahcall spectra are traditionally expressed in terms of a diffuse flux which is the summation of the total output of each discrete GRB source spread out through the entire year and 4π sr solid angle. The limits are given in units of GeV cm^{-2} s^{-1} sr^{-1}, which actually refers to the normalization of the E^{-2} portion of the spectrum, between the two break energies, which appears flat on an $E^2\Phi$ plot.

to calculate, since it is just the upper limit given the median result (the center of the distribution if it is symmetric). However, since pathological effects were observed in other analyses which attempted to use the median upper limit method [88], the analysis described in this thesis uses average upper limits. Median and average upper limits should not generally result in drastically different results and, since this particular analysis optimizes for discovery, this choice does not directly impact the results of the rolling search.

8.1.2 Determining Upper Limits in This Analysis

The average upper limit is calculated by:

$$\bar{\mu}_{90}(n_b) = \sum_{n_{\rm obs}=0}^{\infty} \mu_{90}(n_{\rm obs}, n_b) \frac{(n_b)^{n_{\rm obs}}}{n_{\rm obs}!} \exp(-n_b) \tag{8.2}$$

which is just saying that one determines the average upper limit by taking the upper limit resulting from each possible outcome of the experiment (generally, the number of events actually observed) and multiplying this by the Poissonian likelihood of that outcome occurring.

For most analyses, which simply use the number of events remaining after cuts as the observable, the upper limits are available from lookup tables. For this analysis, which relies on temporally-correlated clusters of events in order to evaluate significance, the procedure is more complicated. However, it still uses the exact method laid out in [86].

The observable in this analysis is $N_{\rm large}$, the largest observed clustering of events for a given time window occurring at any point in the data sample. This observable was chosen under the assumption that any signal observed would most likely originate from

a unique event with much larger than average flux, rather than part of an ensemble of similar transients.

A Monte Carlo simulation was developed in order to calculate sensitivity. The program was run for a wide range of cut strengths (support vector machine cost factors) and over a wide range of overall signal fluxes. To generate good statistics, an ensemble of 50 000 monte carlo "experiments" was run for each combination of cut strength and signal flux. For each of these "experiments", the number of events observed in the detector for each of the 1238 bursts[2] assumed to be in our livetime is calculated. The signal strength (expected number of neutrino events in the detector) for each burst is calculated by the formula:

$$s = g \times d \times p \times n \tag{8.3}$$

where g is a model-dependent scaling factor described in detail in section 7.3.3, d is the deadtime correction, and p is the percentage of events retained by the support vector machine cut. The average number of events per burst n is incremented in the monte carlo from 0 to 0.5 events per burst in steps of 0.001 events. The value of n increases linearly with flux, so the scaling factor between n and the overall neutrino flux can be calculated using ANIS signal simulation, accounting for all detector effects and cuts up to the final support vector machine cut. Since both p and d are slightly different for different years, 425 of the 1238 bursts simulated use 2001 information, 413 use 2002 information and 400 use 2003 information, scaled with the ontime of the data used for each year.

[2]Arrived at by adjusting the rate of GRB observations by BATSE for field of view and livetime of the analysis.

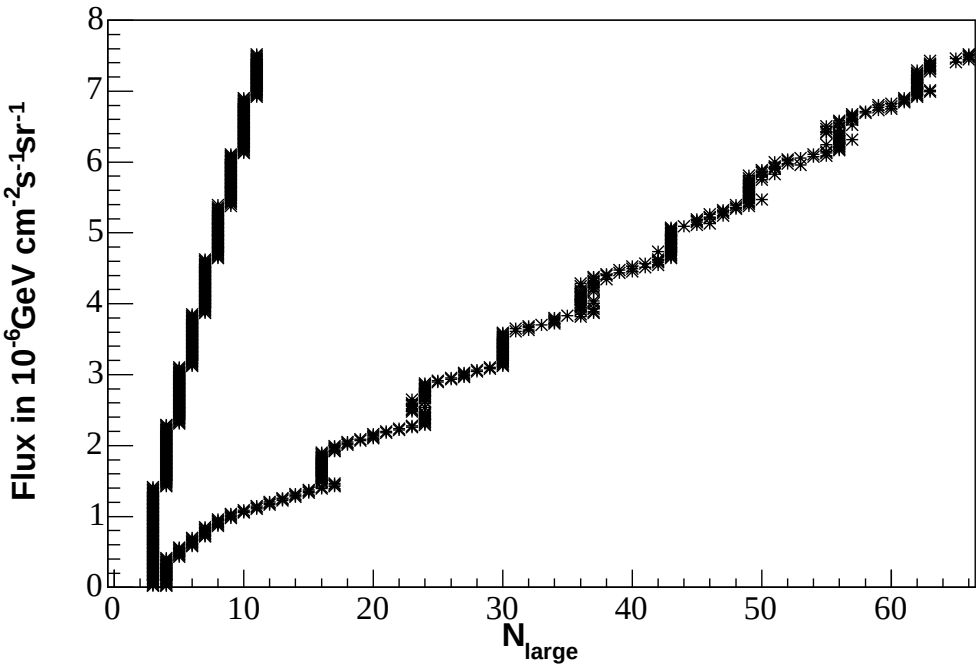

Figure 8.1: 90% confidence level belts for 3-year analysis assuming Waxman-Bahcall spectrum. The y-axis has been re-scaled from average number of signal events per burst to diffuse signal flux (the two are directly proportional).

Using the signal strength s as the average expected number of events for a burst, the number of events actually observed is randomly chosen using Poisson statistics. The program then adds in the possibility of background contamination, then looks through all 1238 bursts to select N_{large} for that experiment. For low signal strengths, it is possible that N_{large} could result solely from background events without any signal, so the simulation includes this possibility in the model. The N_{large} values for all 50 000 trials at a given cut strength and signal flux are recorded.

90% confidence level belts are constructed by applying the Feldman Cousins likelihood ratio ordering method to this data. For each possible value of N_{large}, the

sorting algorithm scans through all the signal fluxes and finds the maximum likelihood, $\mathcal{L}_{\max}$, which is the highest probability of obtaining that value of N_{large} given any signal flux.

After maximum likelihoods are obtained for all N_{large}, confidence belts are assembled for each signal strength. For a given belt, the first value of N_{large} to be included is the value which has the highest likelihood ratio. This is defined as $\mathcal{L}_s/\mathcal{L}_{max}$, where $\mathcal{L}_s$ is the probability of observing that value of N_{large} at *this* signal strength and $\mathcal{L}_{max}$ is the maximum likelihood at *any* signal strength. The second highest likelihood ratio is selected after the highest, and so on until the included values account for at least 90% of the total probability. This range then constitutes a 90% confidence level belt. Since the confidence belt is assembled from discrete rather than continuous quantities, the total percentage included in the confidence belt is in practice generally greater than the nominal 90% value. For example, in Figure 8.1, at a signal flux of $\mathrm{E}^2\Phi = 0.7\times10^{-6}$ GeV cm^{-2} s^{-1} sr^{-1}, the relevant values are as follows:

N_{large}	likelihood ratio $\frac{\mathcal{L}_s}{\mathcal{L}_{max}}$	likelihood $\mathcal{L}_s$
3	0.427	0.322
4	0.907	0.341
5	0.646	0.142
6	0.452	0.079
7	0.300	0.044
8	0.072	0.027

Thus, one would include these in the confidence belt by descending likelihood ratio in the order N_{large} =4,5,6,3,7,8. Adding the likelihoods of getting N_{large}=3, 4, 5 or 6 one obtains 0.322+0.341+0.142+0.079=0.884. This is not yet at the required value of 0.9, so we add 7 to the confidence belt, giving us a total probability of 0.884+0.044

= 0.928. This is greater than a 90% probability, so our confidence belt at this signal strength goes from $N_{\text{large}} = 3$ to $N_{\text{large}} = 7$, inclusive.

Once confidence belts have been constructed for the relevant range of signal fluxes, the upper limit for a given value of N_{large} can be read off the plot as the first flux which is not contained within a confidence belt. At N_{large}=3 events, for example, the upper limit from Figure 8.1 is around 1.4×10^{-6} GeV cm^{-2} s^{-1} sr^{-1}. A disadvantage of employing the likelihood ratio ordering method is that for large values of N_{large}, the maximum likelihood occurs at very high signal strengths, so one is obligated to run simulation over a much wider range of signal fluxes than is otherwise directly relevant to limit setting.

The determination of sensitivity before the experiment is unblinded and the final experimental limit afterwards are nearly identical processes, except that the weighted average of possible values of N_{large} are used for sensitivity and the single experimentally observed value is used for the final limit.

8.1.3 Inclusion of Systematic Uncertainties

Systematic uncertainties are evaluated in the manner laid out in [89] and [90]. Rather than take the signal efficiency ϵ_s as a single known value, the numerator in the likelihood ratio is integrated over the entire probability distribution function of possible signal efficiencies. In the case of this analysis, the PDF used was a flat rather than gaussian distribution. Integrating the maximum likelihood (denominator of the likelihood ratio) over the full range of possible signal strengths has been observed in some cases result in pathological effects. For example, the resulting limits can actually improve as uncertainties increase in cases where this is clearly not a logical result. As

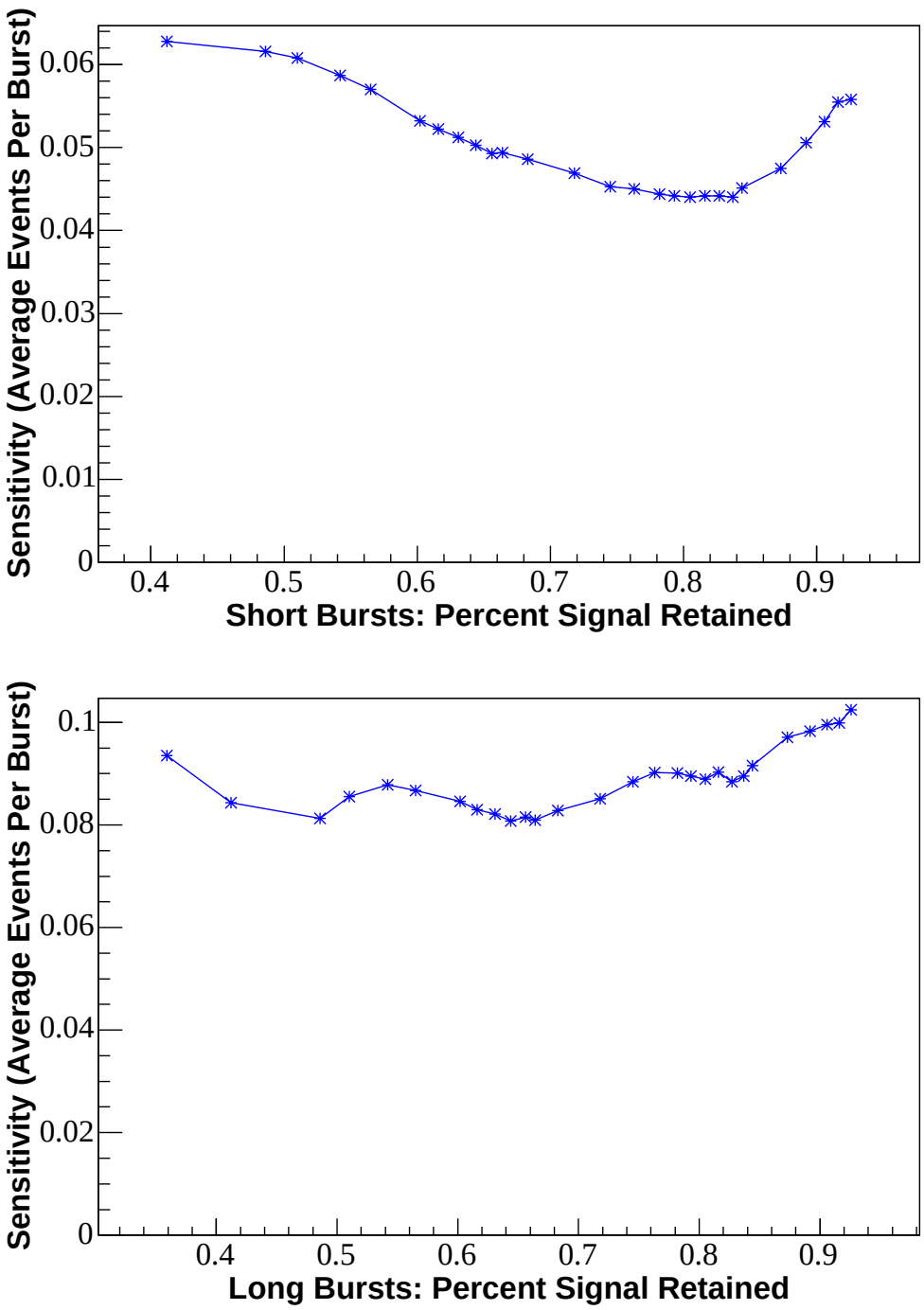

Figure 8.2: Sensitivity as a function of signal retention for long and short duration searches.

recommended in [91], the denominator therefore uses the original best guess ϵ_s rather than integrating over a range. The full equation for the systematics-adjusted likelihood ratio is thus:

$$R = \frac{\int_{\epsilon'_s} \mathcal{L}(n|\mu_s, \mu_b, \epsilon'_s) P(\epsilon'_s|\epsilon_s, \sigma_{\epsilon_s}) d\epsilon'_s}{\mathcal{L}(n|\mu_s, \mu_b, \epsilon'_s)} \tag{8.4}$$

In practice, this integration is carried out numerically rather than analytically by sampling at random from the possible range of signal efficiencies for each trial in the Monte Carlo simulation used to determine sensitivity.

8.2 The Model Discovery Potential Method

Since our limits are considerably above the predicted neutrino flux and the sensitivity is not strongly dependent on cuts, it was decided to optimize for the best chance of discovery, using the procedure discussed in [87]. Optimizing for discovery in this analysis means selecting the cut at which one has a 90% chance of seeing a cluster of at least 5σ significance at the minimum possible neutrino flux. 5σ was selected because it is the standard threshold for discovery in the astrophysics community. The choice of 90% probability[3] is more arbitrary, but a reasonable choice to have a solid likelihood of seeing a signal without making excessive demands. In practice, it is just necessary to choose a value for calculation purposes and the optimization does not depend strongly on the chosen value, as long as the probability chosen is above 50% or so (see Fig. 8.3).

The number of events which is sufficient for a 5σ discovery is a discrete quantity

[3]The specific probability chosen is referred to as the *statistical power* in this context.

which must be evaluated at each possible cut strength. Because the statistical significance of a cluster of n events is determined by how likely it is to be a "false" detection, the number of events needed for a discovery at each cut level is determined entirely based on the background rate. The signal flux at which one has a 90% probability of detecting at least this many events for that cut is determined with monte carlo simulation similar to that used when determining sensitivity.

For the rolling search, each measured event starts a new 1 or 100 second time window. When determining the number of events required for statistical significance, we assume a background that is reasonably stable over large timescales and can be adequately modeled with Poissonian statistics (see Appendices B and C for plots supporting these assertions). Thus, each time window is expected to contain the event that starts the window, plus an additional number of events determined by Poissonian statistics.

When determining the odds of getting an upward fluctuation by chance, it is mathematically much more convenient to calculate the odds of *not* getting an upward fluctuation of at least n events rather than of getting such a fluctuation. Not only does this avoid calculating what is technically an infinite series of probabilities, but it also makes it easier to combine calculations for multiple time windows.

The probability of getting n or more events in a window is of course equal to the probability of getting fewer than n events subtracted from 1 (because either you get at least n events or you don't). Likewise, the probability of getting n or more events in *at least* one of two windows is the same as the Poissonian probability of getting fewer than n events in both windows subtracted from 1, expressed formally in this case as:

$$p(\geq n) = 1 - \sum_{i_1=0}^{n-2} \frac{\lambda_1^{i_1}}{i_1!} \exp(-\lambda_1) \sum_{i_2=0}^{n-2} \frac{\lambda_2^{i_2}}{i_2!} \exp(-\lambda_2) \tag{8.5}$$

where λ_1 and λ_2 are the event number expectation values in the two time windows. Note that here we are counting the single event which starts each time window of the rolling search towards our total of n events in the above equation, which then calculates the probability of getting at least $n-1$ *additional* events. This is true of the remaining equations in this section as well. Easily generalizing to an ensemble of m time windows, one for every event, the probability of getting n or more events in any window is therefore:

$$p = 1 - \prod_{j=1} \sum_{i_j=0}^{n-2} \frac{\lambda_j^{i_j}}{i_j!} \exp(-\lambda_j). \tag{8.6}$$

The event rate λ_j is not quite identical for each window because the background rates vary non-negligibly over the year. See [103] for a discussion of seasonal variation in the atmospheric muon rate. If a different λ is selected for periods which are too short, say each day, one winds up overestimating the spread of event rates because one's choices of λ are based on insufficient statistics, becoming influenced by upward and downward fluctuations rather than reflecting a true Poissonian average. On the other hand, a single averaged rate for the whole sample produces a distribution of events that is too narrow because it ignores real variations in the actual average background rate. Thus, an appropriate compromise was found splitting each year into five periods and using the average λ_j in each of the five periods for all time windows within that period.

So, using five periods with different λ's, one obtains a probability of obtaining

n or more events in any window of:

$$p = 1 - \prod_{j=1}^{5} (\sum_{i_j=0}^{n-2} \frac{\lambda_j^{i_j}}{i_j!} \exp(-\lambda_j))^{m_j} \tag{8.7}$$

where m_j is the number of events (hence time windows) in each of the five periods.

Our criterion for a "discovery" requires that the observed cluster of events has no more than a 5.73×10^{-7} probability of occurring as a chance fluctuation of background alone. This is after trials factors are accounted for, so to leave a little room for the possibility of signals resulting from coincidences with observed GRBs or sums of multiple bursts (see next chapter) the total chance probability for each of the two searches was not allowed to exceed 2.0×10^{-7} and still count as a discovery. Model discovery potential plots for the long and short searches are shown in Figure 8.3. The jagged nature of the plots is expected because the number of events needed to claim a significance of 5σ is a discrete quantity. It stands to reason that the minimum possible flux to have a 90% chance of obtaining a 5σ event will occur at a threshold where a certain number of events is just barely sufficient to claim significance. At the optimal cut for the 1 second search, a cluster of 5 events in a window would be required for a 5σ discovery whereas 7 events are required for the 100 second search.

8.3 Modeling the Distribution of Events Per Burst

The way the neutrino flux is divided between sources is important in this analysis because it counts clusters rather than individual events. One is more likely to get a significant cluster from one strong source than an ensemble of weaker ones occurring at different times, even if the net flux is the same. The experimentally motivated

distribution of expected events actually used in this analysis is based on calculations performed in Guetta et al. [55] and is therefore referred to in this thesis as the "Guetta" distribution. In addition, two much simpler assumptions were studied for comparison using 2001 data: a single burst distribution wherein all flux is concentrated in a single source and a flat distribution wherein each burst has equal flux. The three assumptions are summarized below and plots of sensitivity and Model Discovery Potential (MDP) are given for 2001 data in Figure 8.3.

8.3.1 Guetta Distribution

The "Guetta" Distribution is the most realistic model of burst distributions studied and therefore the one actually used in the analysis. The variable g in equation 8.3 is applied because all neutrino fluxes are not equal. Because of factors including distance from Earth, spectral shape and overall luminosity, the predicted number of neutrino events varies by several orders of magnitude from burst to burst. Predictions of the number of expected neutrino events in a kilometer scale detector were made for a large ensemble of real bursts by Guetta et al. in [55]. We fit a Gaussian to this distribution (see Figure 8.4). The variable g multiplies each burst by a random factor, weighted so that the overall distribution of signal strengths relative to the average will match this Gaussian. Thus, the majority of bursts will have the "average" signal strength or close to it, but a few will be much weaker and a few will be much stronger. Long and short bursts were fit separately, with the long burst fit applied to the 100 second search and the short burst fit applied to the 1 second search. In the short burst case, two gaussians were used to better match the distribution.

The Gaussian is fit in logarithmic rather than linear scale on the x-axis. When

sampling from this shape there is therefore a greater likelihood of getting a value above the peak than below it. To restore n in equation 8.3 to its original meaning of average number of events per burst, one must divide the result of the equation by 2.73 for the long burst set and 1.79 for the short burst set to adjust for this asymmetry.

In addition to adjusting each burst by some factor taken from this distribution, several other adjustments are made by randomly selecting which category a given burst falls into. Half of the bursts experience Earth shadowing effects, while the other half are unaffected by this loss of signal. There is also a 33% chance of a given burst falling into the short burst class, which dramatically decreases its expected fluence. Furthermore, for long bursts, roughly 7% of the time some non-negligible flux will be outside the search window because the duration of the burst exceeds 100 seconds. The percentage retained for each burst in this 7% is modeled by selecting a random retention rate from a distribution function estimated using the light curves of bursts in the BATSE 4b catalog.

8.3.2 Selection Effects

Obviously, since Guetta et al. have compiled predictions for bursts actually measured with the BATSE experiment, significant selection effects are present in this sample. There are many more GRBs occurring per year with jets aligned towards Earth than the nominal 667 per year detected by BATSE. However, since the more distant and less energetic bursts which do not provide sufficient gamma-ray output to trigger the detector will generally also not provide strong neutrino flux at Earth, the bursts observed by BATSE are generally the most relevant to neutrino searches (although there are caveats to consider, such as bursts with high baryon loading factors).

The redshift distribution of GRBs is currently a topic of much debate. Actual measured redshifts are not available for the vast majority of bursts from the BATSE era. The redshift distribution used by Guetta et al. assumes redshifts derived from the luminosity-variability relationship [92]. This distribution is significantly different than the distribution obtained through direct measurement of afterglow observations using the Swift satellite in concert with ground-based telescopes, which is itself still subject to selection effects due to detector thresholds. It has been postulated that the rate of GRBs may roughly match the star formation rate. Although sophisticated simulations of GRB distributions based on the Rowan-Robinson star formation rate have been performed [94], there is still a significant amount of uncertainty within this framework. It is currently not even clear whether all long bursts are part of the same distribution, as postulated in some papers (e.g. [93]), or whether low luminosity bursts such as GRB980425 and GRB060218 are a separate population from high luminosity bursts [39].

Hopefully, a clearer picture of the actual redshift distribution will emerge once more data has been collected (only $\sim$50 bursts have had redshifts directly measured so far [95]). Regardless, however, redshift assumptions have only a secondary effect on the predicted neutrino output in the final analysis. Refer back to Figure 4.4 for a comparison of predicted net neutrino fluxes for the Murase and Nagataki parameterization using both satellite observations and linking GRBs to the star formation rate for a demonstration of this point. Since this analysis is explicitly designed to be independent of satellite triggers, it would be ideal for it to use a parameterization that is also entirely independent of satellite selection effects, and this may be possible in

similar analyses in the future. However, the selection effects of treating only bursts which would trigger BATSE rather than more distant and less energetic bursts do not greatly affect the final result, making this primarily an aesthetic concern.

8.3.3 Single Burst Distribution

This alternate model assumes that instead of an ensemble of bursts, there is only one burst that has any significant neutrino flux. This is an unphysical model, but interesting to consider since it is a simplification of the realistic case in which a single burst dominates the neutrino contribution for the year. The optimal cuts using this distribution are quite similar to the "Guetta" distribution, discussed below, because that distribution also tends to be dominated by one, or at most a few, GRBs.

8.3.4 Flat Distribution

In the flat distribution, it is assumed that all bursts are equal and each burst therefore receives equal weighting. This is physically quite unrealistic, but it is in some sense the obvious "default" model. Since it is mathematically simple, it provides a convenient means of checking the sensitivity calculations employing Monte Carlo computer simulations and Feldman Cousins Likelihood Ratio Ordering against a simple back of the envelope calculation, presented below:

8.3.4.1 Back-of-the-Envelope Sensitivity Calculation Check

Mathematically, a 90% C.L. sensitivity calculation is different than determining the flux at which one has a 90% chance of seeing something above background. However, one expects they should generally have similar values. Here, we calculate the flux at which one has a 90% of seeing a fluctuation above background assuming 425

identical bursts (equivalent to the 2001 data set), which should correspond roughly to the sensitivity of 1.3×10^{-5} GeV cm^{-2} s^{-1} sr^{-1} which one obtains under the Feldman Cousins method when assuming equal flux for each burst.

To have a probability of 0.9 of detecting a signal, one has a 0.1 probability of failing to detect a signal. If there are 425 equivalent bursts during our ontime, then statistically, the odds of failing to detect any bursts is just the product of the probabilities of the failure to detect each burst individually. Thus:

$$0.1 = p^{425} \tag{8.8}$$

$$p = \sqrt[425]{0.1} \tag{8.9}$$

$$p = 0.9946 \tag{8.10}$$

where p is the probability of not detecting one individual burst. Since 5 events is outside the 90% confidence belt at 0 events, 5 or more events is above background for the purposes of this calculation, even though this would not be significant enough to label it a discovery. Assuming Poissonian statistics and counting 5 or more events as a "signal", the odds of failing to detect an individual burst with signal expectation λ is simply the odds of obtaining 4 or fewer events:

$$0.9946 = e^{-\lambda}(1 + \lambda + \frac{\lambda^2}{2} + \frac{\lambda^3}{6} + \frac{\lambda^4}{24}) \tag{8.11}$$

When solving for λ, one obtains an expectation of 1.1 events per burst. Multiplying this by the total expected number of bursts per year, 667[4], one obtains an expectation

[4] 425 is the approximate number of bursts occurring during the time when usable data was being taken, whereas 667 is the approximate number of bursts occurring over the course of the whole year.

of 733.7 events. One can then scale this with the total number of events one obtains from ANIS given a total flux of 1.3×10^{-8} GeV cm^{-2} s^{-1} sr^{-1} (summed events from ν_e, ν_μ and ν_τ with 4.5×10^{-9} flux each), which is 0.323, to scale up to the flux we are sensitive to.

$$\Phi = 4.5 \times 10^{-9} \text{ GeV cm}^{-2} \text{ s}^{-1} \text{ sr}^{-1} \times \frac{733.5}{0.323} \tag{8.12}$$

$$\Phi = 1.02 \times 10^{-5} \text{ GeV cm}^{-2} \text{ s}^{-1} \text{ sr}^{-1} \tag{8.13}$$

After correcting for deadtime, one obtains 1.3×10^{-5}GeV cm^{-2} s^{-1} sr^{-1}, identical to the sensitivity determined for the flat model for a single year. Thus, the calculated sensitivity resulting from the confidence belt constructions is consistent with this simpler estimate.

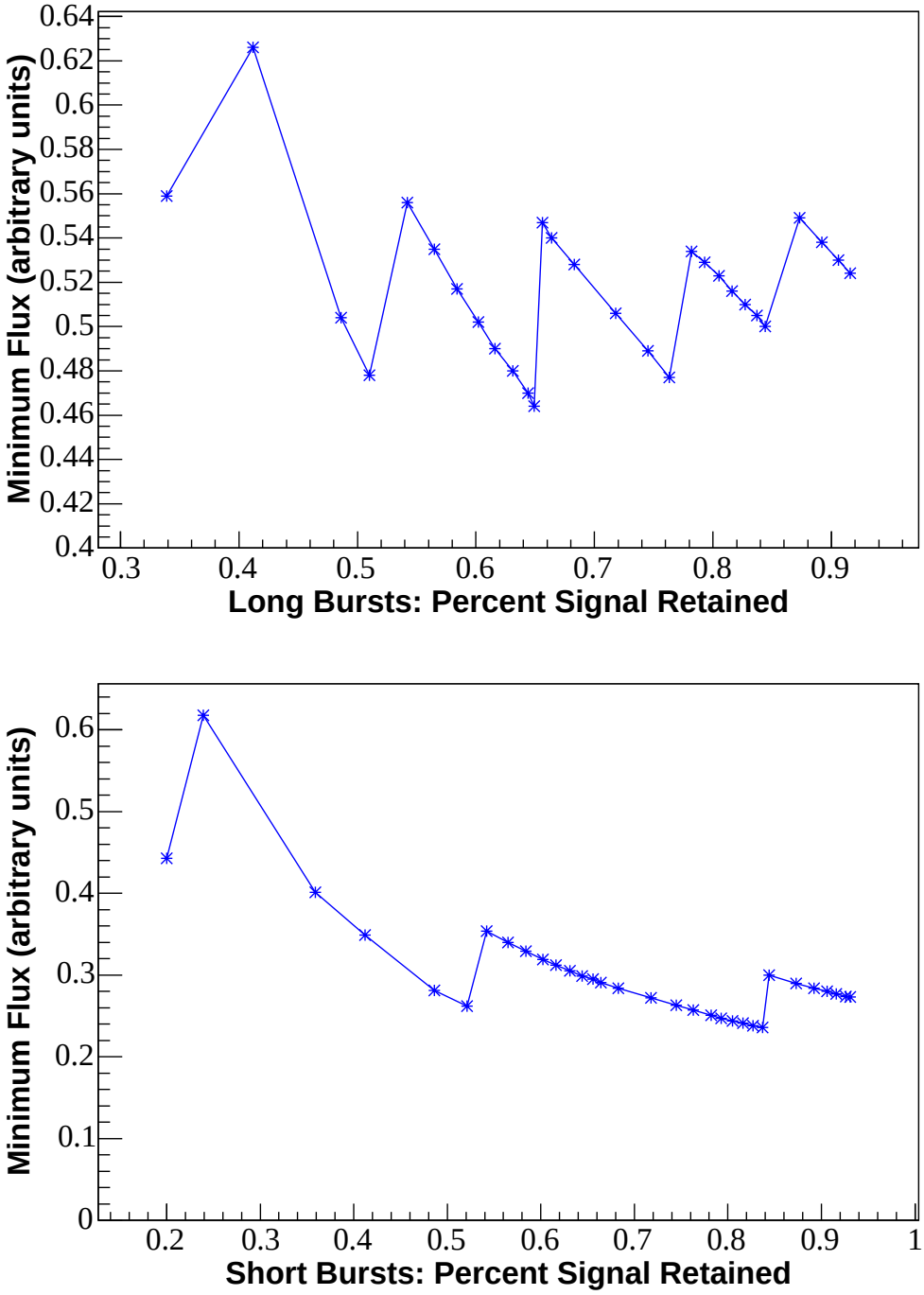

Figure 8.3: Minimum flux needed to have a 90% chance of getting a 5 σ detection as a function of signal retention for long and short duration searches.

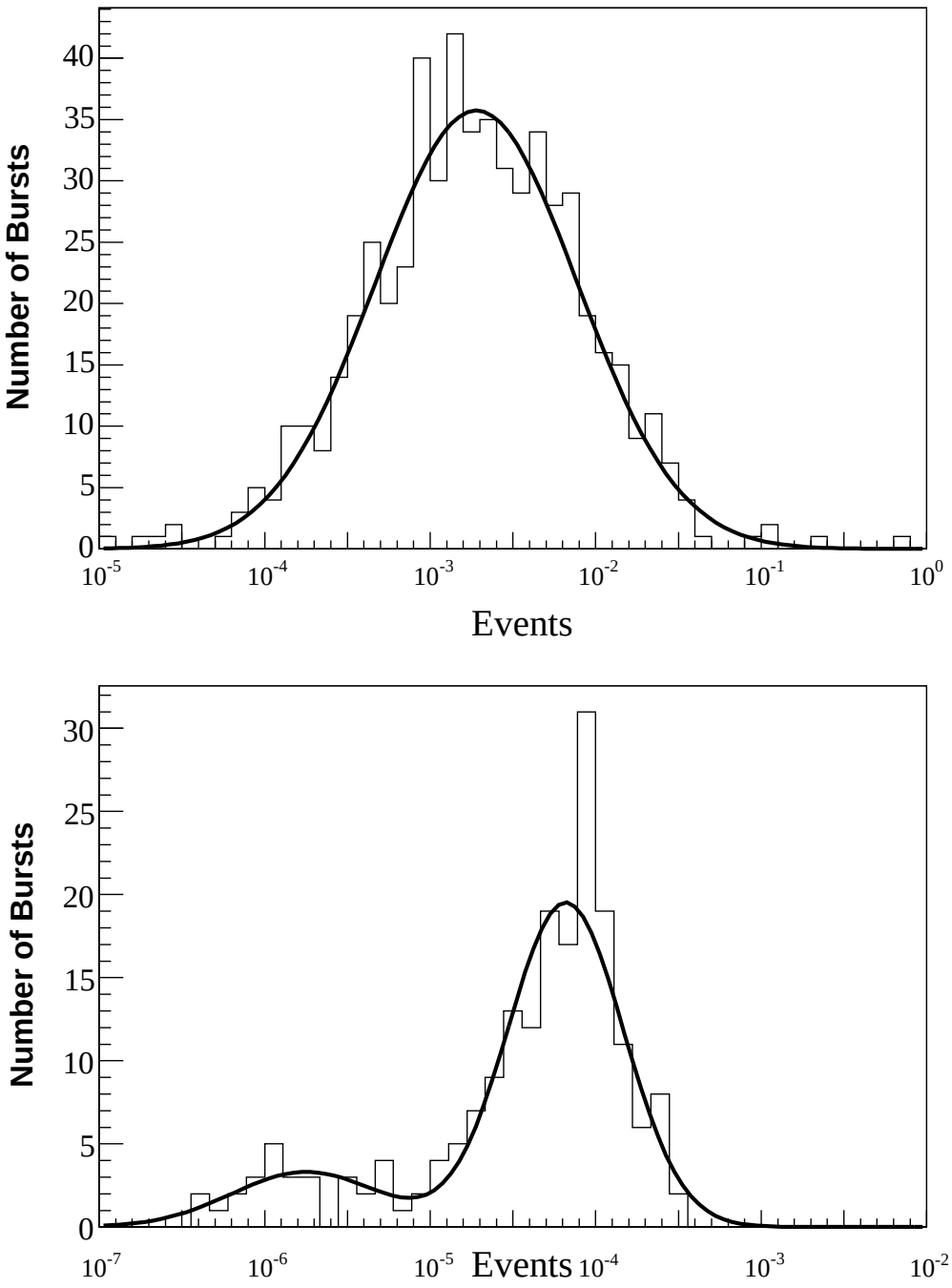

Figure 8.4: Distribution of predicted observable neutrino events from GRBs in a km^3 detector for long (top) and short (bottom) duration burst classes.

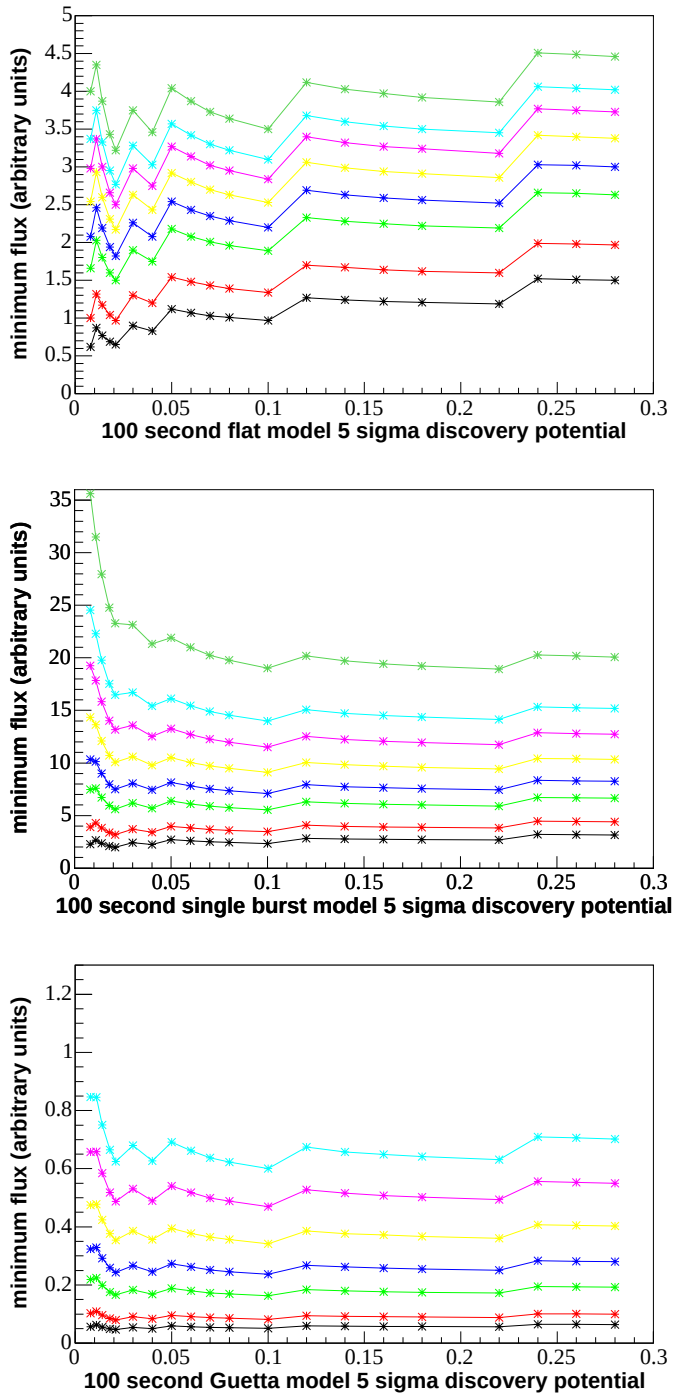

Figure 8.5: Model Discovery potential functions for three different distributions of events per burst, with statistical power ranging from 1% to 99%.

Chapter 9

Significance of a Detection and Systematics

The rolling search is optimized to identify a single burst, since all current predictions indicate that detection would require an anomalously close and/or bright event. However, it is also possible that two or three separate events, while not significant in themselves, would lead to a statistically significant observation when taken together. (An object like a soft gamma repeater, for example, may have multiple "bright" periods, or there may really be multiple GRBs.) Additionally, a cluster of events which is not statistically significant in and of itself may become statistically significant if it is observed to be in coincidence with a gamma-ray trigger of a satellite. Even though the rolling search ignores satellite coincidence, it is still reasonable to make an *a posteriori* check against the times that these occurred.

In order to have a mathematically well-defined probability of false detection, it was necessary to carefully define all scenarios to be checked before the unblinding. These are summarized in the following two sections. Systematic uncertainties are then discussed in Section 9.3.

9.1 Checks for γ-ray coincidence

For our purposes a time window is defined as "in coincidence" with a satellite trigger if any part of the window overlaps with any part of the duration of the measured prompt γ-ray emission. Aside from being the only practical way to define this, it also tacitly accounts for the possibility of an observation of precursor neutrinos, since a detection starting roughly 100 seconds before the trigger time will still count as being "in coincidence" in the long duration search. Given 1 cluster of n events, the odds of it occurring in coincidence with a burst are, to good approximation, simply

$$\frac{(N_{\text{bursts}} \times \text{ time window length} + \text{total duration of all bursts})}{\text{total livetime}} \tag{9.1}$$

Based on this data and a compilation of triggers from the IPN satellite network, in the 100 second search a cluster of 6 events would have a significance greater than 5σ and a 4 or 5 event cluster would have a significance greater than 4σ. Similarly, for the 1 second search, a 4 event cluster would have a significance greater than 5σ and a 3 event cluster would have a significance greater than 4σ.

The approximate durations and trigger times used in this analysis are given for 2001, 2002 and 2003 respectively in the following 3 tables. In the first column is the year, month and day in the format normally presented for GRB triggers. For example, March 17, 2002 reads as 020317. The second column is the time of day in seconds (using Greenwich Mean Time). The final column is approximate duration. Where possible, externally approved values were used, particularly in the case of those used in previous satellite-coincident analyses [61], but many were estimated based on the light-curves provided by Konus-Wind [96] and should be considered approximations

only. However, these values are sufficient for an *a posteriori* check.

2001 Triggers

Y/M/D	Time(s)	Duration(s)		Y/M/D	Time(s)	Duration(s)
010220	4488668.66	9		010222	4605791.65	26
010222	4650184.16	6		010224	4769357.83	19
010226	4994114.24	12		010304	5462335.99	5
010305	5533503.17	19		010306	5697344.65	21
010308	5845138.47	2		010315	6447669.86	7
010317	6589691	2		010326	7355700.54	25
010327	7499741.8	8		010408	8491522.83	5
010420	9534786.67	1		010420	9585483.16	2
010427	10176252.97	1		010429	10362163.9	6
010502	10547957.43	2		010504	10723432.03	11
010508	11107028.28	15		010517	11922694.19	22
010520	12097887.72	15		010522	12338066.05	3
010522	12343910.66	11		010523	12372259.05	12
010526	12671986.75	32		010526	12678903.05	13
010530	12992067.67	5		010607	13704923.52	12
010611	14076366.97	6		010612	14092398.83	28
010613	14196841.69	12		010613	14217788.36	5
010615	14386466.06	9		010616	14448924.03	1
010619	14698706.24	13		010619	14743023.77	3
010623	15046274.63	8		010624	15168929.13	2
010625	15269310.04	5		010628	15534018.4	12
010628	15469806.82	2		010629	15596467.23	14
010701	15727589.58	15		010706	16186745.01	33
010710	16587251.59	20		010721	17467011.43	5
010723	17689356.58	20		010725	17859688.51	8
010726	17890282.53	6		010729	18183325.29	9
010801	18469829.78	33		010802	18520516.71	5
010804	18735204.93	14		010806	18847924.67	2
010813	19475042.27	8		010818	19921995.91	2
010821	20179623.55	30		010826	20628453.59	15
010828	20751498.35	5		010902	21210114.82	1
010903	21338874.45	17		010903	21288644.59	30
010917	22470336.04	1		010918	22606273.79	14
010921	22828557.15	16		010922	22959413.75	18
010923	23016271.26	6		010928	23475226	29
011004	24006552.8	35		011008	24350152.99	15
011016	24998199.99	5		011018	25165379.11	5

2002 Triggers

Y/M/D	Time (s)	Duration (s)		Y/M/D	Time(s)	Duration (s)
020214	3955773.43	20		020218	4264863.11	1
020218	4304952.45	30		020221	4522074.34	20
020226	4983222.24	5		020302	5315019.69	23
020303	5438840.22	6		020304	5446947.12	26
020306	5684280.71	1		020311	6056492.73	13
020313	6225471.76	22		020317	6632131	10
020326	7383182.94	1		020327	7439169.36	29
020402	7954371.93	18		020402	7977305.02	10
020404	8158457.35	1		020405	8210499.5	30
020406	8360295	130		020407	8396077.86	23
020409	8629885	59		020413	8958015.2	10
020417	9264984.35	9		020418	9362312.8	15
020418	9394984.89	5		020426	10108571.05	1
020429	10284535.83	7		020430	10369609.16	6
020430	10444919.45	9		020504	10769435.14	10
020508	11074019.62	3		020508	11133711.26	2
020509	11145674.56	2		020514	11644557.33	11
020525	12544014.63	1		020525	12548164.12	30
020530	13022544.17	18		020602	13256514.31	2
020602	13282230.32	1		020603	13369833.99	2
020604	13443223.21	7		020608	13775629.9	16
020609	13825745.67	8		020620	14821090.34	3
020623	15049383.3	13		020625	15247549.3	125
020630	15662246.74	13		020630	15667131.13	0
020706	16169426.83	30		020708	16346050.94	150
020712	16697386.87	3		020714	16904970.69	20
020715	16989266.14	1		020715	17004063.04	10
020715	17014660.45	9		020730	18252473.07	1
020731	18318435.9	1		020731	18367031.74	1
020801	18445959.42	4		020803	18602931	8
020813	19449880.65	25		020819	19987001.06	1
020819	20012259.77	20		020821	20190843.48	5
020828	20756737.98	1		020904	21365621.69	18
020908	21691102.73	12		020910	21931051.87	24
020911	22010415.79	3		020914	22221610.15	5
020914	22283598.85	12		020020918	22597692.5	4
020923	23029582.58	5		020924	23087411.99	1
020926	23259162.72	22		021004	23976373.6	100
021008	24303650.6	26		021008	24330603.19	13
021013	24724896.86	8		021014	24820308.9	11
021016	25007384.74	50		021020	25387972.53	20
021023	25584825.67	9		021025	25820311.15	11
021027	25950831.05	13				

2003 Triggers

Y/M/D	Time (s)	Duration (s)		Y/M/D	Time(s)	Duration (s)
030225	4892573.55	7		030226	4938392	100
030227	5042520	20		030228	5171212.16	10
030301	5257644	30		030304	5528064.73	3
030306	5629078.98	18		030307	5754719.63	4
030308	5807904.83	8		030317	6591529.2	20
030320	6862319.3	14		030320	6893362.81	28
030324	7182762	12		030325	7308909.99	3
030329	7645049.25	25		030329	7659258.82	17
030331	7796320.34	25		030403	8048269.46	8
030405	8216253.08	5		030406	8376127.54	19
030410	8681025.17	1		030413	8926479.56	15
030414	9035307.76	19		030419	9421927.38	30
030421	9592590.53	13		030422	9705080.07	10
030422	9709286.71	12		030422	9739584.15	4
030425	9992911.06	500		030426	10106999.61	11
030428	10276278.88	12		030429	10306288.5	5
030501	10459041.82	6		030501	10529090.26	8
030505	10832605.6	15		030506	10893851.47	27
030509	11166620.73	9		030509	11208505.42	11
030514	11643750.9	12		030518	11928223.89	27
030518	11934738.64	19		030518	12000522.95	16
030519	12060299.08	2		030523	12406249.12	1
030523	12411059.45	30		030601	13212726.95	20
030605	13486819.53	6		030605	13554385.93	2
030606	13650470.86	13		030607	13659557.39	1
030614	14261441.66	20		030620	14836254.44	23
030626	15299211.11	40		030629	15564404.1	1
030629	15599336.31	15		030706	16156935.26	10
030709	16454245.76	27		030710	16585501.09	7
030714	16928091.49	6		030715	16950350.86	10
030721	17538072.2	30		030722	17587900.69	27
030725	17840788.68	16		030726	17908712.1	30
030801	18463909.18	29		030806	18846610.15	10
030808	19064868.59	8		030814	19537572.57	9
030817	19787067.7	50		030821	20151096.97	17
030822	20284827.76	26		030823	20335690.6	79
030824	20450855.1	16		030827	20707720.9	5
030830	20975853.81	21		030831	21049624.21	23
030903	21310999.22	3		030908	21696371.11	14
030913	22180017.5	8		030916	22456758.38	1
030919	22713037.95	14		030921	22840703.28	16
030922	22927404.12	21		030922	22962648.56	15
030926	23043147.27	1		030929	23552835.43	1
031004	24009250.94	7		031007	24228731.23	5

9.2 Checks for statistical significance from multiple bursts

The following combinations of events would have a statistical significance greater than 5σ:

- A single occurrence of 7 events in the 100 second search
- A single occurrence of 5 events in the 1 second search
- An occurrence of 6 events and an independent occurrence of at least 5 evenets in the 100 second search
- Three independent occurrences of at least 5 events in the 100 second search
- Two independent occurrences of 4 events in the 1 second search
- Two independent occurrences of at least 5 events in the 100 second search and one occurrence of 4 events in the 1 second search

The following scenarios would have a significance greater than 4σ:

- One 6 event window in the 100 second search
- Two independent 5 event windows in the 100 second search
- One 4 event window in the 1 second search

Likewise, one 5 event window and at least one 4 event window in the 100 second search would have a significance greater than 3σ but less than 4σ. Given only Poissonian background, the total probabilities of all scenarios which are listed as being considered a "discovery" are below the 5.73×10^{-7} probability needed to be considered a $\sim 5\sigma$ discovery (likewise for the appropriate probabilities for 3σ and 4σ). This

is summarized in the following table:

Discovery Scenario	Probability
7 events in long time window	2.0×10^{-7}
5 events in short time window	2.0×10^{-7}
2 or 3 event combinations	1.2×10^{-7}
IPN coincidence	0.2×10^{-7}
Total	5.4×10^{-7}

These possibilities are added linearly, since the coupling of any two of these scenarios is extremely weak (well under a percent difference in the end result) assuming only stochastic background.

9.3 Systematic Uncertainty

Because AMANDA is constructed in a natural medium and deals with higher energy ranges, its systematic uncertainties tend to be larger than those of other neutrino experiments. Each of the uncertainties in the signal efficiency described below is taken as a separate nuisance parameter and treated as described in section 8.1.3. Since the background is directly measured from real data, no uncertainty in background rates was assumed.

9.3.1 Ice Properties

There is significant uncertainty concerning the properties of the ice in which AMANDA was deployed. Although Antarctic ice is remarkably clear for a natural medium, the propagation of light is affected by a number of properties which are imperfectly modeled in our computer software, particularly the layers of dust which influence absorption and scattering. Whereas muon analyses generally use layered ice

models with relatively clear and dusty layers, these do not work as well for cascades, so cascade simulations use a single average ice model. The potential effect of systematics on the final result was estimated by simulating Monte Carlo with the most extreme properties possible, both dustier and more clear, in addition to the normal average ice properties. Average scattering lengths are 14 m, 24 m and 28 m for dusty, normal and clear ice, respectively. Taking these dusty and clear extrema as the possible bounds for the real ice properties, then propagating the signal Monte Carlo through all stages of the analysis, one obtains roughly a $\pm 50\%$ uncertainty in the signal retention, which we treat as a flat error. It should be pointed out that taking the possible extrema is a very conservative approach and cascade analyses have a larger uncertainty due to ice properties than do muon analyses.

9.3.2 OM Sensitivity

OM sensitivity was varied by $\pm 10\%$ by shrinking or enlarging the modeled photomultiplier tube surface area in the AMANDA geometry files. This has an overall effect of $\sim \pm 5\%$ in the overall signal generated. For 2001 data, OM sensitivity and Ice Properties were also varied in the same files, creating a total of 9 possible scenarios (dusty and low sensitivity, dusty and normal sensitivity, et cetera). The results showed no unexpected correlations, so the Sensitivity and Ice Properties uncertainties were treated as independent parameters. The net effect of the OM Sensitivity uncertainty is of course very small, since it is a full order of magnitude less significant than the largest uncertainty.

9.3.3 Distribution of events per burst

As discussed in section 7.3.3, since this analysis looks for a cluster of events in temporal coincidence, the way the net neutrino flux is distributed between events is very important. The burst-to-burst distribution of the detectable neutrino flux will depend on several factors of varying significance, including total photon fluence, distance from Earth, spectral shape and baryon loading. Many competing models exist for predicting neutrino event rates from GRBs. In [55], two of these models are used to create distributions of expected neutrino event rates at Earth, specifically one modeling proton-photon interactions in the GRB jet and the other assuming a "supranova" progenitor and thus including proton interactions with pulsar wind photons. Additionally, each model is calculated using two different sets of assumptions, giving a total of 4 rate predictions. In the case of the first model, calculations are made both assuming the energy fraction transferred to pions is fixed and assuming the energy fraction varies according to an approximate formula. In the case of the second model, event rate calculations are made assuming two different timescales between the supranova and the GRB.

Based on the difference in sensitivity when these different relative event rate distributions are used as the underlying assumption, the net uncertainty resulting from variations in the distribution of signal events is taken as 20%. Since the model-to-model difference was considerably larger than the uncertainty of the individual fits themselves, no additional adjustment was made for the fit uncertainty.

9.3.4 Variations in actual spectra

The actual values of the break energies for a given burst affect the energy distribution of the expected neutrino events. Changing break energies therefore alters the signal efficiency of the cuts compared to the "averaged" Waxman-Bahcall spectrum (with breaks at 10^5 and 10^7 GeV) which was the assumed signal input in the analysis. The "Guetta" distribution accounts for variations in shape and normalization up to the trigger level of the detector, but naturally does not take into account the differing signal efficiencies when the specific cuts of this analysis are applied. Variation in the higher break energy does not impact the results strongly and is near its nominal value of 10^7 GeV for the majority of bursts contained in [97]. However, when holding the synchrotron break at 10^7 GeV but varying the lower break energy, the signal efficiency at E_b=10^4 GeV is only 70% of what it is at the nominal value E_b=10^5 GeV and 142% as great at E_b=10^6 GeV. The signal efficiency relative to a burst with 10^5 GeV break energy roughly follows the empirical fit:

$$\frac{\epsilon_{\mathrm{E}_b}}{\epsilon_{10^5\mathrm{GeV}}} = log10(6.44E_b)/2.74 \tag{9.2}$$

The gaussian "Guetta" distribution described in section 8.3.3 was adjusted by modifying the predicted neutrino event rates for BATSE bursts found in [97] by the above formula. After this adjustment was made, the change in the resulting Gaussian fit was within the uncertainties of the original gaussian fits themselves and considerably less than the difference between the fits resulting from various models. On a burst by burst basis, the predicted observed neutrino flux can vary substantially, but it appears that these differences more or less average out over the entire ensemble. Therefore no

adjustment has been made for varying signal efficiency due to changes in spectral shape, and this can be considered to be included in the 20% uncertainty for the way in which events are distributed among the ensemble of bursts.

Chapter 10

Results

10.1 Experimental Results

As defined in Chapter 8, our experimental observable is N_{large}, the maximum number of events observed in any window. Upon unblinding, N_{large} was 2 in the 1 second analysis, a result that is 70.1% probable assuming only background. N_{large} in the 100 second search was 3, a result that is 75.3% probable under the assumption of only stochastic background. Thus, there is no evidence of a GRB or other transient in the 2001-2003 dataset.

10.2 Doublet and Triplet Distributions

Not only is the largest number of events observed consistent with expectations, but the total number of occurrences of 2 or 3 events per bin is consistent with background expectations as well. Background event distributions were simulated for the entire 3 year sample using 10000 iterations of toy Poissonian computer simulation. The simulation was done with separate Poissonian rates for 5 periods in each year, in the same manner as the calculations used to determine model discovery potential (see

section 8.2). The total number of doublets (windows with 2 events) in both the 1 and 100 second search and triplets (windows with 3 events) in the 100 second search for each Monte Carlo trial produce roughly gaussian distributions, plotted in Figure 10.1. The actual number of doublets and triplets observed are superimposed on these plots. They demonstrate that the actual results are quite consistent with the background expectation (well within 1σ uncertainties), arguing strongly against any significant influence from non-stochastic unphysical events. The plots are for all 3 year-long data sets combined. Distributions of doublets and triplets show a reasonable spread between years. A summary of individual event times for doublets in the 1 second search and triplets in the 100 second search is given in Appendix A. The year-by-year breakdown of doublets and triplets is as follows:

	2001	2002	2003	total
Doublets in 1 Second	95	102	114	311
Doublets in 100 Seconds	328	321	351	1000
Triplets in 100 Seconds	6	8	6	20

10.3 Testing Models of Neutrino Emission

Although the analysis was optimized based on the averaged Waxman-Bahcall spectrum, it is possible to examine several of the model predictions shown and discussed in sections 4.3 and 4.4. The following table summarizes the Model Rejection Factor (if available), expected number of events per year before the final SVM cut and average percent retention through the support vector machine cut. A limit plot for these various models is shown in Figure 10.2. All numbers assume the 100 second search time window cuts. Specific details of the assumptions made for each case are given in the remainder of this section.

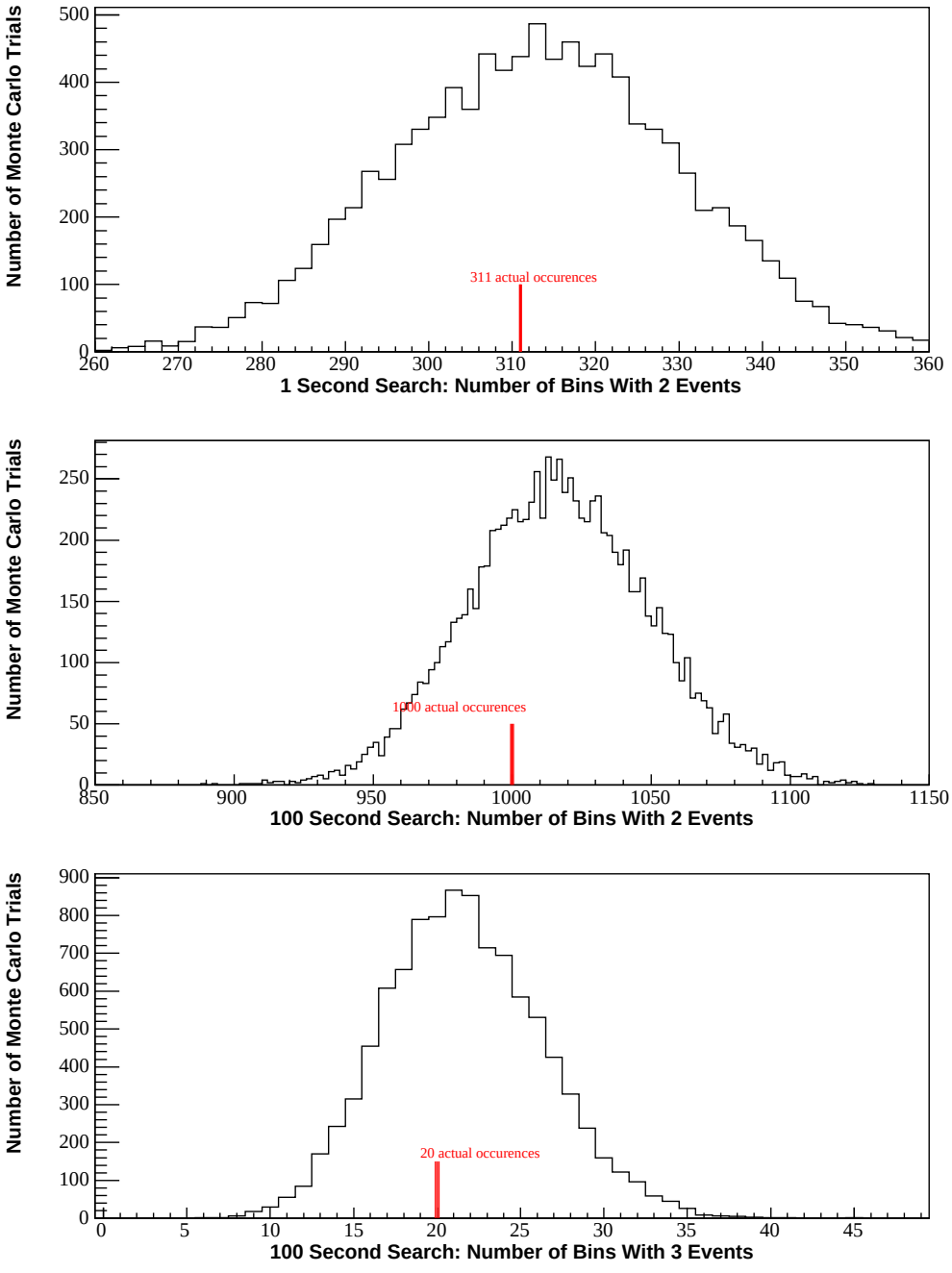

Figure 10.1: Number of doublets and triplets in real analysis compared to distribution produced by computer simulation. The distributions of simulated events are approximately Gaussian, and the actual numbers of observed events are well within the 1σ error bars in each case.

Model	MRF	Events/Year	Energy Range	% Kept
Waxman Bahcall spectrum	120	0.373	70 TeV to 8 PeV	63.9%
Murase Nagataki (Model A)	94	1.22	100 TeV to 10 PeV	75.0%
Supranova (top curve)	41	2.11	50 TeV to 7 PeV	49.1%
Choked Burst	72	0.055	13 TeV to 5 PeV	18.7%
Afterglow	n/a	0.0044	n/a	84.5%

10.3.1 Waxman-Bahcall flux

Assuming a flavor ratio at Earth of 1:1:1, as has traditionally been done for AMANDA analyses, the limit set by this analysis by the flux of all neutrino flavors from GRBs is $E^2\Phi = 1.6\times10^{-6}$ GeV cm^{-2} s^{-1} sr^{-1} (referring to the E^{-2} portion between the two break energies). This is presented as a diffuse flux by averaging the emission of 667[1] transient point source GRBs over the whole year and the entire sky. Without the inclusion of systematic errors, the limit would be 1.2×10^{-6} GeV cm^{-2} s^{-1} sr^{-1}. If one ignores the other two flavors, the limit on ν_e emission alone would be 9.7×10^{-7} GeV cm^{-2} s^{-1} sr^{-1}. Adjusting for the transition to a flavor ratio of 1:1.8:1.8 at high energies would result in a $\sim$10% reduction in the limit.

10.3.2 Murase-Nagataki flux

The MRF shown assumes 690 total bursts per year, as Murase and Nagataki themselves did for this model. The predicted flux, however, only results from the long burst sub-class (short bursts were not modeled). Since both ν_μ and ν_e spectra at source were provided, precise oscillation calculations have been applied and it was unnecessary to assume a 1:1:1 flavor ratio. Since the ν_e and ν_μ spectra are different, the exact flavor ratio varies as a function of energy.

[1] This is the number of observable bursts as based on the detection rate by BATSE.

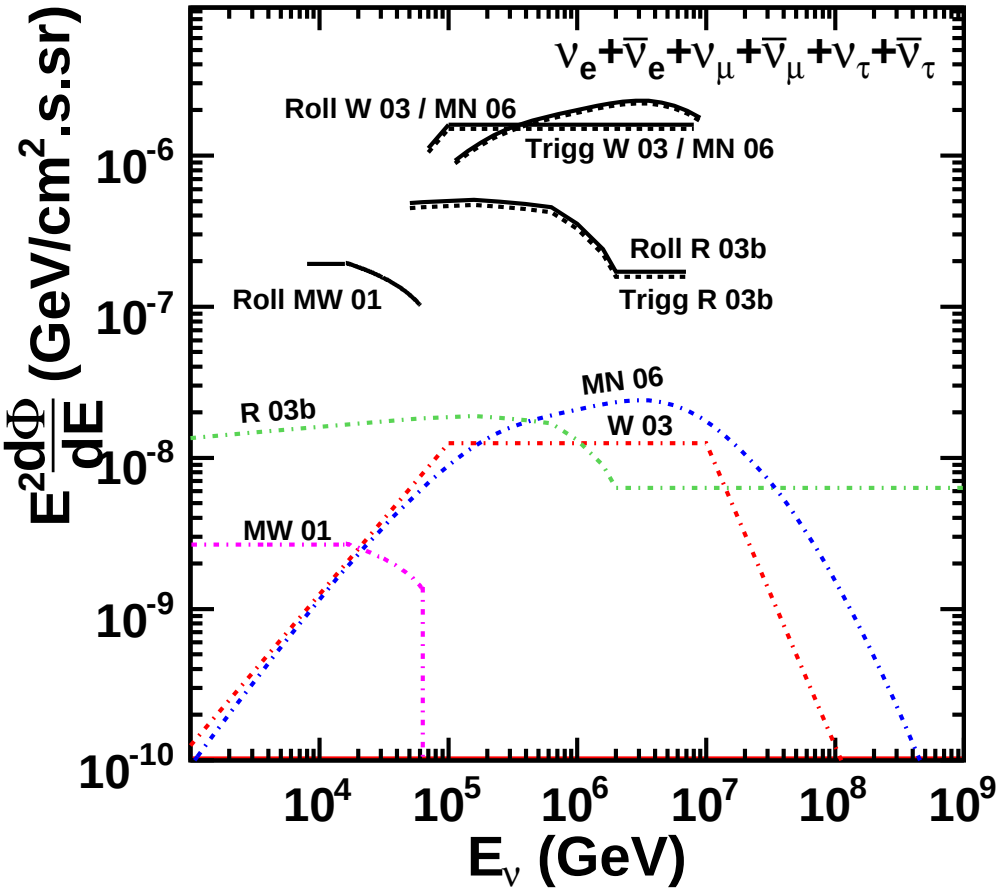

Figure 10.2: Limits relative to various models of GRB neutrino emission. Solid lines are for this rolling analysis, dashed lines are for the 73 burst 2000 cascade triggered analysis [63]. The plotted ranges are for the central 90% of events. Models shown are Waxman-Bahcall (W 03), Murase and Nagataki (MN 06), Razzaque's supranova model (R 03) and Meszaros and Waxman's precursor/choked burst spectrum (MW 01).

10.3.3 Supranova Model

Signal retention for the predicted supranova model emission is only slightly worse than for the collapsar model. Since the supranova model applies only to long bursts, sensitivity was evaluated considering only the long burst class and the 100 second time window. For the 3 year analysis, one obtains a Model Rejection Factor of 35 relative to the top supranova flux in Figure 4.5. This flux is summed with emission from the standard broken power law spectrum as well, because the processes generating the two spectra both contribute to the total neutrino flux in the supranova scenario [55]. Ignoring the broken power law contribution, the Model Rejection Factor becomes about a factor of 41.

10.3.4 Choked Burst Sensitivity

As discussed in section 3.4.1, choked bursts have a considerably different predicted neutrino spectrum compared to prompt GRB emission. Since the choked burst spectrum peaks at lower energies, signal retention is considerably worse in comparison with the prompt emission spectrum. The analysis in its current form is not sufficiently sensitive to precursor/choked burst emission to rule out any predictions. The factor by which the sensitivity would need to be improved depends on the unknown choked burst rate. However, since one must still get a fluctuation from an individual source and the choked burst rate increases the number of sources, not their average strength, one does not get a linear improvement in the model rejection factor by increasing the number of sources. The current analysis is approximately a factor of 1100 above sensitivity considering only precursor emission from GRBs themselves, a factor of 380 if choked bursts are 10 times as prevalent as conventional GRBs and a factor of 60 if

choked bursts are 100 times as prevalent. This last factor is roughly what one obtains if the rate of choked GRBs is tied to the rate of type-II supernovae. An analysis optimized for this lower energy spectrum could of course do somewhat better, although the improvement that would be possible would probably not justify this being done for AMANDA.

10.3.5 Afterglow Emission

The analysis was not optimized to afterglow emission, either by signal spectrum or time window length. In fact, the timescale for afterglow emission is not a well-determined quantity and certainly requires letting in much more background than prompt searches. However, an *a posteriori* check was done comparing the number of events observed in the 1000 seconds following the IPN burst triggers. This was compared to expectation and found to be entirely consistent with background.

10.3.6 SGR

Since soft gamma repeater flares generally occur on a timescale of tenths of a second, the 1 second time window is appropriate for attempting to identify this phenomenon. It is difficult, however, to place meaningful limits on SGR emission since neutrino event rates vary by orders of magnitude depending on both the slope of the power law and normalization, which are not well-constrained. Considering the "monster" flare on December 27, 2004, the neutrino spectrum calculation 8.74×10^{-3} $(\mathrm{E/GeV})^{-1.47}$ cm^{-2} s^{-1} GeV^{-1} found in [58] would generate a few neutrino-induced cascade events per second which, given the rolling search cuts' $\sim$95% signal retention for this very hard spectrum, would be sufficient for a detection. On the other hand, if

the more conservative and softer spectral fit 8.23×10^{-5} $(E/GeV)^{-2}$ cm^{-2} s^{-1} GeV^{-1} is used, the neutrino flux is many orders of magnitude lower than is needed, even though signal retention during the 1 second search Support Vector Machine cut is still very good for an E^{-2} spectrum ($\sim$82% for muon cascades to $\sim$86% for electron cascades) .

10.3.7 Cosmic Strings and Other Exotic Neutrino Sources

It should be kept in mind that there are other potentially surprising sources of high energy neutrino bursts to which a rolling search could be sensitive which have not been tested. One example of these more exotic models is neutrino emission from cosmic strings, either through cusp formation [98] or through cosmic string decay [99]. Predicted spectra for neutrinos from cosmic strings generally peak in the UHE ($> 10^{10}$ GeV) range, which is above the energy range normally considered for this analysis, but should have very good signal retention (similar to 10^9 GeV neutrinos, which also saturate the detector). Given that the rolling search looks for a transient on a fairly small time-scale, a detection in this analysis would most likely require a decay of a particularly close-by string.

10.4 Neutrino Effective Area

Conceptually, effective area is the surface area of a theoretical perfect detector which detects signal events at the same rate as the real detector, but does not miss any events that pass through it. A detector with surface area 50 cm^2 that detects one out of every 50 particles passing through it has an effective area of 1 cm^2. Mathematically, this is represented as:

$$A_{\nu}^{\mathrm{eff}}(E_{\mathrm{lower}}, E_{\mathrm{upper}}) = A_{\mathrm{gen}} \frac{n_{\mathrm{sig}}}{n_{\mathrm{gen}}} \tag{10.1}$$

where n_{sig} events are successfully reconstructed and survive all cuts out of n_{gen} total events passing through the detector area A_{gen}. Neutrino effective area is a function of energy, so a given value of the area is valid only for a particular energy range $\mathrm{E_{lower}}$ to $\mathrm{E_{upper}}$. Effective area plots for ν_e and ν_τ are shown in Figure 10.3. These plots incorporate Earth shadowing effects and are thus shown for several angular ranges. Neutrino effective areas are of course generally much smaller than the physical surface areas of a neutrino detector because the vast majority of the neutrinos passing through do not interact at all with the detector medium.

Effective area is in some sense the most generic measurement of the capabilities of a detector. It is model independent, but one can fold in the effective area as a function of energy with any model to obtain event rate predictions. For example, the effective area plots have been multiplied by the generic Waxman-Bahcall neutrino energy function used in this analysis and the atmospheric neutrino spectrum to obtain the relative number of expected detectable neutrino events as a function of energy, shown in Figures 10.4 and 10.5.

10.5 Cascade Effective Volume

Effective volume is closely related to effective area. Cascade effective volume is a measure of the detector's ability to detect neutrino events that have produced electromagnetic or hadronic cascades. In close analogy to equation 10.1 effective volume is defined as:

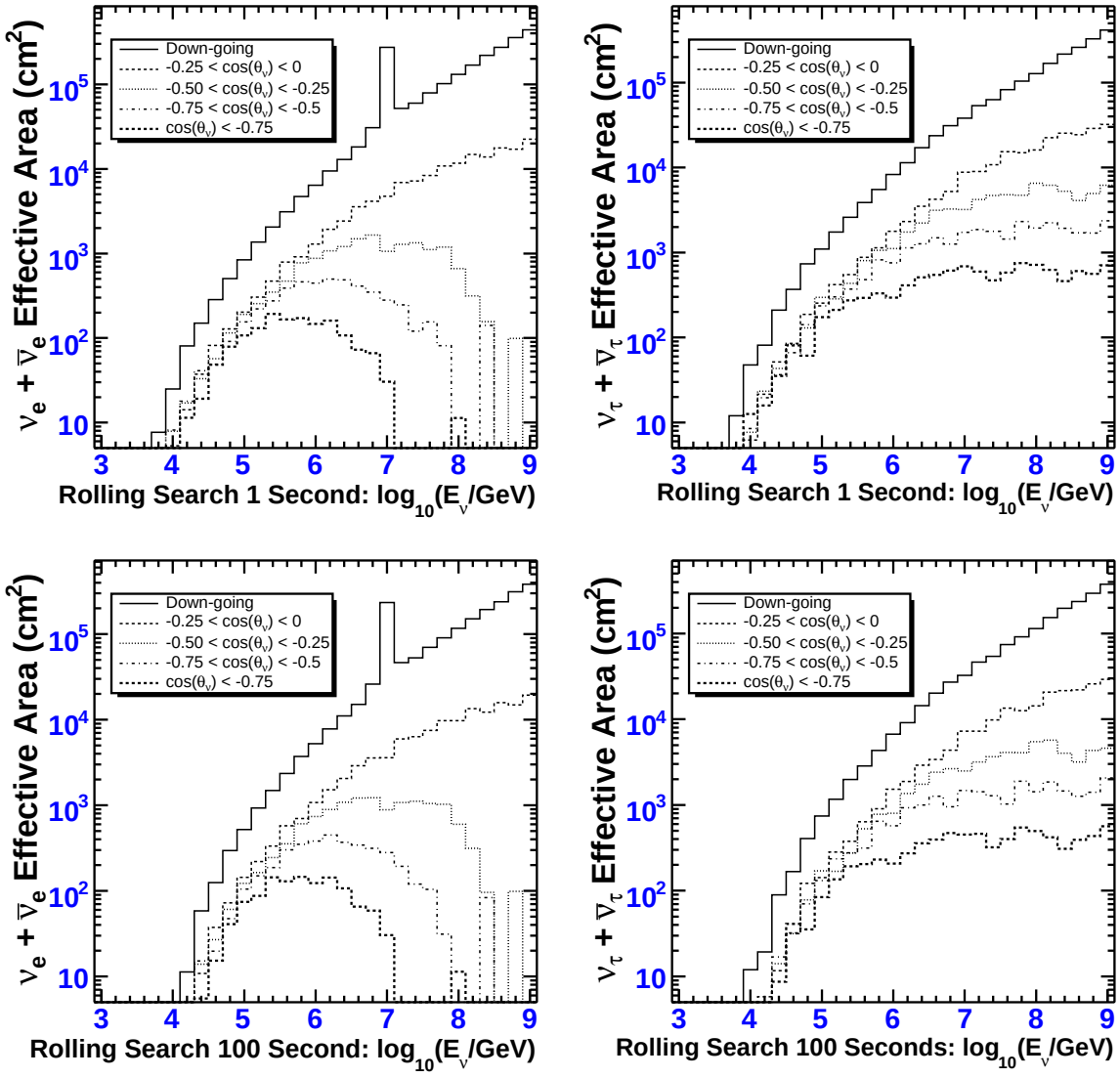

Figure 10.3: Neutrino effective areas as function of neutrino energy (at Earth surface) and $\cos\theta_\nu$ for the rolling analysis after all selection criteria have been applied, for both 1 and 100 second search windows. The peak at 6.3 PeV is due to the Glashow resonance for $\bar{\nu}_e$. The effective areas for ν_τ for upgoing events are larger than for ν_e because of charged current regeneration. ν_μ neutral current interactions also make a small contribution to the total flux, but this is much less significant.

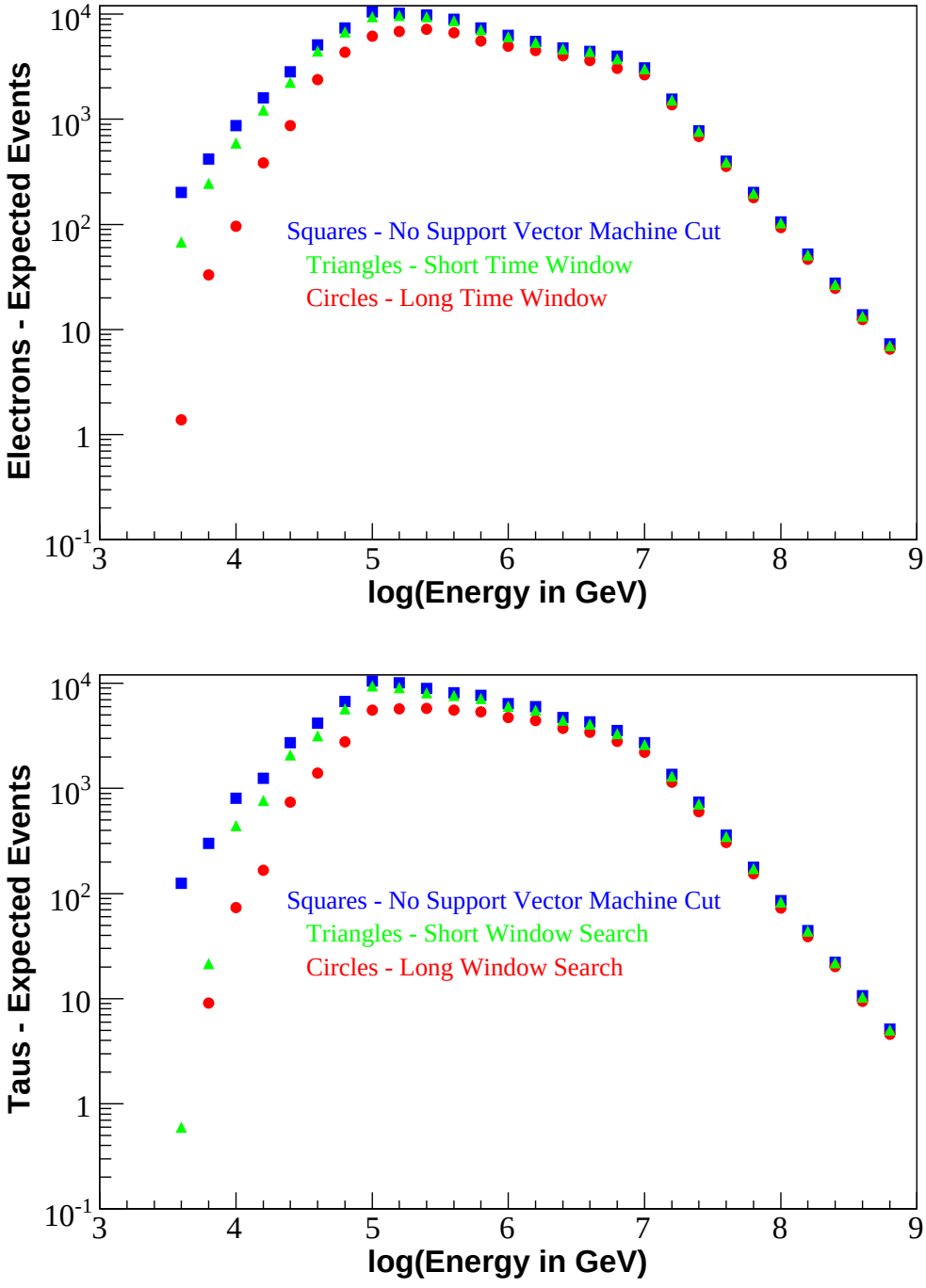

Figure 10.4: Expected relative number of events from the Waxman-Bahcall spectrum (arbitrary normalization) surviving given particular cuts, as a function of energy. These values are obtained by folding the predicted spectra with the effective area.

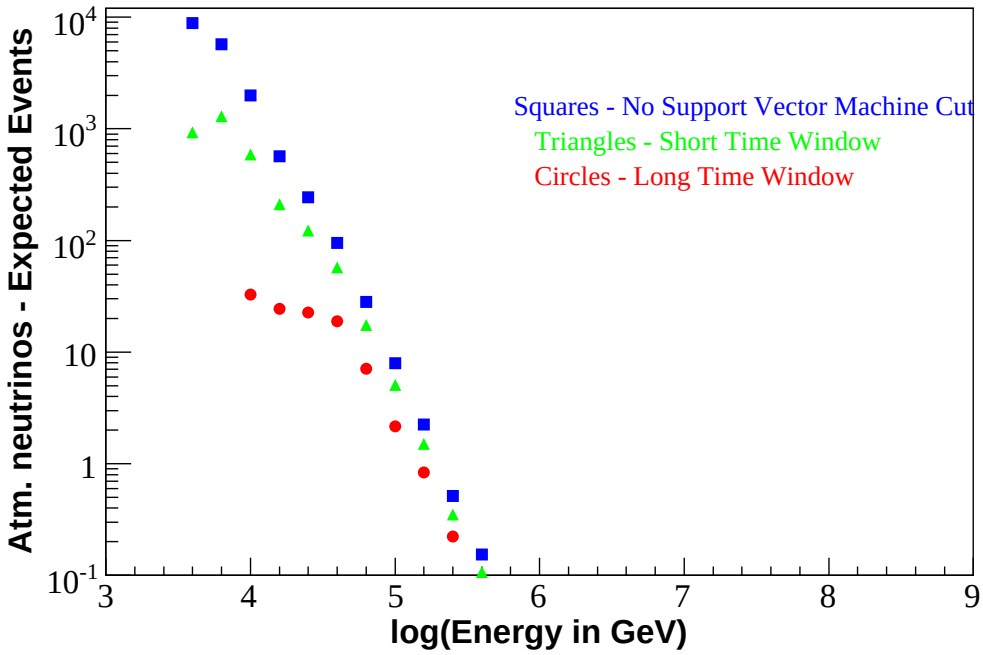

Figure 10.5: Expected relative number of muon atmospheric neutrino events (arbitrary normalization) surviving given particular cuts, plotted as a function of energy. The steep slope of the spectrum results in very few remaining events in this analysis.

$$V_{\text{cascade}}^{\text{eff}}(E_{\text{lower}}, E_{\text{upper}}) = V_{\text{gen}} \frac{n_{\text{sig}}}{n_{\text{gen}}}. \tag{10.2}$$

For particles traveling in long, linear paths, it is most appropriate to speak of effective areas. For three-dimensional spherical cascades, effective area is not a well-defined quantity and effective volume must be used instead. When calculating effective volumes using simulation, it is important to use a generation volume considerably larger than the detector, since AMANDA can detect some energetic cascades originating well outside the detector itself. Cascade effective volume and muon effective area are generally much larger values than neutrino effective area since only neutrinos which have interacted and produced particles are counted towards the number generated.

10.6 Sphere of Sensitivity

It is worth asking how close a burst would have to be for the AMANDA detector to be sensitive to it. This "sphere of sensitivity", the maximum radial distance from Earth at which one would have a 90% probability of observing a neutrino signature from the burst, provides an intuitive way of viewing the sensitivity of the analysis on a per-burst basis, rather than the amalgamation presented in the flux limit. This distance depends, of course, on several properties of the individual GRB which impact the neutrino rate predictions. The overall photon flux (which scales directly with neutrino output) and the break energy both have significant impact on the predicted neutrino rate. Additionally, neutrino fluence at the detector is inversely proportional to the square of the distance between Earth and the source. This relationship between

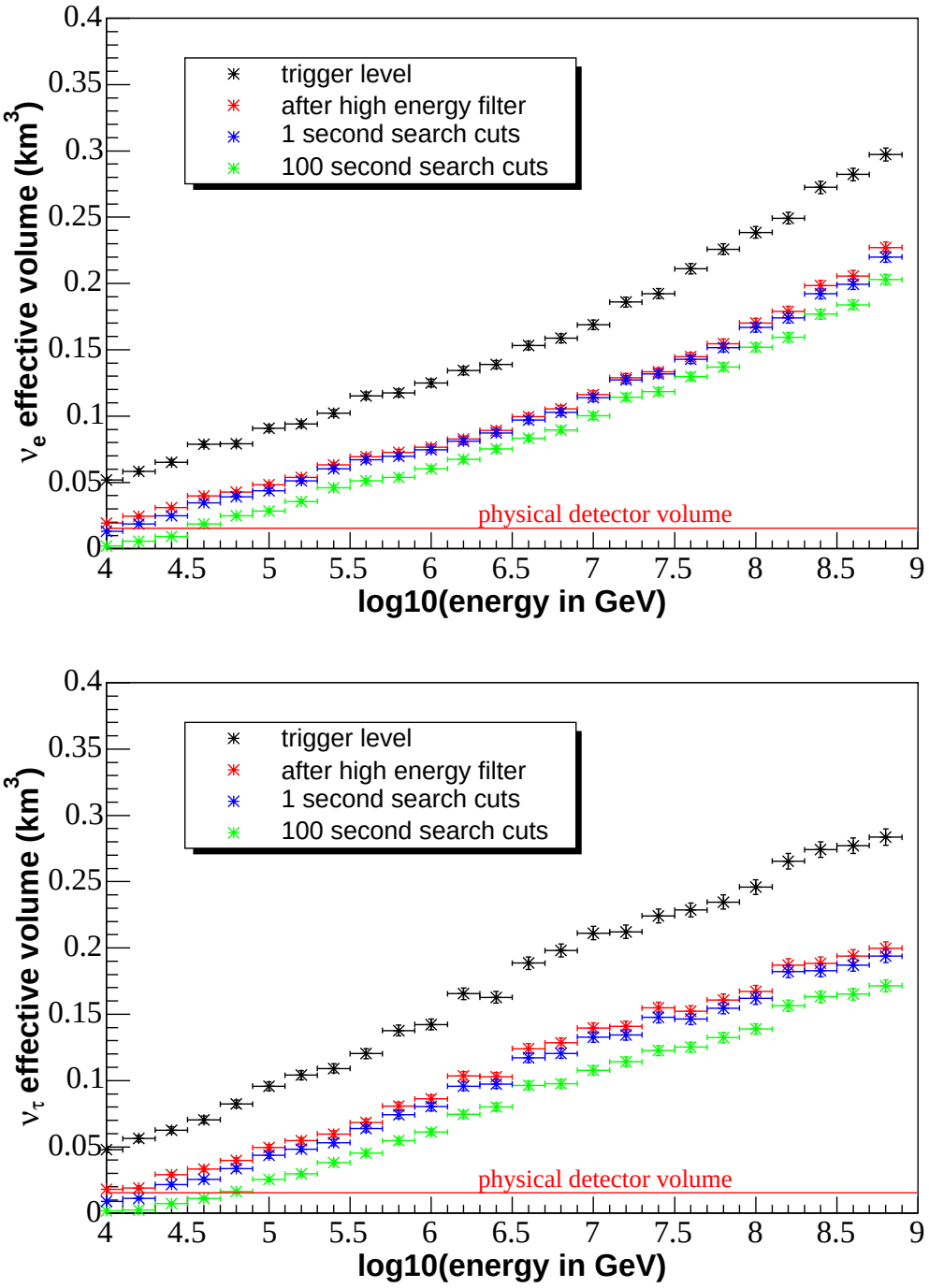

Figure 10.6: Effective volume for ν_e and ν_τ as a function of energy.

fluence and distance is intuitively obvious in the case of isotropic emission, but is valid for beamed jets such as GRB fireballs as well, since these are just conical sections and the same basic geometry applies to a part of a sphere as well as a whole one.

The distance between GRBs and Earth is usually discussed in terms of redshift z, the reddening of the wavelengths of light emitted by the GRB because of acceleration away from Earth. According to [55], the relationship between r and z can be calculated using the formula:

$$r = \frac{c}{H} \int_0^z \frac{dz'}{\sqrt{\Omega_{\rm vac} + \Omega_{\rm M}(1+z')^3}}. \tag{10.3}$$

The cosmological variables included in this equation are the Hubble constant H as well as $\Omega_{\rm M}$ and $\Omega_{\rm vac}$. These are the ratios of matter density and vacuum density to the critical density of the universe. As summarized in [100], the current best value for $\Omega_{\rm M}$ is around 0.3 and $\Omega_{\rm vac}$ is therefore about 0.7 assuming a flat ($\Omega_{\rm M} + \Omega_{\rm vac} = 1$) cosmology. The Hubble constant's current best value is around 71 km s^{-1}/Mpc. These values use the currently favored cold dark matter cosmology and are based on the results of the WMAP satellite as well as other experiments. The redshift z and (comoving radial) distance r have a roughly linear relationship at cosmologically small distances ($z \lesssim 0.04$).

Calculating how close a given burst would have to be for its neutrino spectrum to be visible is complicated by the fact that relativistic effects alter the predicted neutrino spectrum of a nearby burst relative to a distant one. Specifically, the first break energy in the Waxman-Bahcall spectrum is determined according to the formula:

$$\epsilon_\nu^b = 7 \times 10^5 \frac{1}{(1+z)^2} \frac{\Gamma_{2.5}^2}{\epsilon_{\gamma,\mathrm{MeV}}^b} \mathrm{GeV} \quad [55] \tag{10.4}$$

Given this relationship's dependence on z, a burst at a very close redshift ($z << 1$) will have a break energy almost 4 times higher than a burst at z=1. Depending on the specific slopes and break energies of that given burst, this can alter the predicted final neutrino rate by anywhere from 50% to 300% for the same flux normalization. Within the range z=0 to z=0.02, however, the change in the break energy is less than 4%, which leads to a negligible change in neutrino production and signal retention. Therefore, to good approximation at small z, the relationship between neutrino flux and redshift can be modeled as a simple inverse square relationship.

Factors other than observed fluence and overall spectral shape (such as baryon load and fraction of energy converted to $\pi^\pm$) are intrinsic properties of the burst themselves which are not redshift dependent. We can therefore predict the distance at which a given burst would have an observable neutrino spectrum simply by adjusting the spectral break energies appropriately and increasing the fluence at the detector as the burst is brought closer. (Our criterion for "sensitivity" in this context is a 90% probability of observing at least 5 neutrino events.) We have performed this calculation for 9 BATSE bursts with measured redshift using data compiled in [97]. Results for these bursts are summarized in the following table:

BATSE Trigger	fluence (erg/cm^2)	Actual Redshift	Observable Redshift
6225	3.96×10^{-6}	0.84	9.36×10^{-4}
6533	1.25×10^{-5}	3.42	1.70×10^{-3}
6891	6.22×10^{-5}	0.97	2.99×10^{-3}
7343	4.87×10^{-4}	1.6	3.89×10^{-3}
7549	2.11×10^{-4}	1.3	1.42×10^{-2}
7559	2.21×10^{-7}	1.62	3.12×10^{-4}
7560	2.06×10^{-5}	1.62	1.09×10^{-3}
7648	5.83×10^{-6}	0.43	7.99×10^{-4}
7906	2.51×10^{-4}	1.02	8.32×10^{-3}
8079	1.61×10^{-6}	1.12	1.87×10^{-4}

We have also performed a general calculation for "typical" bursts with $\Gamma \sim 300$, and a break energy of either 77 or 300 TeV as observed at a redshift of 1. Figure 10.7 shows the redshift at which this "typical" burst would be observable for a realistic range of fluences for both long and short bursts. The results confirm that at this stage an extremely unusual bright and/or close burst would be required for detection. However, future methods (and IceCube) will extend our range considerably. There are already many galaxies (including approximately 2000 galaxies in the Virgo cluster) which are within our sphere of sensitivity for bursts with fairly typical properties. One GRB, GRB980425, had a measured redshift of $\sim 9\times10^{-3}$, although this particular burst had an anomalously low electromagnetic fluence.

10.7 Conclusions and Future Directions

The rolling search method provides a useful complement to satellite-coincident analyses. The sensitivity on a per-burst basis is lower than for the satellite-triggered analyses, but the total sample of bursts is not limited to those which triggered satellites. Therefore, the overall sensitivity is competitive for periods in which there is

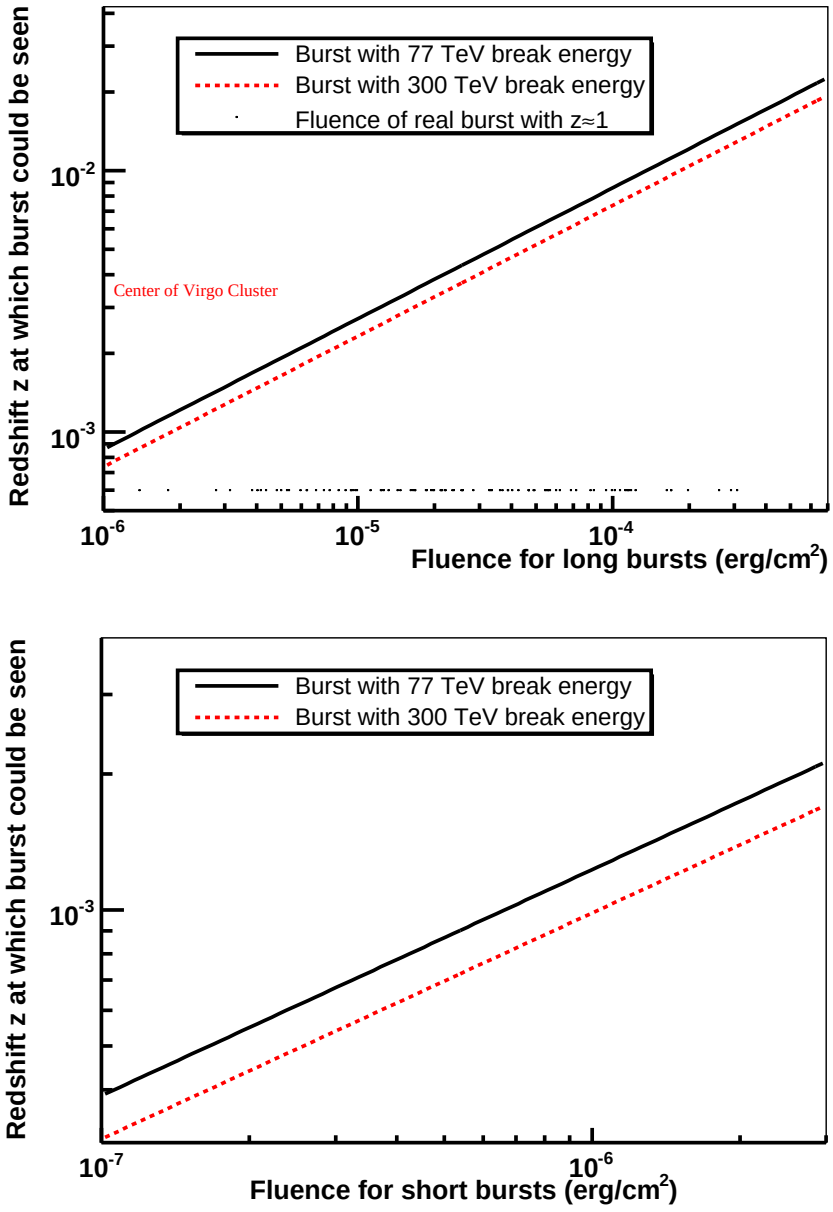

Figure 10.7: "Sphere of sensitivity" for bursts above the horizon assuming a bulk Lorentz factor of 300. The top and bottom lines are for 77 and 300 TeV break energies at z=1, respectively. The x-axis is the intensity of the burst, represented by the electromagnetic fluence normalized to a distance from Earth of z=1. The x-axes are plotted over realistic fluence ranges. Measured fluences of BATSE bursts in the range z=0.7 to 1.3 are plotted as black marks for comparison.

no dedicated GRB detector such as BATSE. Additionally, this method is capable of searching for photon-dark transients that other methods are not.

10.7.1 Muon Rolling Search

A future application of the rolling search method may be to apply a similar procedure to the muon channel. This has two primary advantages. The first is that spatial as well as temporal cuts can be applied, further reducing background. After obtaining multiple events in temporal coincidence, one can determine the angular difference in their reconstructed directions to see how many arrive within a pre-determined angular radius. Additionally, if one uses cuts similar to those used in the Zeuthen point source analysis, signal retention is far less dependent on energy than is the case for cascade cuts, meaning it is also far less model-dependent. This may therefore be the best means of obtaining a reasonable constraint on choked burst models. Preliminary estimates indicate that reasonable sensitivity to GRB spectra can be obtained using cuts from existing point source analyses, so it may be most practical to use pre-existing data selection from point source searches, thereby significantly reducing the overhead involved in performing such an analysis.

10.7.2 Rolling Searches Optimized for Non-GRB Transients

Although this analysis optimized on GRB prompt emission, there is no reason why future rolling analyses could not explicitly optimize for choked burst spectra, GRB-like supernova jets, or other non-GRB transient phenomena. AMANDA muon channel point source analyses have already used a technique somewhat similar to the rolling search method described in this thesis to search for neutrinos from flary periods

in specific blazars [101]. The analysis described in this thesis uses non-contained cascade events (originating outside the detector) because this dramatically increases the effective volume for higher energy events. For lower energy spectra, however, it may be beneficial to require contained cascades, such as was done in cascade analyses by Marek Kowalski [102] and Ignacio Taboada [22]. The reduction in effective volume will not be as severe for lower energy events and the better reconstructions would allow considerable improvements in background rejection.

10.7.3 Coincidence Studies

Looking for a simultaneous upward fluctuation in two or more experiments can be a means of improving sensitivity relative to a single experiment. In certain cases, such as gravitational wave detectors, where the experimental background is not well understood this is in fact one of the primary methods used in data reduction. Rolling searches are an obvious candidate for coincidence studies with other detectors. Since GRBs and other phenomena should emit multiple signals nearly simultaneously, other neutrino telescopes, gravitational wave detectors and large field-of-view γ-ray detectors such as Milagro are all obvious candidates for coincidence studies.

10.7.4 IceCube

The first 22 strings of IceCube have already been installed and rolling analyses stand to benefit as much as any other analysis from a large increase in effective area compared to AMANDA. The wider string spacing should not negatively effect searches for GRB neutrino emission too severely, since the predicted spectra peak in the energy range for which IceCube is optimized. An estimate of the improvement one

Figure 10.8: Successful neutrino capture by Bucky the Badger (artist's conception).

would expect when conducting an IceCube cascade rolling search analysis is provided in Appendix D. Since we are not in the regime of very small backgrounds, sensitivity does not improve linearly with effective area and one only gains an order of magnitude improvement in sensitivity by porting the current analysis more-or-less directly to IceCube. The future usefulness of cascade rolling search analyses in comparison with other techniques therefore hinges on improved background rejection. Fortunately, IceCube's superior data acquisition system should in principle make it possible to perform significantly better rejection techniques. As mentioned previously, muon rolling search techniques will have considerably lower background because of different cut selection techniques and the ability to take advantage of angular as well as temporal coincidence. A muon channel rolling search using IceCube is currently the most promising avenue to conduct future GRB rolling searches with improved sensitivity.

Bibliography

[1] F. Halzen, *Icefishing for Neutrinos* URL:http://www.phys.psu.edu/ cowen/popular-articles/index.html.

[2] D. Steele, *A Search for Extraterrestrial Point-Sources of Neutrinos with AMANDA-II*, PhD. thesis, University of Wisconsin - Madison.

[3] J. Cronin, T.K. Gaisser, and S.P. Swordy, Sci. Amer. **276** (1997) p44.

[4] E. Waxman, Ap. J. **606** (2004) 988-993.

[5] S. Wick, C.D. Dermer, A. Atoyan, Astropart. Phys. **21** (2004) 125-148.

[6] A. Achterberg, Y.A. Gallant, J.G. Kirk, and A.W. Guthmann, Mon. Not. RAS **328** (2001) 393.

[7] T. Piran, Rev. Mod. Phys. **76** (2004) 1143-1210.

[8] T.K. Gaisser and M. Honda, Annu. Rev. Nucl. Part. Sci. **52** (2002) 153-199.

[9] Y. Fukuda *et al.*, Phys. Rev. Lett. **81** (1998) 1158-1162.

[10] J.C. Van Der Velde *et al.*, Nucl. Instrum. Meth. A **264** (1988) 28-31.

[11] J. Ahrens *et al.*, Astropart. Phys. **16** (2002) 345-359.

[12] E. Waxman and J. Bahcall, Phys. Rev. Lett., **78** (1997) 12.

[13] H.J. Haubold, Nucl. Phys. A **621** (1997) 341c-344c.

[14] H. Athar, C.S. Kim, Jake Lee, Mod. Phys. Lett. A **21** (2006) 1049-1066 (hep-ph/0505017).

[15] T. Kashti, E. Waxman, Phys. Rev. Lett. **95** (2005) 181101.

[16] J. V. Jelley, *Cerenkov Radiation and Its Applications*. Pergamon: London, 1958.

[17] K. Young *et al.*, *Proc. 5th Conf. on Intersections of Particle and Nuclear Physics*, St. Petersburg FL, May 1994.

[18] L. Kuzmichev *et al.*, *Proc. 29th ICRC*, Pune India, August 2005.

[19] T. Pradier *et al.*, Frascati Phys. Ser. **555** (2004) 1-7.

[20] P. B. Price, Appl. Optics **36** (1997) 1965-1975.

[21] E. Andres *et al.*, Astropart. Phys. **13** (200) 1-20.

[22] I. Taboada, *Search for High Energy Neutrino Induced Cascades with the AMANDA-B10 Detector*, PhD. thesis, University of Pennsylvania.

[23] W.M. Yao *et al.*, J. Phys. G **33** (2006) 1.

[24] J. Learned and S. Pakvsa, Astropart. Phys. **3** (1995) 267.

[25] T. DeYoung, S. Razzaque, D. F. Cowen (astro-ph/0608486).

[26] R.W. Klebesadel, I.B. Strong, R.A. Olson, Ap. J. Lett. **182** (1973) L85.

[27] F. Halzen and D. Hooper, Rept. Prog. Phys. **65** (2002) 1025-1078.

[28] S. White, Astrophys. Space Sci., **208** (1993) 301.

[29] R. Hardtke, *The Search for High Energy Neutrinos from Gamma-Ray Bursts with the AMANDA Detector*, PhD thesis, University of Wisconsin - Madison.

[30] A.K. Harding, Phys. Reports, **206** (1991) 327.

[31] Z. Bagoly et al. accepted to A&A (astro-ph/0604326).

[32] G. Tagllaferri et al, Astron. Astrophys. **443** (2005) L1.

[33] B.E. Cobb *et al.*, Ap. J., **645** (2006) 113-116.

[34] P. Jakobsson *et al.*, *16th Annual October Astrophysics Conference in Maryland*, Washington D.C., November[2] 2005.

[35] W.S. Paciesas *et al.*, Ap. J. S. **122** (1999) 465.

[36] S. Ando, JCAP **0406** (2004) 007 (astro-ph/0405411).

[37] M.C. Miller, Ap. J. **626** (2005) L41-L44.

[2]This citation is not a typo. "The October Astrophysics Conference in Maryland" was apparently neither in October nor in Maryland.

[38] S.E. Woosley, A.I. MacFadyen and A. Heger, To be published in: *Supernovae and Gamma-Ray Bursts*, eds. M. Livio, K. Sahu, N. Panagia (Cambridge: Cambridge University Press) (astro-ph9909034).

[39] E. Liang, B. Zhang, F. Virgili, Z.G. Dai, Ap. J. in press (astro-ph/0605200).

[40] D. Guetta and J. Granot, Phys. Rev. Lett. **90** (2003) 201103.

[41] S. Campana *et al.* Nature, **442** (2006) 1008.

[42] J.P.U. Fynbo, J. Hjorth *et al.*, *Proc. 2003 Santa Fe Conference on GRBs.* Santa Fe NM, September 2003.

[43] S.R. Kulkarni, *et al.*, Nature **393** (1999) 35.

[44] F.A. Harrison, *et al.* (astro-ph/9905306).

[45] J.P. Halpern, *et al.*, Ap. J. Lett. **517** (1999) 105.

[46] P. Meszaros, *AIP Conf.Proc.* **526** (2000) 514-518.

[47] D. Band *et al.*, Ap. J. **413** (1993) 281.

[48] E. Waxman and J. Bahcall, Phys. Rev. D **59** (1998) 023002.

[49] L. Murase and S. Nagataki, Phys. Rev. D **73** (2006) 063002.

[50] L. Murase and S. Nagataki, Private communication.

[51] A. Atoyan and C.D. Dermer, *Proc. 2003 Santa Fe Conference on GRBs.* Santa Fe NM, September 2003.

[52] E. Waxman and J. Bahcall (astro-ph/9909286v2).

[53] S. Razzaque, P. Meszaros and E. Waxman. Phys. Rev. Lett. **90** (2003) 241103.

[54] S. Razzaque, P. Meszaros and E. Waxman, Phys. Rev. D **68** (2003) 083001.

[55] D. Guetta, M. Spada and E. Waxman, Ap. J. textbf559 (2001) 101-109.

[56] P. Meszaros and E Waxman. Phys. Rev. Lett. **87** (2001) 171102.

[57] S. Ando and J.F. Beacom, Phys. Rev. Lett. **95** (2005) 061103.

[58] F. Halzen, H. Landsman and T. Montaruli, *TeV photons and Neutrinos from giant soft-gamma repeaters flares.* (astro-ph/0503348).

[59] K. Ioka, S. Razzaque, S. Kobayashi and P. Meszaros, Ap. J. **633** (2005) 1013-1017.

[60] R. Bay, *Search for High Energy Emission from Gamma-Ray Bursts with the Antarctic Muon and Neutrino Detector Array (AMANDA)*, PhD thesis, University of Wisconsin - Madison.

[61] K. Kuehn, PhD thesis, University of California Irvine.

[62] M. Stamatikos for the IceCube Collaboration, J. Kurtzweil and M. Clarke. *Probing for Leptonic Signatures from GRB0303029* (astro-ph/0510336).

[63] B. Hughey and I. Taboada for the IceCube Collaboration, *Proc. 29^{th} ICRC*, Pune India, August 2005.

[64] J. Becker, M. Stamatikos, F. Halzen, W. Rhode, Astropart. Phys. **25** (2006) 118-128.

[65] The Tibet AS Collaboration: M. Amenomori *et al.*, Astron. Astrophys. **311** (1996) 919-926.

[66] G. Walker, R. Atkins and D. Kieda, Ap. J. **614** (2004) L93-L96.

[67] URL: http://www-zeuthen.desy.de/%7Ebernardi/point/filtering/badfiles/

[68] URL:http://www-zeuthen.desy.de/nuastro/software/siegmund/siegmund_old/pro/siegmund.html

[69] URL:http://icecube.wisc.edu/internal/amanda-archive/software/sieglinde/

[70] A. Pohl, *A Statistical Tool for Finding Non-Particle Events from AMANDA Neutrino Telescope*, PhD. thesis, Uppsala and Kalmar Universities.

[71] A. Pohl, URL: http://www5.hik.se/personal/tpoar/

[72] P. Steffen, *Direct-Walk: A Fast Track Search Algorithm Without Hit Cleaning*, AMANDA Int. Rep. 20010801.

[73] P. Steffen, *Direct-Walk II*, AMANDA Int. Rep. 20020201.

[74] D. Pandel, *Bestimmung von Waser- und Detektorparameteren und Rekonstrucion von Myonen bis 100 TeV mit dem Baikal-Neutrinoteleskip NT-72*, Diploma thesis, Humboldt University.

[75] J. Ahrens *et al.*, Nucl. Instr. Meth. **A524** (2004) 169-194.

[76] J. Ahrens *et al.*, Nucl. Instr. Meth. A **524** (2004), 169.

[77] A. Gazizov and M. Kowalski, *ANIS: High Energy Neutrino Generator for Neutrino Telescopes.* DESY report 04-101, June 2004 (astro-ph/04064390).

[78] K. Hanson, private communication.

[79] D. Heck *et al.*, Tech. Rep. FZKA report 6019 Forschungszantrum Karlsruhe (1998). http://iklau1.fzk.de/ heck/corsika

[80] D. Chirkin and W. Rhode, *Proc. 27^{th} ICRC*, Hamburg, Germany (2001) 1017-1020.

[81] S. Hundertmark, *Proc.1^{st} Workshop Methodical Aspects of Underwater/Ice Neutrino Telescopes*, Zeuthen, Germany 1998.

[82] C.J.C. Burges, *Data Mining and Knowledge Discovery* **2** (1998) 121-167.

[83] T. Joakims, *Making Large-Scale SVM Learning Practical. Advances in Kernel Methods - Support Vector Learning.* MIT Press, 1999, $1^{st}ed$.

[84] A. Roodman, *Proc.of PHYSTAT 2003*, Stanford CA, September 2003.

[85] G.C. Hill and K. Rawlins, Astropart. Phys. **19** (2003) 393-402.

[86] G.J. Feldman, R.D. Cousins, Phys. Rev. D **57** (1998) 3873.

[87] G.C. Hill, J. Hodges, B. Hughey, A. Karle and M. Stamatikos, *Proc. of PHYSTAT 2005*, Oxford, September 2005.

[88] J. Hodges for the IceCube Collaboration, *Proc. 29^{th} ICRC*, Pune India, August 2005.

[89] R.D. Cousins and V.L. Highland, Nucl. Instrum. Meth. A **320** (1992) 331-335.

[90] J. Conrad, O. Botner, A. Hallgren, and C. Pérez de los Heros, Phys. Rev. D **67** (2003) 012002.

[91] G.C. Hill, Phys. Rev. D **67** (2003) 118101.

[92] D. Reichart, D.Q. Lamb, E.E. Fenimore, E. Ramirez-Ruiz, T. Cline, K. Hurley, Ap. J. **552** (2001) 57-71.

[93] D. Guetta, T. Piran and E. Waxman Ap. J. **619** (2005) 412-419.

[94] E.W. Liang *et al.*, Ap. J. in press (astro-ph/0602142).

[95] P. Meszaros, Rept. Prog. Phys. **69** (2006) 2259-2322.

[96] URL: http://gcn.gsfc.nasa.gov/konus_grbs.html

[97] URL: http://www.arcetri.astro.it/∼dafne/grb/

[98] R. Plaga, Ap. J. Lett. **424** (1994) 9-12.

[99] U.F. Wichoski, J.H. MacGibbon and R.H. Brandenberger, Phys. Rev. **D65** (2002) 063005.

[100] J.R. Primack, *Proc. of 5th International UCLA Symposium on Sources and Detection of Dark Matter*, Marina del Rey CA, February 2002, ed. D. Cline (astro-ph/0205391).

[101] M. Ackermann, E. Bernardini, T. Hauschildt, E. Resconi *et al.*, *Proc. 29th ICRC*, Pune India, August 2005.

[102] M. Kowalski, *Search for Neutrino-induced Cascades With the AMANDA-II Detector*, PhD thesis. Humboldt University.

[103] M. Ackermann, E. Bernardini *et al.*, *Proc. 29th ICRC*, Pune India, August 2005.

[104] L. Anchordoqui and F. Halzen, Annals Phys. **321** (2006) 2660-2716.

[105] M. Stamatikos for the IceCube Collaboration and David L. Band, *Proc. 16th Annual Astrophysics Conference in Maryland.* Washington D.C., November 2005 (astro-ph/0602481).

[106] A.S. Friedman and J.S. Bloom, Ap. J. **627** (2005) 1-25.

Appendix A

Appendix A: Doublet and Triplet Times

The following is a listing of the event times for doublets in the 1 second search and triplets in the 100 second search.

2001 Short Window Search Doublets

Run	Day	Event Time 1	Event Time 2		Run	Day	Event Time 1	Event Time 2
3114	45	74929.308417	74929.441709		3263	174	71102.74321	71102.975873
3116	48	28983.473251	28984.305861		3263	174	84077.614042	84077.869319
3117	49	35048.498692	35048.576581		3266	177	39415.275696	39415.770327
3118	49	74360.135323	74360.982763		3267	178	43892.710933	43893.42136
3119	51	60745.524871	60746.159925		3271	182	15271.889019	15272.398
3121	53	52153.657608	52154.212144		3274	185	6886.060912	6886.86920902
3123	55	54558.366248	54558.375076		3277	188	11023.893724	11024.859486
3145	65	17517.00291	17517.446424		3278	189	29073.606747	29073.772381
3146	67	6162.19304899	6162.45024701		3284	195	4639.91779098	4640.91675302
3149	69	16765.872449	16766.013437		3287	197	80464.967816	80465.246399
3151	71	21859.744007	21860.681535		3291	200	11365.675871	11366.36875
3152	72	43963.672019	43964.335737		3293	202	58388.003082	58388.939941
3155	75	39284.505445	39284.695492		3299	205	11988.643878	11989.154179
3157	77	13888.483011	13889.202046		3305	210	46184.685461	46184.77029
3157	77	13980.054664	13980.528055		3306	211	60352.392627	60352.542645
3163	83	1631.83785402	1632.56043002		3306	211	60643.437404	60643.632832
3171	90	65760.943136	65761.255009		3309	214	60637.87154	60638.137231
3176	95	47507.227451	47508.029629		3310	215	42816.23796	42816.775779
3178	97	31834.661567	31835.255072		3312	218	7112.75187501	7113.18391299
3180	99	13684.999283	13685.95484		3313	218	47455.647183	47456.137478
3182	101	58149.650517	58149.785455		3313	219	3175.723032	3176.550408
3183	102	9927.42892998	9927.47331101		3320	225	79949.45741	79950.001766
3183	102	60796.347641	60797.172738		3323	228	69395.397676	69395.9818

2001 Short Window Search Doublets (continued)

Run	Day	Event Time 1	Event Time 2		Run	Day	Event Time 1	Event Time 2
3189	108	77911.433421	77911.552138		3325	230	47505.86204	47506.058511
3190	109	56835.228173	56835.689688		3329	234	26133.07737	26133.756555
3195	113	67761.117376	67761.504249		3332	237	72019.032652	72019.649899
3202	118	52867.608869	52867.617644		3339	239	30151.383177	30151.575429
3206	123	14251.885194	14252.512322		3340	240	51577.233567	51578.032823
3208	125	3824.108859	3824.65608499		3341	241	2019.68635002	2020.56338502
3208	125	29350.792479	29351.791203		3348	247	64614.931582	64615.480423
3209	125	64561.019441	64562.017088		3358	257	38709.370362	38709.5329
3210	126	84909.647737	84910.151586		3360	259	86242.026138	86242.131869
3216	129	26764.444702	26765.181438		3366	264	63432.725945	63433.518624
3216	130	8568.46132602	8569.46128198		3367	265	48247.161812	48247.204643
3219	132	30397.837817	30398.040503		3375	270	83610.4708	83610.772466
3223	136	47785.324109	47786.132097		3377	272	33172.356248	33173.309742
3224	137	63976.08805	63976.929545		3381	276	26843.657004	26844.487259
3225	139	18000.362496	18000.856888		3386	281	34362.175526	34363.027285
3226	140	13730.941989	13731.22832		3386	281	82337.362209	82337.82023
3228	141	51451.495873	51451.779037		3390	285	66945.091072	66945.405423
3229	142	55885.383477	55885.778257		3392	287	29382.386135	29382.55714
3233	146	81564.854076	81565.020623		3393	287	84574.093356	84574.356041
3235	149	27019.665375	27019.846504		3393	288	54822.443055	54822.693287
3239	153	6208.45110099	6209.18598701		3395	289	69184.727251	69185.630327
3240	153	83418.920439	83418.948591		3397	292	29238.948581	29239.412749
3249	163	50033.435974	50033.685203		3398	293	5335.629176	5335.835864
3252	165	78966.043162	78966.912613		3398	293	40883.852814	40884.587721
3261	172	54593.499841	54594.150597					

2002 Short Window Search Doublets

Run	Day	Event Time 1	Event Time 2		Run	Day	Event Time 1	Event Time 2
5469	45	26675.585005	26676.195977		5793	180	68930.774728	68931.28182
5469	45	58018.972839	58019.069989		5808	194	45231.872571	45232.820774
5470	46	68202.578345	68203.231202		5810	196	39135.534563	39136.187168
5470	46	69008.093614	69008.889095		5813	199	41259.74411	41260.140537
5523	56	8017.003293	8017.21065501		5817	203	86220.34776	86221.000415
5559	63	61886.827399	61887.672173		5820	206	28064.962055	28065.405112
5568	64	29457.440614	29457.561596		5821	206	71551.396187	71552.277469
5570	67	8618.55353997	8618.90547002		5821	207	57789.037252	57789.720965
5575	71	78423.501005	78423.526812		5823	208	78451.704508	78452.239762
5588	74	37392.681657	37392.87914		5824	210	4417.079469	4417.14650301
5588	74	70885.132567	70886.120474		5832	218	13590.402481	13591.346544
5589	75	60580.251363	60580.581126		5834	220	35899.719792	35899.730026
5590	76	58844.55688	58845.195327		5836	222	1242.89071398	1243.22588899
5591	77	71818.902926	71819.448433		5837	223	67823.928947	67824.835026

2002 Short Window Search Doublets (continued)

Run	Day	Event Time 1	Event Time 2		Run	Day	Event Time 1	Event Time 2
5599	81	55699.074198	55699.802535		5837	223	78530.284994	78530.536426
5599	82	14819.781555	14819.991585		5847	232	1601.83753798	1602.41544301
5605	86	80071.265721	80071.311772		5847	232	35227.697383	35228.365467
5606	87	47273.186532	47273.368612		5849	234	33290.861952	33291.308306
5615	92	49058.773634	49059.693033		5860	243	56544.152032	56545.114633
5621	97	63874.119725	63875.012933		5863	245	23165.480439	23165.554796
5622	98	42709.305635	42709.652936		5866	248	54863.941495	54864.916974
5628	101	30737.176555	30737.241565		5868	250	69194.23513	69194.277551
5628	101	53800.480161	53800.732974		5870	253	17100.758684	17101.511195
5629	102	44265.622147	44266.41963		5872	254	47925.563087	47926.431988
5639	107	41580.300126	41580.578565		5873	255	38098.596136	38098.856692
5639	108	4912.063123	4913.005965		5873	255	77650.96956	77651.330082
5664	109	2309.21354301	2309.55080198		5874	256	58118.840766	58118.88591
5672	117	10024.251822	10024.524717		5875	257	45657.947433	45658.674784
5675	119	84438.963511	84439.037161		5882	265	22778.212763	22779.164655
5676	120	71972.174811	71972.241677		5883	266	10828.940837	10829.681733
5678	123	1835.79745498	1836.63480902		5884	266	30430.108951	30430.277443
5678	123	47945.494919	47946.137759		5884	266	76781.748021	76782.533776
5684	128	81971.92301	81972.625353		5885	267	48144.62109	48144.719571
5684	129	55655.038103	55655.095074		5887	270	10554.092862	10555.007331
5688	133	60390.055085	60390.167384		5890	273	1494.91016301	1495.083358
5693	137	21726.885647	21726.971492		5891	273	36150.288643	36151.008334
5693	137	76948.410592	76949.246723		5892	274	79993.719319	79994.396926
5704	141	55883.464744	55884.437714		5893	275	40598.93819	40599.331778
5704	141	67893.525764	67893.954274		5895	278	19395.777547	19396.726716
5704	142	18468.002655	18468.292885		5896	278	42612.687737	42613.008765
5727	151	4476.23319299	4477.1719		5900	282	40003.144895	40003.840505
5730	154	9150.464024	9150.99051398		5912	291	17554.123034	17554.602866
5731	154	27392.244846	27392.430265		5917	296	60042.442687	60042.917556
5733	155	72979.861246	72980.323057		5919	298	36207.558662	36207.944549
5746	164	52123.164135	52123.847512		5921	300	29186.558749	29186.840451
5748	167	8713.819136	8714.75246003		5925	303	82181.090199	82181.884623
5751	170	7010.46264099	7010.75380198		5925	304	21610.867864	21611.205284
5751	170	9608.89162298	9609.22541501		5925	304	48127.704106	48127.928784
5788	175	77706.904029	77707.527488		5926	305	28989.606901	28989.896579
5788	176	52667.975699	52668.60463		5927	306	69683.510364	69683.665375
5789	176	83275.7683	83275.854937		5928	307	34150.793056	34151.246295

2003 Short Window Search Doublets

Run	Day	Event Time 1	Event Time 2		Run	Day	Event Time 1	Event Time 2
6912	44	63883.069263	63883.394444		7105	147	53192.884966	53193.694089
6914	46	43428.333021	43429.309347		7107	148	46591.112982	46591.915537
6915	47	31546.00855	31546.882764		7108	149	44747.99637	44748.663594
6915	47	36522.737319	36522.919439		7111	151	5376.98927898	5377.81133402
6919	48	82726.71111	82727.007145		7114	154	21492.761767	21492.879826
6922	49	41251.626634	41252.250597		7117	155	5527.87439699	5528.28264701
6925	50	18396.423413	18396.902646		7120	157	35077.449134	35077.826254
6926	50	67091.812219	67092.350499		7121	157	75967.415556	75968.102507
6926	51	23155.433343	23155.707954		7124	159	81881.442915	81882.012328
6927	51	53285.665345	53286.444122		7126	161	78885.871703	78886.098254
6927	51	58278.103125	58278.63023		7132	164	9724.82830202	9725.760856
6940	55	74356.207179	74357.1474		7135	166	47608.374462	47609.113406
6942	57	13440.658991	13441.168014		7136	167	27256.748462	27257.039324
6943	58	29965.347485	29965.430319		7142	171	82081.317761	82081.635935
6945	59	21629.267995	21630.082293		7150	177	35957.243309	35957.920861
6946	59	28204.127781	28204.283394		7151	177	85862.956224	85863.751643
6949	59	84600.242092	84600.864886		7153	180	17.682758976	18.458849984
6952	61	28007.190364	28008.08294		7156	182	60090.372326	60091.151027
6954	62	65320.333011	65321.272477		7159	185	61239.636424	61240.219977
6960	64	75205.577618	75205.636572		7206	196	23128.670271	23129.297287
6962	66	18551.571162	18552.373604		7206	196	47809.853602	47810.456986
6967	67	17127.09372	17127.753787		7212	202	48277.609572	48277.94313
6974	69	76008.405108	76008.865981		7214	204	31664.241756	31664.461428
6974	70	5287.41792602	5287.68339597		7217	206	66335.482368	66335.629029
6976	71	16288.085391	16288.781563		7218	207	48757.602201	48757.899762
6976	71	41219.327216	41220.140848		7219	208	44714.799658	44715.409275
6976	71	74336.299267	74337.246618		7219	208	77816.222344	77816.473174
6978	73	73248.86724	73249.152307		7222	211	34247.346066	34248.021835
6979	74	21237.340262	21237.841158		7229	213	63850.259209	63850.500866
6981	75	75786.058853	75786.071461		7233	216	26416.812915	26417.672119
6981	76	39665.865241	39666.851514		7236	219	22064.363562	22064.93762
6983	78	59.660819008	60.590198976		7236	219	40733.033511	40733.564634
6985	79	65620.999953	65621.022521		7240	223	41363.346707	41364.026162
6986	80	5351.6876	5351.94717299		7248	230	80772.086698	80772.75944
6986	80	40287.875974	40288.500926		7250	232	27614.183059	27614.531574
6988	82	38119.74808	38120.115937		7250	232	27695.1397	27695.718293
6990	83	26841.346725	26842.123386		7250	232	49526.695605	49526.832796
6997	85	75779.677127	75779.938101		7251	233	29782.294993	29782.830502
6998	87	23357.997138	23358.472288		7261	236	84592.567088	84593.215661
7008	92	11195.720368	11196.506261		7261	237	28787.216564	28787.325199
7017	98	2410.359036	2410.41829299		7263	238	85633.775384	85633.953597
7020	99	34477.166244	34477.849579		7264	240	46332.776634	46333.399253
7020	100	13032.349421	13033.121235		7266	241	4242.95679302	4243.82831501
7021	100	18930.796184	18931.358313		7271	243	32874.705927	32875.253778

2003 Short Window Search Doublets (continued)

Run	Day	Event Time 1	Event Time 2		Run	Day	Event Time 1	Event Time 2
7021	100	27467.815694	27468.788256		7271	243	64072.068692	64073.038332
7034	108	78596.037234	78596.530405		7272	243	72496.110932	72496.7486
7053	117	11667.199297	11667.98796		7294	251	52875.410615	52876.1684
7061	122	57652.209935	57652.287364		7294	251	73254.284379	73255.075511
7061	123	28408.097629	28408.783091		7297	254	61967.448554	61968.357619
7068	127	67306.915676	67307.560123		7301	258	53008.170722	53008.256062
7072	129	76278.820103	76279.102026		7344	296	11087.585961	11088.484309
7077	133	73788.170243	73788.222884		7345	297	61764.123949	61765.109306
7077	133	75969.484304	75969.492579		7346	298	31063.100027	31063.105415
7077	134	46953.123383	46953.159879		7348	300	68776.529213	68777.387152
7084	139	32841.504099	32841.763908		7349	301	8036.83264198	8036.98155302
7084	139	56252.556101	56253.521022		7353	303	32097.846932	32098.069699
7084	139	56805.280341	56805.861108		7354	304	30990.419235	30991.401489
7084	139	56805.280341	56805.861108		7354	304	30990.419235	30991.401489

2001 Long Window Search Triplets

Run	Day	Event Time 1	Event Time 2	Event Time 3
3123	55	27621.144132	27686.363083	27713.167542
3131	61	70441.53301	70492.511013	70519.35468
3131	61	70492.511013	70519.35468	70563.819445
3224	137	63894.791963	63976.08805	63976.929545
3280	191	16738.28367	16822.991313	16834.191385
3332	237	70406.229089	70419.092321	70425.997163

2002 Long Window Search Triplets

Run	Day	Event Time 1	Event Time 2	Event Time 3
5519	51	69081.526824	69092.3918	69178.468493
5575	71	58305.911873	58399.77314	58402.923576
5623	99	38906.664227	38928.812774	38978.882105
5675	120	37356.84093	37400.451547	37411.173533
5789	176	66788.815604	66811.187748	66841.747277
5830	216	51753.801891	51771.97027	51774.645654
5854	237	45265.325714	45268.908979	45363.191478
5895	277	71857.547014	71889.589552	71933.9095

2003 Long Window Search Triplets

Run	Day	Event Time 1	Event Time 2	Event Time 3
6961	65	30828.014481	30847.429385	30870.816527
6985	79	65555.437881	65620.999953	65621.022521
7021	100	61852.447915	61853.539347	61912.30649
7171	189	51130.15578	51147.355379	51198.941017
7345	297	19170.514394	19180.009407	19239.27788
7348	300	51263.428526	51312.274063	51347.43506

Appendix B

Appendix B: Δt plots

It is of critical importance that the distribution of background data can adequately be modeled by the Poisson distribution. Our expected probabilities of background fluctuation are based on Poissonian statistics, so a considerable deviation from this distribution would render the significances calculated for a cluster with a certain number of events meaningless. Other than an astrophysical signal, non-physical events (flares) are an obvious potential source of non-stochastic background which could potentially cause significant deviation from a Poissonian distribution.

Figures B.1 and B.2 show Δt distributions for events surviving cuts in the long and short time window searches, respectively. The superimposed dashed line is the expected behavior based on a Poissonian distribution normalized to the number of observed events. Since the average expected rate has been demonstrated to vary non-negligibly over the course of the year, this function is in reality the summation of separate Poissonian predictions for each of five periods in each year. The theoretical function is therefore of the form:

$$\sum \lambda_i b n_i \exp(-t\lambda_i) \tag{B.1}$$

where λ_i is the expected event rate for each period, n_i is the total number of events within that time period and b is simply the bin size in seconds (in order to scale to the real data in the plot). As can be seen in the figures, the data is entirely consistent with the assumption of a stochastic background modeled by Poissonian statistics.

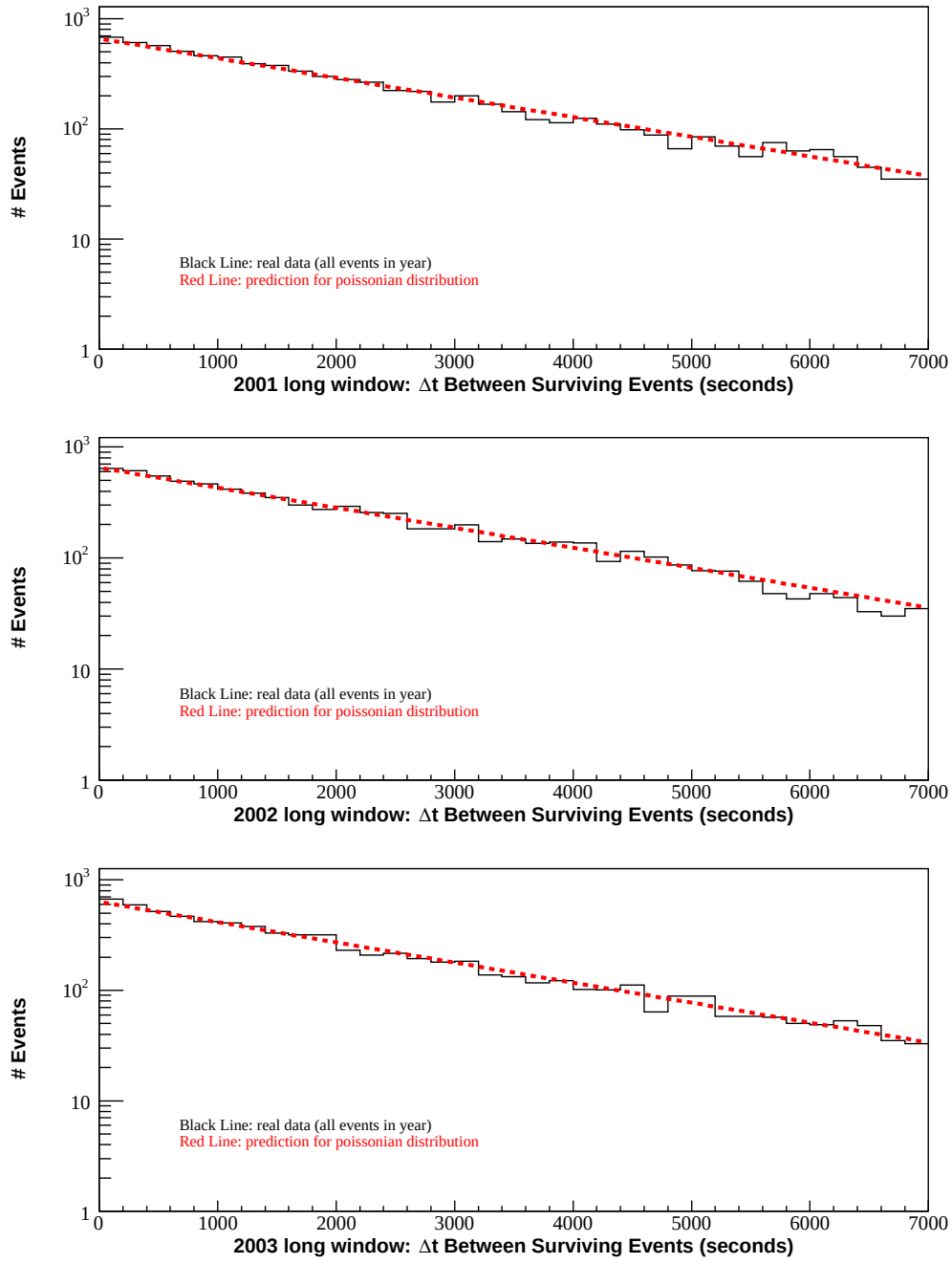

Figure B.1: Δt plots for events surviving cuts used in the long window search.

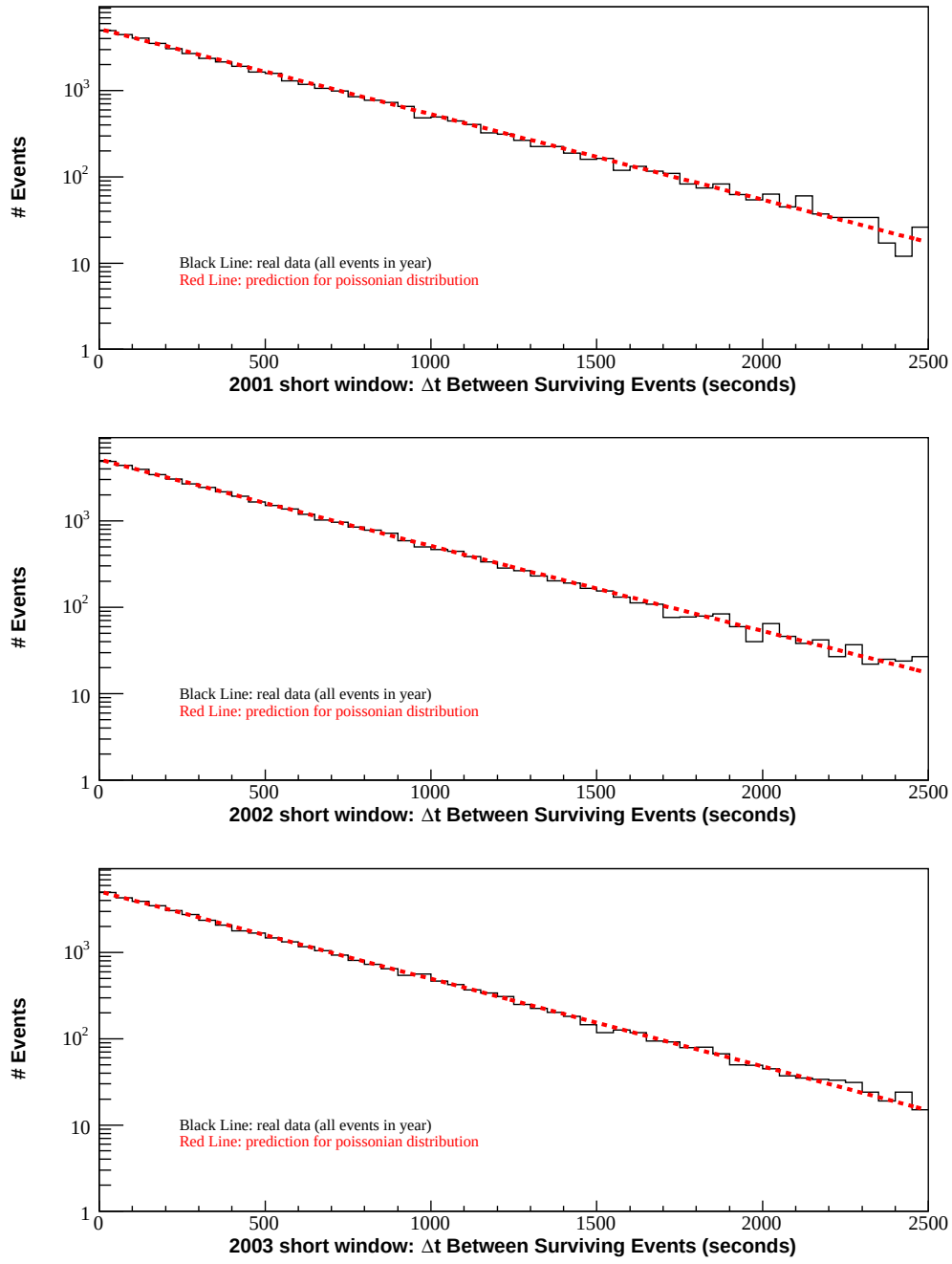

Figure B.2: Δt plots for events surviving cuts used in the short window search.

Appendix C

Appendix C: Background Rate Plots

In order to accurately model the expected number of events, it is also necessary that the data rates be consistent. Shown in figures C.1 and C.2 are the rate of surviving events per run for the long and short time window searches, respectively. The error bars show statistical uncertainty based on the total number of events in the run, so shorter runs (which are more common in 2002 and 2003) have larger error bars. These plots show relatively good consistency from run to run. In addition to random fluctuations, there are also seasonal variations visible in the short time window plots and even more obvious with looser cuts. These are due to the seasonal muon effect [103], in which pressure changes associated with varying temperature affect the rate of atmospheric muons in the detector. For this reason, each year was split into five sections to better characterize the background rate.

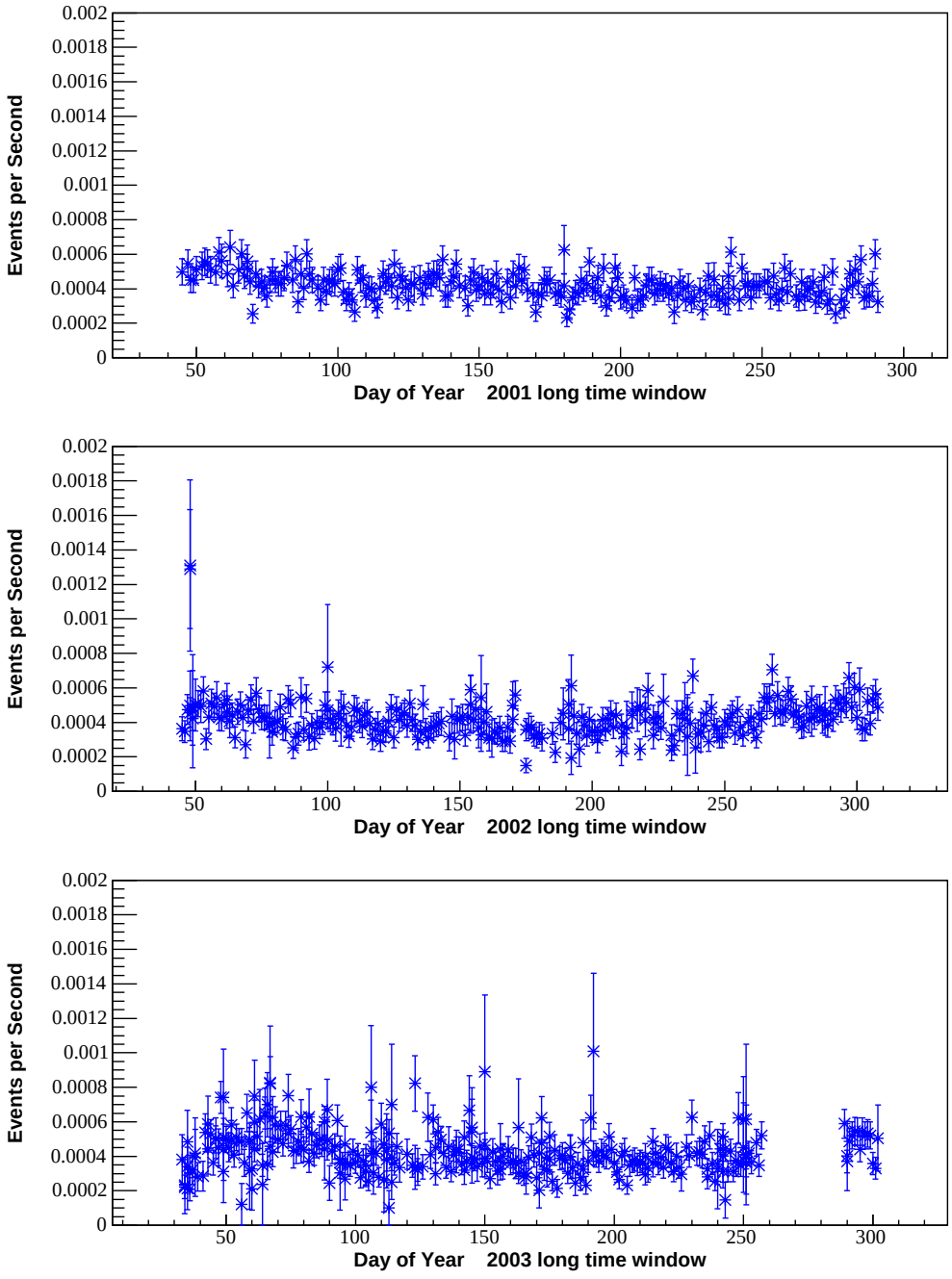

Figure C.1: Surviving event rate plots for the long window search.

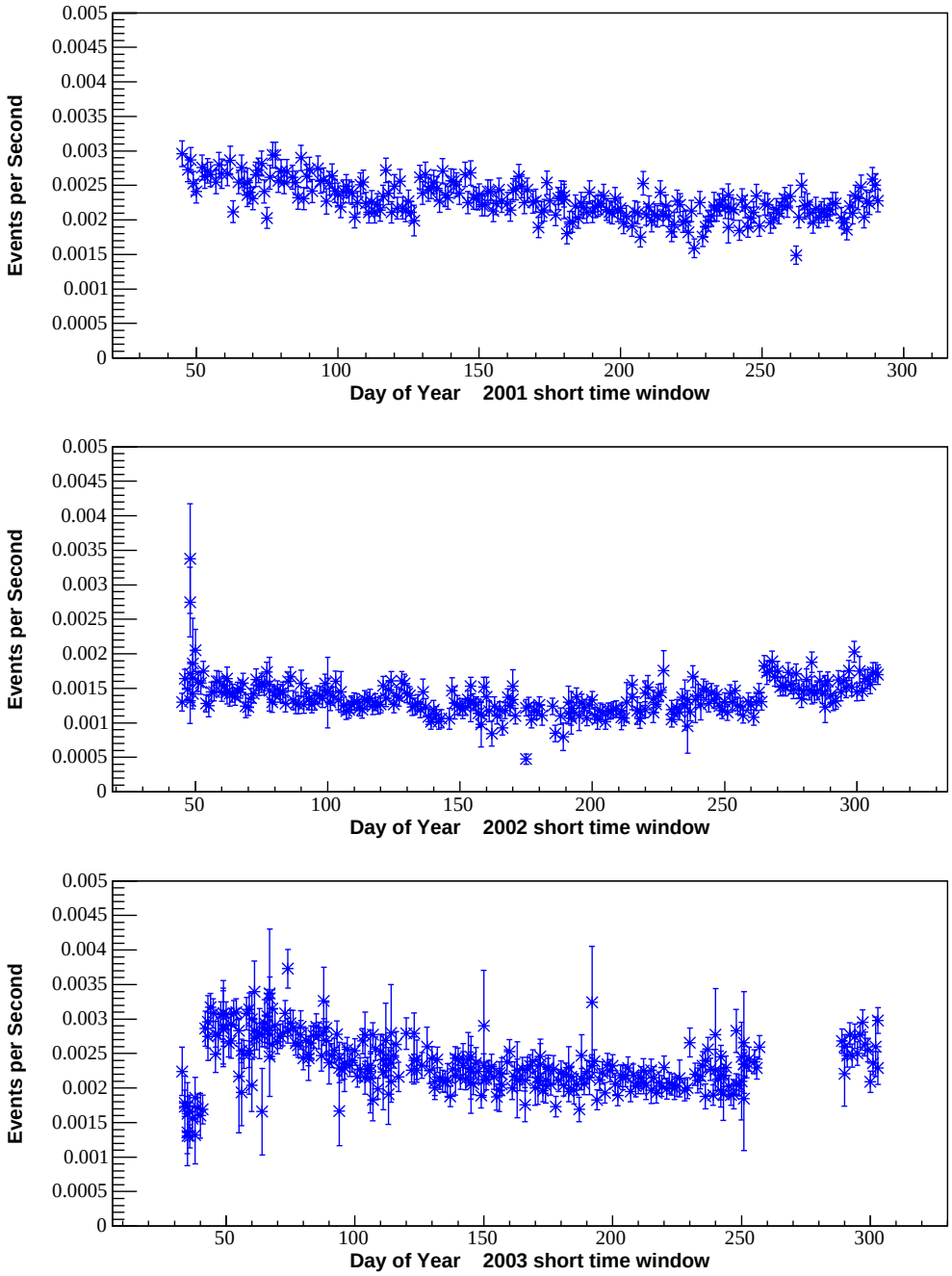

Figure C.2: Surviving event rate plots for the short window search.

Appendix D

Appendix D: IceCube Sensitivity

D.1 Rolling Search Sensitivity

In this section we present a back-of-the-envelope estimate of the improvement in the limit one should expect from an IceCube rolling search relative to the 3 year AMANDA rolling cascade search described in this thesis.

Comparing trigger level effective volumes from my cascade analysis to the predicted effective volume for IceCube [104], decade-by-decade improvements in effective volume are as follows:

Improvement in Effective Volume

Decade $\log_{10}$(E in GeV)	Factor Improvement
4 to 5	31.3
5 to 6	27.2
6 to 7	22.1
7 to 8	19.1
8 to 9	15.3

When this is weighted by the relative rates at various energies which one expects from a Waxman-Bahcall neutrino spectrum (figure 10.4) one obtains a factor of $\sim$26 improvement in effective volume. Assuming a comparable increase in the background

rate, the expected improvement in the limit would naively be a factor of $26/\sqrt{26} \approx 5.1$. However, the actual expected improvement is certainly better than this. The support vector machine cut retains ∼64% of the signal from a Waxman-Bahcall spectrum for the 100 second cut. By tightening the cuts, one can reduce the background to roughly 1/26th of its current rate and still retain ∼19% of the signal (roughly a factor of 3.4 reduction in signal retention rate). So, scaling up to IceCube's effective area, one can obtain the same background rates (hence the same requirements for signal detection) with a net improvement in the limit of a factor of 26/3.4=7.6. Of course, this is not re-optimized for the increased background and signal rates, and thus a factor of 7.6 improvement is a conservative minimum and the optimal sensitivity is likely to be somewhat better.

Perhaps more importantly, reconstruction methods will be improved for IceCube data relative to AMANDA. Rough estimates indicate that only a few surviving background events per year result from atmospheric neutrinos (which are an irreducible background because they are real neutrino events). Since our primary surviving background is the energetic tail of the downgoing atmospheric muon spectrum, we should in principle be able to distinguish real signal neutrino events from background given more information and better reconstruction techniques. The predicted signal flux is in principle sufficient to set limits well below the Waxman-Bahcall bound within a few years given enough improvement in background rejection.

D.2 Satellite Triggered analyses in IceCube

Since triggered analyses in IceCube are in the very low background regime, one expects sensitivity to improve roughly linearly with effective area. The analytical ma-

chinery developed for the rolling search can easily be adapted to look at the triggered analysis case, so in this section I present my own preliminary estimate concerning what can be expected from triggered GRB analyses in IceCube.

Excluding analyses which have focused on modeling only a single burst, triggered GRB analyses conducted up to this point have treated each burst as being essentially identical. They have simply divided the total neutrino flux in the year by the expected number of bursts above some threshold (usually the BATSE detection threshold) to obtain the expected rate per burst. Since these analyses are simply counting the total number of events observed, this is sufficient to get a reasonable expectation value for the average number of neutrino events. However, as discussed previously in this thesis, the rates of neutrino events expected from actual GRBs can vary from burst to burst by several orders of magnitude due to distance, luminosity and other factors, so the "average" value is not particularly meaningful when applied to an individual burst. The majority of bursts will have fluxes below the average, while a few nearby and energetic bursts will contain a much higher percentage of the neutrino flux. Of course, given a sufficiently large ensemble of bursts, the results from the realistic and flat distributions will converge as long as the expectation value is the same[1], but it is not *a priori* obvious what counts as a sufficiently large ensemble.

In this study we estimate the number of bursts required by IceCube to constrain the Waxman-Bahcall GRB neutrino emission model under several sets of assumptions. We compare results derived from Feldman-Cousins confidence intervals constructed with both the realistic "Guetta" distribution and the more simplistic "flat" distribu-

[1]Hooray for the Central Limit Theorem.

tion, as described in section 8.3 and demonstrated in Figure 8.5, to test what effect these assumptions have on the resulting limits. Since we are studying triggered analyses rather than the rolling search, we simply sum the signal over all examined bursts rather than look for event clusters. Additionally, rather than obtaining a limit by plotting the average expected event rate per burst on the y-axis of the confidence belt construction, we instead hold the average expected number of events per burst constant for each scenario and plot the total number of bursts examined on the y-axis. This allows us to easily examine how many bursts will need to be studied in order to rule out the assumed neutrino flux in that scenario.

We have conducted this simulation for 4 different assumed event rates. The first scenario examined was detection of the GRB flux at the Waxman-Bahcall limit using the cascade channel. Ignacio Taboada predicts 0.03 events in AMANDA-II after all selection effects for 73 bursts with neutrino emission at the Waxman-Bahcall bound. Taking the average flux per burst and doing an approximate re-scaling for IceCube effective volumes rather than AMANDA, we obtain an approximate rate of 0.01 cascade events per burst after cuts. Propagating this through toy Monte Carlo simulation and the Feldman Cousins sorting algorithm, IceCube is estimated to be sensitive to this flux level given a sample of 244 bursts under a "flat" distribution and 256 bursts under a realistic "Guetta" distribution of events per burst. In this context, sensitivity means that 0 events is excluded from the 90% confidence level belt for this number of bursts. 3 events (the standard for 5σ detection in the original AMANDA analysis) is the minimum value inside the confidence interval for 592 bursts for the flat distribution and 590 for the Guetta distribution.

The same process was repeated for the muon channel, assuming flux limit equivalent to Waxman-Bahcall. It was then done for both the muon and cascade channel, using more realistic estimate of the actual GRB event rates in a km^3 detector as calculated by Guetta et al. [97] for a large ensemble of BATSE bursts (using their Model 1). The following table summarizes the number of bursts required under these scenarios to be 90% confident of detecting either 1 or 3 events:

Scenario	events per burst	flat model 1 event	realistic model 1 event	flat model 3 events	realistic model 3 events
ν_μ predicted	0.006	407	419	984	983
ν_μ Waxman Bahcall	0.04	67	61	148	158
cascades predicted	0.002	1220	1231	2957	2945
cascade Waxman Bahcall	0.01	244	255	592	590

To make a fair comparison between the cascade and muon channels, it is necessary to keep in mind that the cascade channel has full sky coverage whereas the muon channel has only half sky coverage, resulting in a factor of two increase in the number of bursts which can be studied with the cascade channel.

Overall, the difference in sensitivity between assuming identical bursts and modeling a reasonably realistic distribution is small, but genuine and statistically significant[2]. Using the flat assumption is probably sufficient in most cases, especially scenarios which involve a large number of bursts. However, the difference can be on the order of 10% for smaller ensembles, so it is recommended that those applying limits should at least be cognizant of the assumptions that they are making.

[2]The number of bursts required for the realistic distribution in the Waxman-Bahcall flux/cascade channel scenario was determined several times using different random number seeds and the results never differed by more than one burst, so 244 bursts is significantly different than 255 bursts.

When interpreting the numbers obtained in this study there are a few caveats to bear in mind. The numbers provided here are done without regard to systematic uncertainties. By analogy with the current GRB analyses, one would anticipate approximately a factor of $\sim$1.5 increase in the required total signal for cascades and a factor of $\sim$1.2 for muons. However, the uncertainties should be somewhat smaller for IceCube analyses using photonics simulations than they were for AMANDA with PTD. The numbers stated here also assume thresholds for detection equivalent to those of BATSE. It is therefore more accurate to say that these are the required number of bursts which would have been above BATSE thresholds. Under current models of neutrino production, bursts below the threshold of BATSE detectability do not contribute significantly to the neutrino flux.

The true composite neutrino spectrum from real bursts will not in reality match the Waxman Bahcall spectrum shape, so this model will never be more than an approximation in the same way that the E^{-2} spectrum used for most high energy neutrino analyses is an approximation. Given sufficient information about each burst, a stacking analysis utilizing individual spectra could produce a more accurate composite "averaged" spectrum, although this is unlikely to significantly alter the predicted event numbers. One should also bear in mind that these numbers in this study should only be taken as rough estimates and that there is a substantial chance of an upward fluctuation rendering talk of flux limits unnecessary before these numbers are reached.

Appendix E

Modeling the Neutrino Flux From GRBs

In this appendix we discuss in some detail the process of modeling the prompt neutrino spectra of individual GRBs. We will take two examples of specific GRBs, GRB030328 and GRB020813. These two bursts were selected because they have the most complete measurements of the relevant variables of any bursts during the timeframe of the rolling search,with the exception of GRB030329, whose predicted neutrino spectrum has already been discussed in detail [62]. Both these bursts were identified by the HETE-II satellite. The procedure outlined in Guetta et al. [55] is used to derive the neutrino spectra. These spectra can vary quite widely from the Waxman-Bahcall spectrum. It should also be noted, however, that derived spectra for the same burst under different assumptions can vary significantly from each other as well, as this section will demonstrate.

The broken-power law spectrum for prompt GRB emission from the collapsar model is:

$$E^2\frac{\mathrm{d}\Phi}{\mathrm{d}E} = \frac{f_\pi}{8\epsilon_e}\frac{F_\gamma}{ln(10)}\begin{cases} (E/E_b)^{-\beta-1} & E < E_b \\ (E/E_b)^{-\alpha-1} & E_b < E < E_\pi \\ (E/E_b)^{-\alpha-1}(E/E_\pi)^{-2} & E > E_\pi \end{cases} \tag{E.1}$$

Note that the definitions for α and β used here are different by a sign and a factor of 1 from [55], but rather follow the definition used in the original power-law Band function fits of the GRB gamma-ray spectra [47] (see equation 4.1) as well as Mike Stamatikos's previous studies of the GRB030329 and GRB980703A neutrino spectra [105].

Prompt high energy neutrinos are produced by the same γ rays in the GRB jet which are observed as the prompt gamma-ray emission. Thus, after integrating over all interacting proton energies, the spectral slopes, α and β, and the overall fluence, F_γ, translate directly from the observed gamma-ray spectrum. The factor of 1/8 in equation E.1 arises because roughly 1/2 the pγ interactions result in the production of π^+ (the rest produce π^0) and each end product of the π^+ decay ($\nu_e \nu_\mu \bar{\nu}_\mu e$) is taken to receive roughly 1/4 of the total energy. The factor ϵ_e is the fraction of the internal energy converted to electrons, a factor which is not well-determined by current theoretical models. The fraction of the total energy converted to pions, f_π, is also not well constrained, but it can be estimated using other properties of the burst via the formula:

$$f_\pi = 0.2 \frac{L_{\gamma,52}}{\Gamma_{2.5}^4 t_{v,-2} E_{\gamma,MeV}^b} \tag{E.2}$$

where $L_{\gamma,52}$ is the burst luminosity, normalized to 10^{52} erg/s, $\Gamma_{2.5}$ is the bulk Lorentz factor normalized to $10^{2.5}$, $t_{v,-2}$ is the observed variability timescale normalized to 10^{-2} seconds and $E_{\gamma,MeV}^b$ is the break energy of the gamma-ray spectrum in MeV. There are several uncertainties in this calculation (in particular, the ability to correctly measure the variability timescale and luminosity has been called into question), and

an alternate formulation exists in which f_π is simply taken to be 0.2. This appears to yield results that are nearly as accurate on average. Following the example of Guetta et al., we will perform calculations with both constant and variable values of f_π.

Like the spectral slopes and overall fluence, the first break energy, E_b, in Equation E.1 can be derived directly from the γ-ray spectrum, although the relationship is a little more complicated:

$$E_b = 7 \times 10^5 \frac{1}{(1+z)^2} \frac{\Gamma_{2.5}^2}{E_{\gamma,MeV}^b} GeV \tag{E.3}$$

where z is the redshift of the burst. The most reliable method of determining redshift is through direct observations of the GRB afterglow, which fortunately were available for both of our sample bursts. In the absence of directly measured redshift values, it is possible to estimate the redshift using empirically observed relationships with values such as relative spectral lag and variability time [92], although this introduces additional uncertainties.

The second break (generally around 1 PeV) in the neutrino spectrum is not present in the gamma-ray spectrum at all but is rather caused by synchrotron energy losses in the parent π^+ (see equation 2.1) at high energies. The break can be estimated by the equation:

$$E_\pi = \frac{10^8}{1+z} \epsilon_e^{1/2} \epsilon_B^{-1/2} L_{\gamma,52}^{-1/2} \Gamma_{2.5}^4 t_{v,-2} GeV. \tag{E.4}$$

Here, ϵ_B is another equipartition fraction related to the magnetic field which causes the production of synchrotron photons.

The bulk Lorentz factor Γ, which appears in several of the above equations, is

itself not directly observable, but can be determined from observables. For bursts with low break energy (< 500 keV) we can estimate the bulk Lorentz factor by:

$$\Gamma \approx 10^{2.5} \sqrt{\epsilon_B^{1/2} \epsilon_e^{3/2} \frac{L_{\gamma,52}^{-1/2}}{E^b_{\gamma,MeV} t_{v,-2}}} \tag{E.5}$$

Likewise, the Luminosity, L, can be derived from the fluence at Earth, burst duration and distance between Earth and the burst through the elementary flux equation:

$$f_\gamma = F_\gamma / T_{90} = L/(4\pi D^2). \tag{E.6}$$

In the above equation, D is the comoving radial distance between Earth and the GRB. We derive this distance from the observed redshift, assuming (as in the Sphere of Sensitivity discussion in chapter 9) a flat universe ΛCDM cosmology, with Hubble constant $H_0 = 71$ km s^{-1}/Mpc and $\Omega_M = 0.3$.

The table below gives experimentally measured electromagnetic parameters for our sample bursts (as compiled in [106]), as well as the derived luminosity and bulk Lorentz factor. Approximate values associated with the Waxman-Bahcall spectrum are provided for comparison. Unfortunately, the equipartition parameters ϵ_e and ϵ_B are not known and estimates specific to these bursts could not be identified, so typical assumed values of 0.33 were used for each. Likewise, the variability timescales were assumed to be $\sim$10 ms, as is approximately true for the majority of GRBs.

Derived parameters

Burst identification	F_γ erg/cm^2	T_{90} s	z	α	β	E_γ MeV	L erg/s	Γ
GRB020813	9.79×10^{-5}	89.3	1.25	-0.94	-1.57	0.0895	1.94×10^{51}	525
GRB030328	3.0×10^{-5}	91.9	1.52	-1.14	-2.09	0.120	7.49×10^{50}	575
WB	6×10^{-6}	n/a	1	-1	-2	1	10^{52}	300

Under the assumption of isotropic emission and with f_π derived from Equation E.2, these electromagnetic parameters translate into the following values for the neutrino spectrum:

Burst parameters

Burst identification	E_b GeV	E_π GeV	f_π	A GeV/cm^2
GRB020813	4.3×10^6	7.7×10^8	0.057	5.7×10^{-4}
GRB030328	3.0×10^6	1.6×10^9	0.011	3.5×10^{-5}
WB	1×10^5	1×10^7	0.2	8.9×10^{-4}

However, if one assumes a beamed emission with opening half-angle $\theta_{\rm jet}$, the total luminosity changes by a factor of $1 - cos(\theta_{\rm jet})$, which alters the other properties accordingly.

Plots of the predicted spectra for these two bursts under various assumptions and in comparison to the Waxman-Bahcall spectrum are shown in Figure E.1. The fact that the first break occurs at higher energies relative to the Waxman-Bahcall spectrum for both selected bursts is a selection effect, since only bursts with relatively low breaks in the photon spectrum (hence higer breaks in the neutrino spectrum, see Equation E.3) have well-measured values for β due to the limited spectral range of HETE. Approximate numbers of cascade events (all flavors summed) expected in AMANDA-II and IceCube[1] for these spectra are given in the following table:

Expected Cascade Events

Burst/Model	AMANDA events	IceCube events
Waxman-Bahcall	9.7×10^{-5}	2.4×10^{-3}
GRB020813 Model 1	3.0×10^{-5}	7.0×10^{-4}
GRB020813 Model 2	1.1×10^{-4}	2.5×10^{-3}
GRB020813 Model 3	3.7×10^{-5}	7.6×10^{-4}
GRB030328 Model 1	2.6×10^{-6}	5.4×10^{-5}
GRB030328 Model 2	4.6×10^{-5}	9.6×10^{-4}
GRB030328 Model 3	4.3×10^{-6}	8.1×10^{-5}

[1] Or, to be semantically correct, the predicted number of cascade events in IceCube if the 80-string IceCube array existed at the time these bursts were detected.

Model 1 and 2 assume isotropic emission while Model 3 accounts for beaming. Model 1 uses equation E.2 to estimate f_π while Model 2 assumes f_π=0.2. The data selection criteria applied are the same as for the 100 second time window rolling search, meaning 43% of events retained relative to trigger level for the Waxman-Bahcall spectrum, with slightly better retention for bursts with higher break energies.

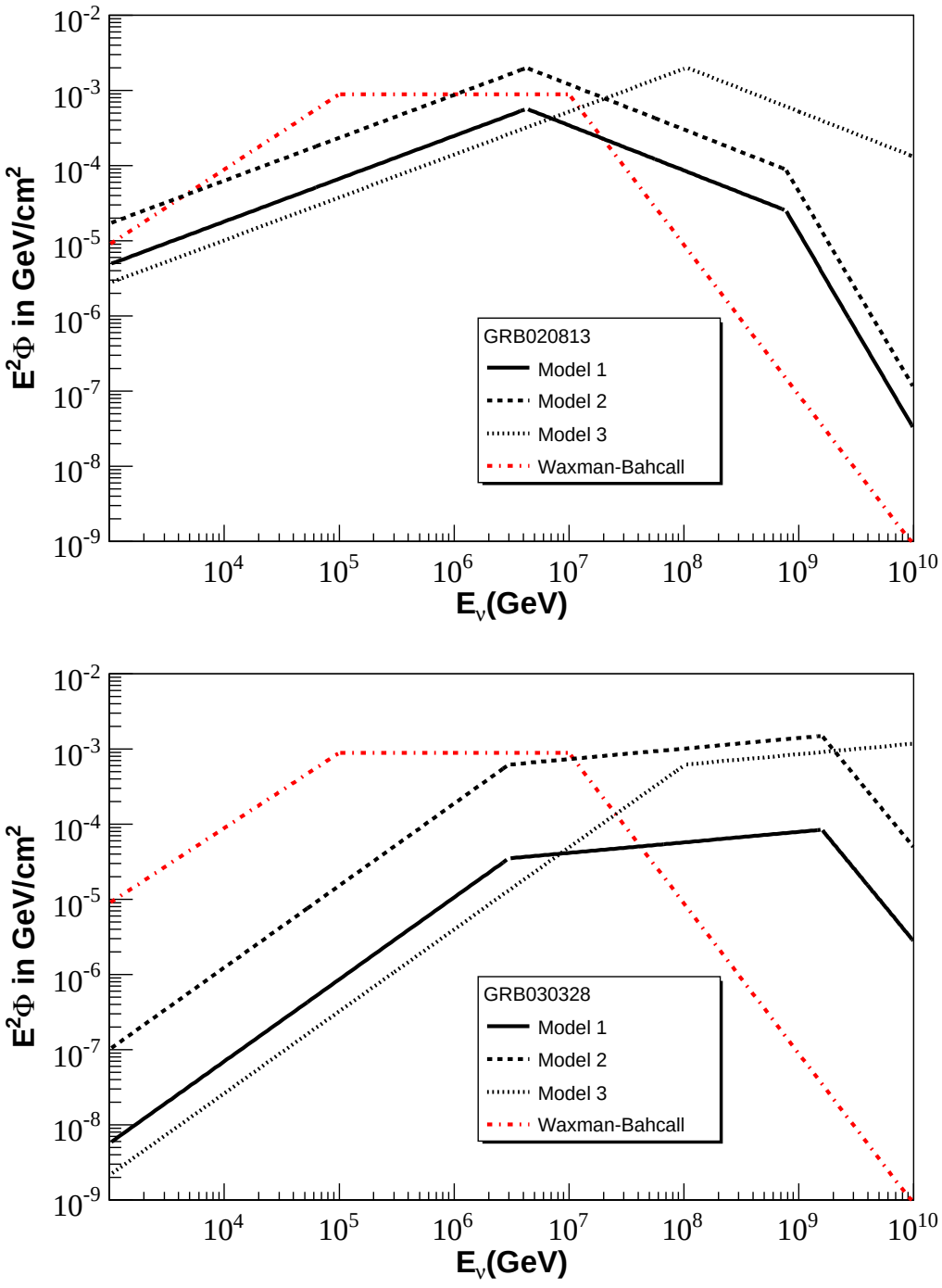

Figure E.1: Predicted neutrino spectra. Model 1 uses isotropic emission with variable f_π. Model 2 uses isotropic emission with fixed f_π. Model 3 assumes beamed jet emission.